UNIVERSITY OF CALIFORNIA, SAN DIEGO

Experimental Studies of Cross-Magnetic-Field Transport in Nonneutral Plasmas

A dissertation submitted in partial satisfaction of the

requirements for the degree Doctor of Philosophy

in Physics

by

Eric Matthias Hollmann

Committee in charge:

Professor C. Fred Driscoll, Chairman
Professor Robert E. Continetti
Professor Daniel H. E. Dubin
Professor Stan C. Luckhardt
Professor D. Asoka Mendis
Professor Thomas M. O'Neil

1999

The dissertation of Eric Matthias Hollmann is approved, and it is acceptable in quality and form for publication on microfilm:

Chairman

University of California, San Diego

1999

This dissertation is dedicated to my mother

in gratitude for many years of support.

There is a theory which states that if ever anybody discovers exactly what the Universe is for and why is is here, it will instantly disappear and be replaced by something even more bizarre and inexplicable. There is another theory which states that this has already happened.

- Douglas Adams

Contents

List of Figures

List of Tables

Acknowledgements

Foremost, I would like to acknowledge the help of Dr. Fred Driscoll and Dr. François Anderegg. Dr. Driscoll, my thesis advisor, has provided an abundance of useful advice and critical insight throughout my thesis work. It has also been a pleasure to work with Dr. Anderegg, who has taught me a tremendous amount about experimental physics and also designed and constructed the IV machine on which my thesis work was done. Both have provided me with an example of a very high standard of scientific research which I have tried hard to emulate.

I would also like to express my gratitude for the friendship and support of the other members of the UCSD nonneutral plasma group. Dr. Pei Huang was extremely helpful in getting me started on the IV machine. Dr. Tom O'Neil and Dr. Dan Dubin have been very helpful in explaining theory concepts to me. I owe a special debt of gratitude to the late Bob Bongard for many enjoyable discussions as well as for excellent electronics help. Jo Ann Christina provided unflagging secretarial support for the research group during my tenure as a graduate student. Thanks also go to Drs. Ann Cass, Brian Cluggish, Steve Crooks, Kevin Fine, Greg Flynn, Dirk Hartmann, Travis Mitchell, Eli Sarid, and Greg Severn, as well as my fellow graduate students James Danielson, Terry Hilsabeck, Dezhe Jin, Jason Kriesel, and David Schecter, with special thanks to James and Jason for careful proof-reading of this manuscript. Additional thanks also go to my outside thesis committee members, Drs. Robert Continetti, Stan Luckhardt, and Asoka Mendis.

I would also like to thank my friends and relatives for all the support during this thesis work.

This work was supported financially by the Department of Energy (FG03-85ER53199), Office of Naval Research (N00014-96-I-0239), and National Science Foundation (PHY94-21318).

Vita, Publications and Fields of Study

Vita

3 April 1970	Born, San Diego, California
1991	B.A., University of California, Berkeley
1993	M.S., University of Colorado, Boulder
1993-1999	Research Assistant, Department of Physics, University of California, San Diego
1999	Ph.D., University of California, San Diego

Publications

1. X.-P. Huang, F. Anderegg, T. M. O'Neil, C. F. Driscoll, and E. M. Hollmann, "Steady-State Pure Ion Plasmas Driven by a Rotating Field," *Bull. Am. Phys. Soc.* **40**, 1740, (1995).
2. E. M. Hollmann, F. Anderegg, D. Jin, D. H. E. Dubin, X.-P. Huang, and C. F. Driscoll, "Spin Depolarization of Magnesium Ions in a Penning-Malmberg Trap," *Bull. Am. Phys. Soc.* **40**, 1740, (1995).
3. E. M. Hollmann, X.-P. Huang, F. Anderegg, C. F. Driscoll, and T. M. O'Neil, "Measurement of Bounce-Resonant Particle Flux Driven by a 'Rotating Wall'," *Bull. Am. Phys. Soc.* **41**, 1955, (1996).
4. F. Anderegg, X.-P. Huang, E. M. Hollmann, C. F. Driscoll, T. M. O'Neil, and D. H. E. Dubin, "Test Particle Transport from Long-Range Collisions," *Phys. Plasmas* **4**, 1552, (1997).
5. X.-P. Huang, F. Anderegg, E. M. Hollmann, C. F. Driscoll, and T. M. O'Neil, "Steady-State Confinement of Nonneutral Plasmas by Rotating Electric Fields," *Phys. Rev. Lett.* **78**, 875, (1997).
6. F. Anderegg, X.-P. Huang, C. F. Driscoll, E. M. Hollmann, T. M. O'Neil, and D. H. E. Dubin, "Test Particle Transport due to Long-Range Interactions," *Phys. Rev. Lett.* **78**, 2128, (1997).
7. F. Anderegg, E. M. Hollmann, and C. F. Driscoll, "Transport in Nonneutral Plasmas due to Long-Range Collisions," *Bull. Am. Phys. Soc.* **42**, 1955, (1997).
8. E. M. Hollmann, F. Anderegg, and C. F. Driscoll, "Measurement of Cross-Magnetic-Field Heat Transport in a Nonneutral Plasma," *Bull. Am. Phys. Soc.* **42**, 1955, (1997).
9. F. Anderegg, E. M. Hollmann, and C. F. Driscoll, "Rotating Field Confinement of Pure Electron Plasmas Using Trivelpiece-Gould Modes," *Phys. Rev. Lett.* **81**, 4875, (1998).
10. F. Anderegg, E. M. Hollmann, and C. F. Driscoll, "Steady-State Confinement of Non-Neutral Plasmas Using Trivelpiece-Gould Modes Excited by 'Rotating Wall', " *Bull. Am. Phys. Soc.* **43**, 1806, (1998).
11. E. M. Hollmann, F. Anderegg, and C. F. Driscoll, "Measurement of Collisional Cross-Magnetic-Field Heat Transport in a Nonneutral Plasma," *Bull. Am. Phys. Soc.* **43**, 1806, (1998).

12. F. Anderegg, E. M. Hollmann, and C. F. Driscoll, " Steady-State Confinement of Electron Plasmas Using Trivelpiece-Gould Modes Excited by a 'Rotating Wall', " *Trapped Charged Particles and Fundamental Physics,* AIP Conference Proceedings **457**, New York: AIP (1999).

13. E. M. Hollmann, F. Anderegg, and C. F. Driscoll, "Measurement of Collisional Cross-Magnetic-Field Heat Transport in a Nonneutral Plasma," *Trapped Charged Particles and Fundamental Physics,* AIP Conference Proceedings **457**, New York: AIP (1999).

14. E. M. Hollmann, F. Anderegg, and C. F. Driscoll, "Measurement of Cross-Magnetic-Field Heat Transport in a Nonneutral Plasma," to be published in *Phys. Rev. Lett.*, 1999.

15. E. M. Hollmann, F. Anderegg, and C. F. Driscoll, "Confinement and Manipulation of Nonneutral Plasmas Using Trivelpiece-Gould Modes Driven by Rotating Electric Fields," to be submitted to *Phys. Plasmas*, 1999.

Fields of Study

Major Field: Physics

Studies in Plasma Physics
Professor Thomas M. O'Neil

Studies in Electromagnetism
Professor Thomas M. O'Neil

Studies in Classical Mechanics
Professor Herbert Levine

Studies in Quantum Mechanics
Professor George M. Fuller

Studies in Statistical Mechanics
Professor Daniel H. E. Dubin

Studies in General Relativity
Professor George M. Fuller

Studies in Quantum Field Theory
Professor Aneesh V. Manohar

Abstract of the Dissertation

Experimental Studies of Cross-Magnetic-Field Transport in Nonneutral Plasmas

by

Eric Matthias Hollmann
Doctor of Philosophy in Physics
University of California, San Diego, 1999
Dr. C. Fred Driscoll, Chairman

Cross-magnetic-field transport is studied in pure electron and pure magnesium ion plasma columns confined in a Penning-Malmberg trap. The transport in these systems can be classified as external transport or internal transport. External transport is a change in the plasma angular momentum or energy as a result of an externally applied perturbation, while internal transport refers to an internal rearrangement of particles and energy within the plasma. Internal transport tries to bring these plasmas into thermal equilibrium, but does not change the total plasma energy or angular momentum.

Measurements are presented of the external transport resulting from an applied rotating electric field, or "rotating wall" perturbation. The rotating wall is found to allow control of the plasma angular momentum, enabling density compression and long-term (week-long) steady-state plasma confinement. It is shown that the rotating wall couples to these plasmas through collective plasma modes.

The internal transport measurements presented are heat and test particle transport. Heat transport acts to smooth out temperature gradients in the plasma, while test particle transport acts to mix test particles with non-test particles. Both heat transport and test particle transport are found to be diffusive in nature and are found to be dominated by collisions acting on scale lengths up to the plasma shielding distance, or Debye length. These “long-range” collisions give a transport rate which can be greatly enhanced over that expected from classical “short-range” collisions acting on scale lengths up to the cyclotron radius. In the case of heat transport, for example, measured heat conduction rates can be more than two orders of magnitude larger than predictions due to classical short-range collisions. Measured test particle diffusion rates are found to be approximately ten times larger than classical. The scaling of measured test particle diffusion rates with density and magnetic field is the same as classical, while the measured thermal diffusion rates are found to be independent of density and magnetic field. These observations are in good agreement with theory predictions for long-range collisional transport. Independent measurements of the short-range collision rate are also found to be well-predicted by theory predictions.

Chapter 1

Introduction and Overview

1.1 Introduction

Research on nonneutral plasmas effectively began with mode experiments in electron beams in the 1960's [14]. Since then, both untrapped (beam) and trapped nonneutral plasmas have been studied, with motivation from basic plasma research, astrophysics, and atomic physics. One of the fundamental questions of plasma physics is how particles, energy, and angular momentum are transferred across magnetic field lines. Magnetic fusion and plasma processing, for example, depend crucially on an understanding of cross-magnetic-field transport.

Here, results are presented for cross-magnetic-field transport in nonneutral plasmas. The cylindrical column of charge is confined in the radial direction by a uniform magnetic field and confined in the axial direction by applied voltages. This confinement geometry is frequently referred to as a Penning-Malmberg trap, after Penning, who first used a similar geometry to make a pressure gauge [49], and Malmberg, who more recently pioneered the use of these traps for basic plasma physics experiments [40].

Cross-magnetic-field transport in nonneutral plasmas can be broadly categorized as external or internal transport. External transport arises from asymmetric or time-dependent external fields acting on the plasma. In general, the total plasma angular momentum can change as a result of an external field which has an angular dependence, while the total plasma energy can change as a result of an external field perturbation which has a time-dependence. This thesis presents the results of external asymmetry-induced transport of electron plasmas and ion plasmas; and on internal heat and test particle transport in ion plasmas.

The main external transport mechanism studied is the "rotating wall" perturbation, which is an azimuthally-rotating electric field that exerts a torque on the plasma column, thus allowing manipulation of the plasma angular momentum. The rotating wall technique enables arbitrary long-time confinement in these traps. Also, understanding the rotating wall transport mechanism could help in understanding the inherent asymmetry-induced transport which degrades confinement in these traps. Results are presented here for studies of rotating wall-induced transport on both pure electron and pure ion plasmas. It is found that the rotating wall perturbation produces a torque by driving azimuthally-dependent plasma modes.

Internal transport refers to transport due to the particles in the plasma interacting with each other. In general, internal transport drives the plasma toward a state of global thermal equilibrium, but cannot change the total plasma angular momentum or total plasma energy. Internal transport can result from binary ion-ion (or electron-electron) collisions, or from collective effects; in the work presented here, only binary ion-ion collisions are important. In nonneutral plasmas, global thermal equilibrium is characterized by radially uniform temperature and rotation frequency. Internal heat transport will thus tend to smooth out temperature gradients and internal viscous particle transport will tend to smooth out rotation frequency gradients. Additionally, if some ions are "tagged", then these particles diffuse radially as a result of "test particle transport".

Results on internal heat and test particle transport are presented. The heat transport in these plasmas is found to be diffusive in nature, and to be dominated by long-range collisions with impact parameter up to a Debye length. Classical heat transport theory considers only collisions with impact parameters up to the ion cyclotron radius (gyroradius); however, these collisions give much smaller cross-field heat transport. The test particle transport results presented here confirm the existence of long-range collisions in these plasmas: this transport is also found to be diffusive in nature, and is also found to be greatly enhanced by the effect of collisions with impact parameter up to the Debye length.

The rate of short-range, velocity-scattering collisions was measured by observing the rate at which the temperature parallel to the magnetic field equilibrates with the temperature perpendicular to the magnetic field; long-range collisions do not contribute to this temperature relaxation rate. Measurements of this anisotropic temperature relaxation rate for ion plasmas agree well with the predictions of classical collisional theory.

1.2 Overview of Dissertation

In Chapter 2, the experimental device on which this research was performed is described. The basic confinement principles of Penning-Malmberg traps are reviewed and the main diagnostics used (laser-induced fluorescence, charge collection, and image charge measurement) are presented. Also, relevant plasma manipulation techniques (laser heating/cooling, spin-state tagging, and electrostatic perturbations) are outlined.

In Chapter 3, the manipulation technique of an applied rotating electric field, or “rotating wall” is described. In these traps, the unneutralized plasma space charge creates a radial electric field and corresponding plasma $\mathbf{E} \times \mathbf{B}$ rotation. Unavoidable trap construction asymmetries drag on the rotating plasma, causing plasma expansion and eventual loss of particles. The rotating wall is an intentionally applied trap asymmetry rotating faster than the plasma, causing radial compression of the plasma. Perturbations rotating faster than the plasma are found to give a positive torque, while perturbations rotating slower than the plasma are found to give a negative torque. The positive applied torque enables steady-state plasma confinement (where the rotating wall torque balances the background drag) or plasma compression (where the rotating wall torque overcomes the background drag).

It is found that the rotating wall provides the strongest torque on these plasmas when the applied frequency is chosen so that a plasma mode is excited. Experiments are presented which unambiguously identify these modes in both electron and ion plasmas. Modes without azimuthal dependence are found to cause plasma heating but no torque, while modes with azimuthal dependence are found to cause both plasma heating and torque. We find that the mode-plasma coupling becomes nonlinear at very small drive amplitudes, although the observed mode frequencies are well-predicted by linear theory.

In Chapter 4, measurements of collisional heat transport in ion plasmas are presented. The plasmas are initially heated or cooled at a particular radius using a manipulating laser, and the time evolution of the plasma temperature is then measured to obtain the heat flux. The measured heat flux is found to be diffusive in nature, and is accurately predicted by a new theory of transport due to long-range collisions. The measurements are complicated by the presence of local heat sinks resulting from collisions with neutral molecules, and heat sources due to interactions between the plasma and trap asymmetries. Measurements of these background heat sinks are presented; the measured values are found to agree reasonably well with the predictions of a simple model.

Additionally, measurements of the anisotropic temperature relaxation rate are presented. An initial condition is created where the temperature parallel to the magnetic field is greater than the temperature perpendicular to the magnetic field. The rate at which this temperature anisotropy relaxes due to short-range ion-ion velocity-scattering collisions is measured, and is found to agree well with the classical collision rate.

In Chapter 5, measurements of test-particle transport in ion plasmas are presented. By spin-state tagging a localized group of ions and observing the radial (cross-field) spreading of the tagged ions, the test-particle transport flux is obtained. The test-particle flux is found to be diffusive in nature, and is also well-predicted by a new theory of transport due to long-range collisions. As in the case of heat transport, this analysis is complicated by the presence of background terms: here the dominant background terms result from collisional depolarization of the ion spins. Measurements of these terms are also presented.

Chapter 2

Experimental Setup

2.1 Overview

This chapter begins with a quick review of the basic geometry and confinement principles of Penning-Malmberg traps. The "IV" apparatus used for the experiments discussed in this thesis is then described. The LIF (laser-induced fluorescence) diagnostic is discussed, as well as the charge collection (collimator plate/ Faraday cup) diagnostic and the image charge (sector probe signal) diagnostic. Relevant plasma manipulation techniques are then described. These are laser heating and spin-state tagging, which are used on the ion plasmas, and electrostatic manipulations (in particular the launching and detection of electrostatic waves using wall-sectors) which are used in both ion and electron plasmas.

2.2 Review of Penning-Malmberg Traps

Figure 2.1 shows a schematic of a Penning-Malmberg trap. The basic geometry is a series of electrically isolated conducting cylinders aligned with a uniform magnetic field $\mathbf{B} = B\hat{z}$. The conducting cylinders are either grounded or biased to a voltage V_c so that particles with a single sign of charge are confined axially (positive magnesium ions are shown here); particles with the opposite sign of charge are not confined and escape in the axial ($\hat{z}$) direction. The unneutralized charge of the

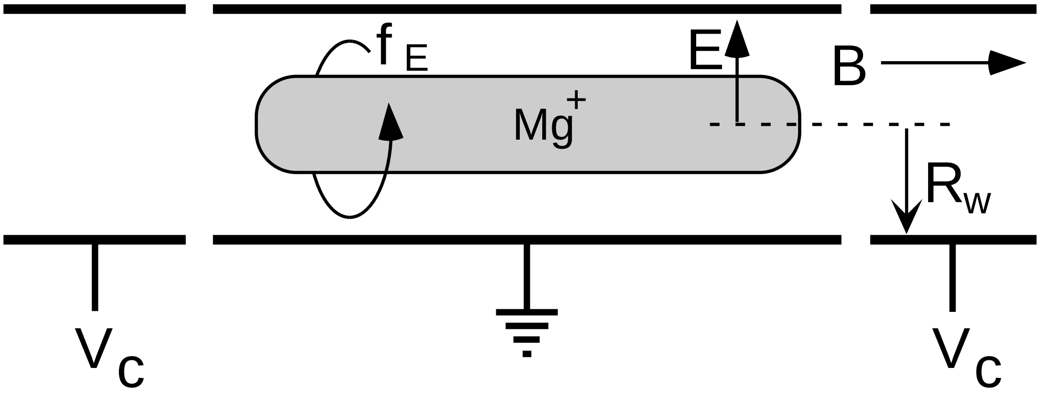

Figure 2.1: Basic geometry of Penning-Malmberg trap.

trapped particles creates a radial electric field **E** which results in an **E** × **B** rotation of the column at frequency f_E. This rotational motion of the charge column provides radial confinement against the radial electric field through the $\mathbf{v} \times \mathbf{B}$ term of the Lorentz force.

Normally, singly-ionized magnesium, Mg^+, is confined in the IV apparatus; however, for the rotating wall studies presented here (Chapter 3), we also perform experiments on electron plasmas.

The ion columns are typically confined at high enough densities n and low enough temperatures T that they can be considered plasmas: the columns are many Debye shielding lengths across, so collective interactions, rather than single particle effects, generally dominate the dynamics of the system [9].

Nonneutral plasmas in Penning-Malmberg traps have exceptional confinement properties. Axial confinement is assured energetically, presuming that the end-confinement voltages are large compared to the plasma space-charge potential plus the plasma temperature. For an ideal cylindrically symmetric trap, radial confinement is also guaranteed. This can be understood in terms of conservation of the total angular momentum of the plasma:

$$P_\theta = \sum_j [m v_{\theta,j} r_j + \frac{e}{c} A_\theta(r_j) r_j] \simeq (eB/2c) \sum_j r_j^2 \ , \tag{2.1}$$

where the sum is over the N_{tot} particles in the plasma, m is the particle mass, e is the charge (which can be positive or negative), $v_{\theta,j}$ is the θ component of the velocity of the jth particle, r_j is the radial position of the jth particle, and A_θ is the θ component of the vector potential. For a uniform magnetic field, this can be written: $A_\theta(r) = Br/2$ (we define B to be negative, i.e. $\mathbf{B} = -B\hat{z}$, for positive ions and B to be positive, i.e. $\mathbf{B} = +B\hat{z}$, for electrons).

For the low energy plasmas considered here, the kinetic component of the angular momentum, mv_θ, is negligible, so the plasma angular momentum is dominated by the angular momentum stored in the fields, i.e. $P_\theta \simeq (eB/2c)\sum_j r_j^2$. For the purposes of this work, the image charge contribution to P_θ can be ignored. In an ideal azimuthally symmetric trap, conservation of angular momentum thus implies conservation of the mean-square radius of the plasma, so the plasma is confined radially. In practice, collisions with neutral molecules and interactions with trap asymmetries decrease the angular momentum of the plasma; this causes an increase in the mean-square radius of the plasma and eventual particle loss to the trap walls at radius R_w.

The experiments discussed here operate in an ultra-high vacuum ($P_N \lesssim 4 \times 10^{-9}$ Torr), so inherent electric or magnetic field errors are believed to be the dominant source of drag on the plasmas. Measurements of inherent asymmetry-induced transport on electron columns show that the plasma expansion rate scales like $(L_p/B)^2$, where L_p is the length of the plasma [16]. Improved plasma confinement is therefore obtained for shorter plasmas and for higher magnetic fields. In the IV Penning-Malmberg trap, we routinely observe plasma lifetimes on time scales of thousands of seconds for short ($L_p \simeq 10$ cm) ion plasmas in a strong magnetic field

($B = 4$ T).

This exceptional confinement is related to the ability of nonneutral plasmas to be confined in a state of global thermal equilibrium; here, global thermal equilibrium is characterized by a uniform temperature and constant rotation frequency. This contrasts with neutral plasmas, which cannot be confined in a state of global thermal equilibrium by static electric and magnetic fields.

Nonneutral plasmas cannot be confined in thermal equilibrium at densities greater than the Brillouin limit, $n_B \equiv B^2/8\pi mc^2$ [8, 14]. The plasmas discussed here are at densities small compared to this limit, i.e. $n \ll n_B$. In this regime, the plasma angular rotation frequency ω_{tot} is small compared to the plasma frequency $\omega_p \equiv \sqrt{4\pi ne^2/m}$, which is small compared to the cyclotron frequency $\Omega_c \equiv eB/mc$; that is, we have the frequency ordering $\omega_{tot} \ll \omega_p \ll \Omega_c$.

2.3 Description of IV Apparatus

The basic schematic of the IV apparatus is shown in Figure 2.2. IV was designed and constructed by François Anderegg, who has written a more detailed description of the apparatus[4]. The electrodes fit inside of the bore of a superconducting magnet, which provides a constant magnetic field of up to $B = 4$ T inside the trap. The Mg^+ plasma is trapped near the axial center of the bore, where the field uniformity along the axis is better than 0.1% over a length of 30 cm (and better than 2% over a length of 60 cm). The magnetic field is carefully aligned with the axis of the electrode structure; this alignment is fine-tuned by using saddle-coil fields.

The electrode structure consists of isolated conducting cylinders with radius $R_w = 2.86$ cm and length $L_r = 5.84$ cm. These cylinders are biased or grounded to create an axial potential well for the plasma. In a typical ion experiment, for example, R4→R10 and R14 are biased to a confinement voltage $V_c = +200$ V, while

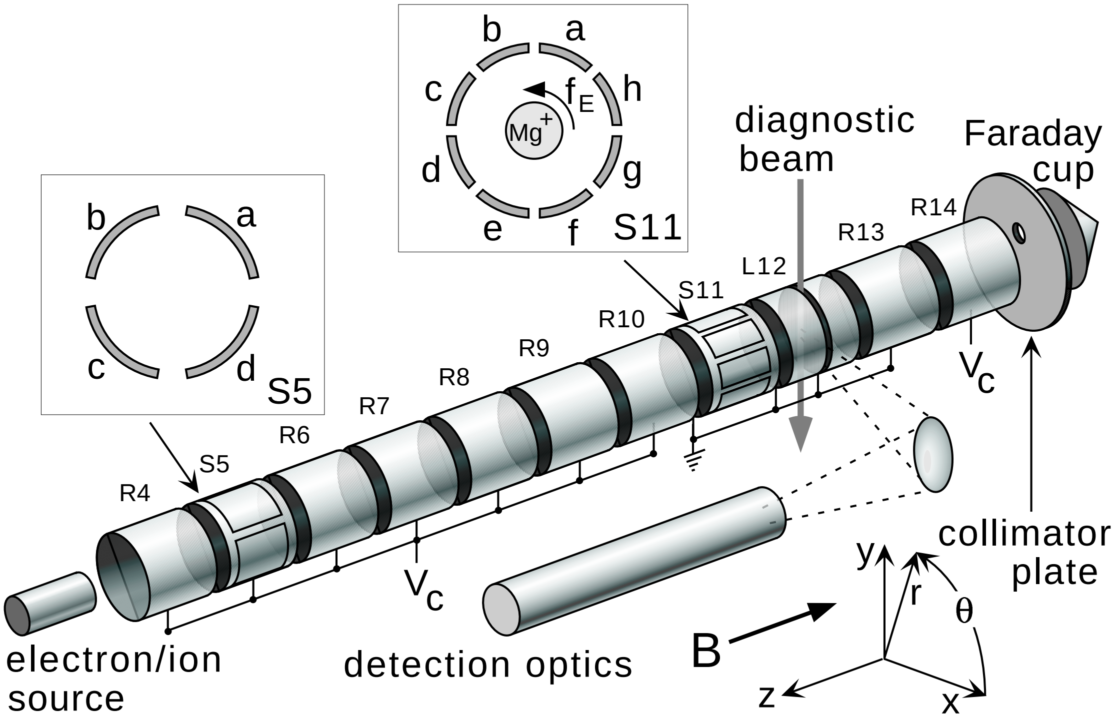

Figure 2.2: Schematic of the IV Penning-Malmberg trap. Source is actually located about 1 meter from R4.

S11→R13 are grounded, so that the (positive) ions are trapped by the potential well S11→R13. For these low-density plasmas, the plasma length is roughly the length of the confining region minus one ring, that is $L_p \simeq (N_r - 1) \times L_r$, so, for example, a plasma trapped in the region S11→R13 would be about $2 \times 5.84 \simeq 12$ cm long. Two of the rings, labeled S5 and S11, are sectored azimuthally; S5 is divided into 4 sectors, labeled S5a, S5b, S5c, and S5d, while S11 is divided into eight sectors. These sectors are isolated from each other by a conducting frame and can thus be used to drive and measure azimuthally-dependent perturbations in the plasma. The ring labeled L12 is perforated to allow the passage of UV light into and out of the trap for the laser diagnostic.

The electrode structure is enclosed by an ultra-high vacuum chamber. After a vacuum bake, the pressure is typically 7×10^{-11} Torr. For most of the data presented here, however, the apparatus was operated at a neutral pressure of 4×10^{-9} Torr. The neutral gas composition is mostly H_2 (97%) and CO (2.5%).

Referring to Figure 2.2, electrons or ions are created at the left (R4) end of the trap. To trap a plasma, the cylinders R4→R10 are grounded, ions or electrons which have been created to the left of R4 stream down the trap along the magnetic field, and then cylinders R4→R10 are biased to V_c to trap the particles. Typically, about $N_{tot} \simeq 10^9$ particles are trapped by this method. The ion and electron source position is not shown to scale in Figure 2.2; for both ions and electrons, the source is located about 1 meter to the left of R4, in the fringing field of the superconducting coil ($B_{source}/B \simeq 1/90$). A series of "inject electrodes" (not shown in Figure 2.2) are located between the source and the confinement electrodes; these inject electrodes are biased to form a potential well which draws the charges from the low-B region of the source into the high-B region of the confinement electrodes. For ion experiments, the source consists of a metal vacuum vapor arc (MEVVA), which can essentially be thought of as a spark-plug with a magnesium electrode. For electron experiments, the source consists of a hot tungsten filament, which creates electrons through thermionic emission.

The MEVVA initially creates an ion plasma consisting of both Mg^{+} and Mg^{++}. Within several minutes of injection, however, the doubly-ionized magnesium reacts with residual neutral gas in the trap to form impurity ions, such as magnesium hydrides, MgH_n^{+}. The ion experiments presented here are performed long after injection, at which point we find the plasmas to consist of about 70% Mg^{+} and 30% impurity ions.

2.4 Plasma Diagnostics

2.4.1 LIF Diagnostic

The principal diagnostic for this experiment is laser induced fluorescence (LIF) of singly-ionized magnesium ions, Mg^+. This provides an essentially non-perturbative measurement of the local ion velocity distribution, thus allowing *in situ* determination of ion density, temperature, and rotation velocity.

The basic idea of the LIF diagnostic is to use a laser to drive an atomic transition in the Mg^+ ions, and then detect the fluorescent photons. Magnesium ions were chosen for this diagnostic because of the experimentally desirable characteristics of the $3S \rightarrow 3P$ transition in Mg^+. This transition is excited out of the ground state, so LIF can be performed on cold ions. The transition occurs at an experimentally useable wavelength ($\lambda_0 \simeq 280$ nm) and is an electric dipole transition, which gives a large on-resonance scattering cross-section, small natural linewidth, and rapid spontaneous decay back to the ground state. Also, there are no branches to intermediary states to slow down the decay from the excited ($3P$) state to the ground state.

To obtain tuneable laser light at a wavelength $\lambda_0 \simeq 280$ nm, we use a frequency-doubled dye laser. A continuous beam (cw) dye laser is used; this allows for a narrow laser linewidth (about 0.5 MHz in the fundamental and about 1 MHz in the UV), giving good temperature resolution of the plasma. Typically, we use laser powers of less than 1 mW to diagnose the plasma.

Two types of transitions are used here: cyclic transitions and optical pumping transitions. The atomic level diagram for these transitions is shown in Figure 2.3. The Mg^+ ions in these plasmas are normally found in the $3S_{1/2}$ ground state with $m_j = +\frac{1}{2}$ or $m_j = -\frac{1}{2}$. The Zeeman splitting between the $3S_{1/2}, m_j = \pm\frac{1}{2}$ ground states is about $(1.2 \times 10^{-4}\,\text{eV})\ (B/1\,\text{T})$. Thus, for typical operating conditions ($B = 4\,\text{T},\ T \simeq .05\,\text{eV}$), the two ground states are equally populated. The energy difference

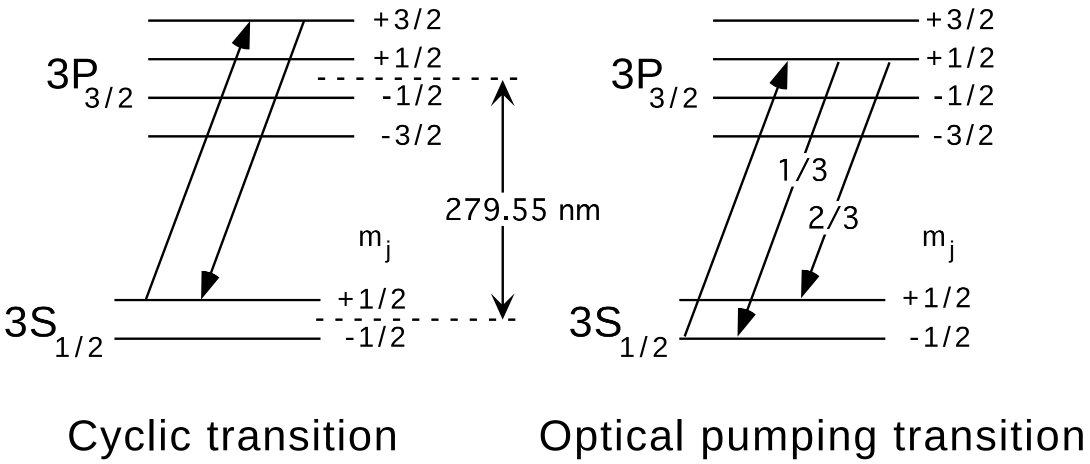

Figure 2.3: Level diagram of Mg^+ ion illustrating cyclic and optical pumping transitions.

between the ground ($3S$) and closest excited states ($3P$) is about 4.3 eV, so the excited states are unpopulated for typical plasma temperatures.

In a cyclic transition, an ion in the $(3S_{1/2}, m_j = +\frac{1}{2})$ ground state is excited to the $(3P_{3/2}, m_j = +\frac{3}{2})$ state after absorbing a 280 nm photon from the laser. The ion then spontaneously decays back to the $(3S_{1/2}, m_j = +\frac{1}{2})$ state; the $(3S_{1/2}, m_j = -\frac{1}{2})$ state is inaccessible because of angular momentum conservation. A second cyclic transition exists between the $(3S_{1/2}, m_j = -\frac{1}{2})$ and $(3P_{3/2}, m_j = -\frac{3}{2})$ states. Cyclic transitions are used to diagnose the plasma, since the ion is unperturbed after the absorption-emission process, aside from the small momentum kick received from the photon.

In an optical pumping transition, the ion is placed into an excited state which can decay to either ground state. In the transition shown in Figure 2.3, for example, an ion in the $(3S_{1/2}, m_j = -\frac{1}{2})$ ground state is excited to the $(3P_{3/2}, m_j = +\frac{1}{2})$ state. This state then decays to the $(3S_{1/2}, m_j = +\frac{1}{2})$ ground state (with a 2/3 probability), or the $(3S_{1/2}, m_j = -\frac{1}{2})$ ground state (with a 1/3 probability). Continued application of light at this frequency will therefore quickly drive any ions in the -1/2 ground state into the +1/2 ground state. Optical pumping transitions are used for test-particle transport, since the spin-alignment of the ion ground state can be used to spatially "tag" a small group of ions. Including $3S_{1/2} \rightarrow 3P_{1/2}$ transitions at $\lambda_0 \simeq 280.27$ nm (not shown in Figure 2.3), eight optical pumping $3S \rightarrow 3P$ transitions are available; here, we typically only use the $(3S_{1/2}, m_j = +\frac{1}{2}) \rightarrow (3P_{3/2}, m_j = -\frac{1}{2})$ transition (to pump ions into the -1/2 ground state) and the $(3S_{1/2}, m_j = -\frac{1}{2}) \rightarrow (3P_{3/2}, m_j = +\frac{1}{2})$ transition (to pump ions into the +1/2 ground state).

In the standard LIF diagnostic, the laser is scanned in frequency through the $(3S_{1/2}, m_j = +\frac{1}{2}) \rightarrow (3P_{3/2}, m_j = +\frac{3}{2})$ cyclic transition. The resulting scattered light is gathered and sent via an optical fiber to a photomultiplier tube/photon counter setup to be recorded as a function of time (and laser frequency). The frequency scan typically covers about 60 GHz and typically takes about 2 seconds to complete. The intensity of the detected fluorescence during the frequency scan is usually recorded in the photon counter in 10 ms bins with 2 ms dwell between each bin. Typically, these plasmas $\mathbf{E} \times \mathbf{B}$ rotate on a time scale of about 1 ms. Also, thermal particles typically bounce axially on a time scale of about 1 ms; thus the standard LIF measurement is averaged both azimuthally (over θ) and axially (over z).

The plasma temperature is obtained from the observed frequency-broadening of the transition. The plasmas studied here are generally in local thermal equilibrium, so the Doppler-broadened transition has the shape of a Maxwellian for each magnesium isotope (^{24}Mg$^+$, ^{25}Mg$^+$, and ^{26}Mg$^+$). The Doppler-broadening of the ^{24}Mg$^+$ peak is $\Delta\nu \equiv \sqrt{2}\nu_0(v_{24}/c) \approx (10.1\,\mathrm{GHz})\ (T/1\,\mathrm{eV})^{1/2}$, where $v_{24} \equiv \sqrt{T/m_{24}}$ is the velocity of a thermal ^{24}Mg$^+$ ion.

The laser beam can be shone through the plasma in the $-\hat{y}$-direction (shown in the Figure 2.2) or in the $-\hat{z}$-direction (with the source, collimator plate, and

Faraday cup removed). We designate the local plasma temperature parallel to the magnetic field as $T_{\|}$ and the temperature perpendicular to the magnetic field as $T_{\perp}$. If the beam is used in the perpendicular direction, there is a frequency shift ν_{rot} of the measured signal due to the total plasma rotation velocity v_{tot}: $\nu_{rot} = \nu_0(v_{tot}/c) \approx (0.2\,\mathrm{GHz})\,(r/1\,\mathrm{cm})\,(f_{tot}/1\,\mathrm{kHz})$, where ν_0 is the cyclic resonance frequency and $v_{tot} = 2\pi r f_{tot}$.

Fitting the scattered photon count rate ν_{photon} as a function of the laser detuning $\delta\nu \equiv \nu - \nu_0$ (for laser frequency ν) to three shifted Maxwellians (one for each isotope) gives the local magnesium density n_{Mg} as well as the local plasma temperature in the direction of beam propagation. For a perpendicular beam, the form of the fit used is:

$$\nu_{photon} \simeq A_1 \left\{ \exp\left[-\left(\frac{\delta\nu - \nu_{rot}}{\Delta\nu}\right)^2\right] + \alpha_{25}\exp\left[-\frac{25}{24}\left(\frac{\delta\nu - \nu_{rot} - \delta\nu_{25}}{\Delta\nu}\right)^2\right] \right.$$
$$\left. + \alpha_{26}\exp\left[-\frac{26}{24}\left(\frac{\delta\nu - \nu_{rot} - \delta\nu_{26}}{\Delta\nu}\right)^2\right] \right\} + A_0\,. \quad (2.2)$$

Here, $A_1 \equiv (2.1 \times 10^5\,\mathrm{photons/s})(n_{Mg}/10^7\,\mathrm{cm}^{-3})(I_0/1\,\mathrm{mW})(T_{\perp}/1\,\mathrm{eV})^{-1/2}$, where I_0 is the probe beam power. The coefficient A_1 depends primarily on the collection efficiency of LIF diagnostic (see Appendix A). A_0 is the measured background (off-resonance) count rate. We assume that there is no centrifugal mass separation in the plasma [45], so the magnesium isotopes are found in their natural abundance at each radius (79% ^{24}Mg, 10% ^{25}Mg, and 11% ^{26}Mg); these relative abundances give the constants $\alpha_{25} = 0.13$ and $\alpha_{26} = 0.14$. $\delta\nu_{25}$ and $\delta\nu_{26}$ are the isotope frequency shifts: $\delta\nu_{25} \simeq 2.28$ GHz and $\delta\nu_{26} \simeq 3.08$ GHz [17]. The same fit is used if the beam is applied in the parallel direction, but $v_{tot} = 0$ is used and $T_{\|}$ is obtained instead of $T_{\perp}$.

The LIF diagnostic initially diagnoses only half of the Mg$^+$ ions, that is, the ions in either the +1/2 or -1/2 ground state, depending on which cyclic transition is being used. During normal operation, however, the Lorentzian wings of the applied light will quickly (on the time scale of 1 second or so) optically pump the plasma into the state which is being sampled. If the $(3S_{1/2}, m_j = -\frac{1}{2}) \rightarrow (3P_{3/2}, m_j = -\frac{3}{2})$ cyclic transition is used, for example, the closest transition which can be driven is the $(3S_{1/2}, m_j = +\frac{1}{2}) \rightarrow (3P_{3/2}, m_j = -\frac{1}{2})$ optical pumping transition at $\delta\nu \simeq (9\,\mathrm{GHz})\,(B/1\,\mathrm{T})$; the opposing optical pumping transition, $(3S_{1/2}, m_j = -\frac{1}{2}) \rightarrow (3P_{3/2}, m_j = +\frac{1}{2})$, is at $\delta\nu \simeq (-32\,\mathrm{GHz})\,(B/1\ \mathrm{T})$ and is therefore not as strongly driven by the laser frequency sidebands. As a result, the plasma will quickly become spin-polarized into the state which is being probed (the -1/2 ground state) when driving this cyclic transition. The spin-polarization of the plasma is long-lived (spin polarization lifetimes are typically $>$ 100 seconds), and all of the Mg^+ ions are diagnosed during normal operation.

A typical LIF frequency scan is shown in Figure 2.4: here, the photon count rate ν_{photon} is plotted as a function of laser frequency detuning $\delta\nu$. The measured count rate is normalized by the instantaneous laser power $I_0 \simeq 0.5$ mW. The probe beam is shone perpendicularly across the plasma at radial position $r = -0.45$ cm. The beam is scanned through the cyclic transition frequency from offset $\delta\nu = -30$ GHz to $\delta\nu = +30$ GHz in about 2 seconds and the resulting scattered photon count rate ν_{photon} is recorded.

The solid line is a fit of Equation 2.2 to the data giving $\Delta\nu \simeq 3.32$ GHz (corresponding to perpendicular temperature $T_\perp \simeq 0.11$ eV), $\nu_{rot} \simeq 2.00$ GHz (corresponding to rotation velocity $v_{tot} \simeq 5.6 \times 10^4\,\mathrm{cm/s}$), magnesium density $n_{Mg} \simeq 3.3 \times 10^7\,\mathrm{cm}^{-3}$, and background count rate $A_0 \simeq 3.5 \times 10^3\,/\mathrm{s}$. It can be seen that the three-Maxwellian functional form of Equation 2.2 fits the data very well. In general, we find that the ion plasmas discussed here have measured velocity distributions which are well-described by Equation 2.2. The exception to this is very cold plasmas

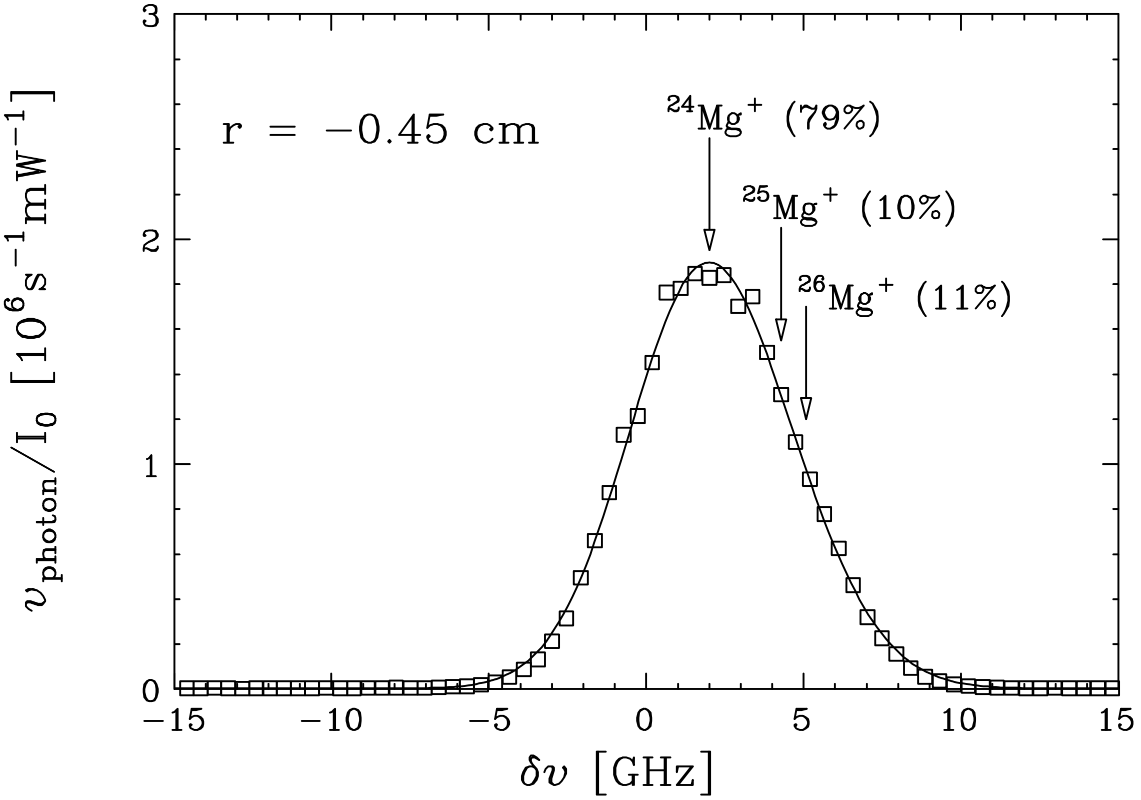

Figure 2.4: LIF frequency scan showing perpendicular velocity distribution and three-Maxwellian fit.

($T \lesssim 10^{-3}$ eV), where centrifugal separation of the isotopes can occur and the finite linewidth of the transition can become important; this is discussed in Appendix A.

In some experiments, such as some of the heat transport measurements of Chapter 4, the plasma temperature T evolves on a time scale which is fast compared with the 2 seconds required for a standard LIF frequency scan. On these time scales, the density can be regarded as constant, so the rapid temperature evolution at each radius $T(r,t)$ can be obtained from peak of the distribution function alone, i.e. we obtain $T_{||}(r,t)$ from $f_{||}(v_{||}=0,r,t)$ and we obtain $T_{\perp}(r,t)$ from $f_{\perp}(v_{\perp}=v_{tot},r,t)$.

By physically moving the probe beam and performing a LIF frequency scan at each radial position, the radial profiles of magnesium density, temperature, and rotation velocity can be obtained. Usually, ion plasmas are confined in rings S11→R13, so this gives a radial profile across the axial center ($z = L_p/2$) of the plasma. A

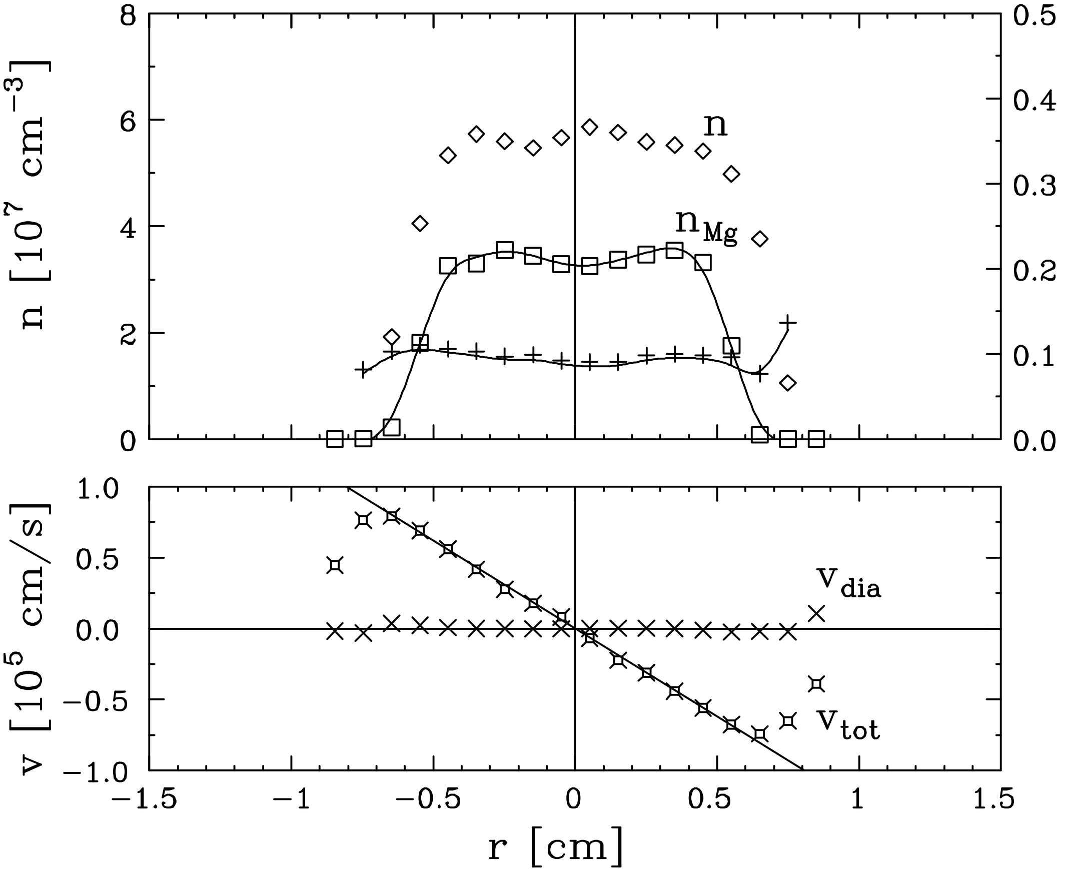

Figure 2.5: Radial profile of plasma showing density n, temperature T, and rotation velocity v.

typical radial profile of an ion plasma is shown in Figure 2.5. Here, each radial point represents a single perpendicular LIF frequency scan, such as Figure 2.4. The plasma was prevented from expanding during this measurement by using a rotating wall perturbation applied with the sectored ring S11.

Also plotted in Figure 2.5 is the total charge density $n(r)$ which is calculated from the measured quantities. The diamagnetic contribution to the total rotation frequency is calculated as:

$$v_{dia}(r) = -\frac{c}{eBn(r)}\frac{\partial}{\partial r}(nT_\perp)\,. \tag{2.3}$$

Since the laser measures v_{tot}, with $v_{tot} = v_E + v_{dia}$, we obtain the $\mathbf{E} \times \mathbf{B}$ rotation frequency $f_E = v_E/2\pi r$ from

$$v_E(r) = cE_r(r)/B = v_{tot}(r) - v_{dia}(r) \, . \tag{2.4}$$

For very cold plasmas, the diamagnetic term can be neglected. Otherwise, centrifugal separation can be neglected, so the diamagnetic term can be calculated by using $(1/n)\partial n/\partial r \simeq (1/n_{Mg})\partial n_{Mg}/\partial r$. The radial electric field E_r arises from the total charge density $n(r)$ through Poisson's equation,

$$(1/r)(\partial/\partial r)(rE_r) = -4\pi ne \, , \tag{2.5}$$

so the charge density is obtained by differentiating $f_E \equiv v_E/2\pi r$:

$$n(r) = -\frac{B}{2ecr}\frac{\partial}{\partial r}[r^2 f_E(r)] \, . \tag{2.6}$$

We typically find that about 70% of the ions in the trap are magnesium, i.e. $n_{Mg}/n \simeq 0.7$. The remainder of the ions, which we refer to as "dark matter" because they are invisible to the LIF diagnostic, are believed to be dominantly hydrides of magnesium, MgH_n^+. We believe these dark matter ions to be in thermal equilibrium with the magnesium ions, so the temperature and rotation velocity measured with the LIF diagnostic is a good measurement of the total plasma temperature and rotation.

In Figure 2.5, it appears that $n(r)/n_{Mg}(r) \neq const.$ This is a result of error introduced in the calculated $n(r)$ when taking the derivative of the (noisy) data at larger radii. Typically, we avoid this error with the approximation $n(r) \simeq C_n \, n_{Mg}(r)$, where C_n is a scale factor estimated from the rotation frequency near the center of the plasma, $C_n \equiv -\frac{f_E(r=0)B}{2\pi ecn_{Mg}(r=0)}$.

It can be seen that the plasma in Figure 2.5 is close to thermal equilibrium: the temperature $T_\perp$ is fairly constant as a function of radius, as is the rotation frequency $f_{tot} = v_{tot}/2\pi r$. The parallel temperature $T_{||}$ (not shown) is well-equilibrated with $T_\perp$, i.e. $T \simeq T_{||} \simeq T_\perp$, where $T \equiv \frac{1}{3}T_{||} + \frac{2}{3}T_\perp$ is the average temperature. The solid line through the f_{tot} data corresponds to $f_{tot} = 19.8$ kHz. The diamagnetic velocity v_{dia} is small here, so the total plasma rotation and $\mathbf{E} \times \mathbf{B}$ rotation are about the same: $f_E \simeq f_{tot}$. We find this to be true for most of the plasmas discussed here.

2.4.2 Charge Collection Diagnostic

The essential components of the charge collection diagnostic can be seen in Figure 2.2. Initially, the plasma is confined at both ends by voltages $V_c \simeq \pm 200\,V$ (+ for ions, - for electrons). When the voltage at the collection end of the machine is lowered ($V_c \rightarrow 0$), the charge is no longer confined in this direction and flows quickly along $\mathbf{B}$. Part of the charge, Q_c, is collected by the collimator plate; the remainder, Q_F, passes through a small circular hole with diameter $d_c = 1$ mm and is collected by the Faraday cup. The total number of ions confined is then $N_{tot} = (Q_c + Q_F)/e$. The density at the radius of the collimator plate hole can be found from:

$$n(r) = \frac{4Q_F(r)}{\pi e d_c^2 L_p}\,, \tag{2.7}$$

where the plasma length L_p is estimated from the confinement geometry.

For ion plasmas, this destructive diagnostic is less desirable than the non-destructive LIF diagnostic and is therefore primarily used to check the LIF calibration. For electron plasmas, however, the charge collection diagnostic is the principal method by which the plasma density profile is measured.

A typical electron plasma radial density profile taken with the charge collection diagnostic is shown in Figure 2.6. Here, an electron plasma is injected, held for 5 seconds, and then dumped onto the collimator plate and Faraday cup. The collimator plate hole is then translated slightly in radius and the measurement is repeated, until the entire radial profile has been reconstructed. This diagnostic requires good shot-to-shot repeatability of the initial conditions; we typically find good repeatability, with shot-to-shot density variations $\delta n/n < .01$ at $r = 0$.

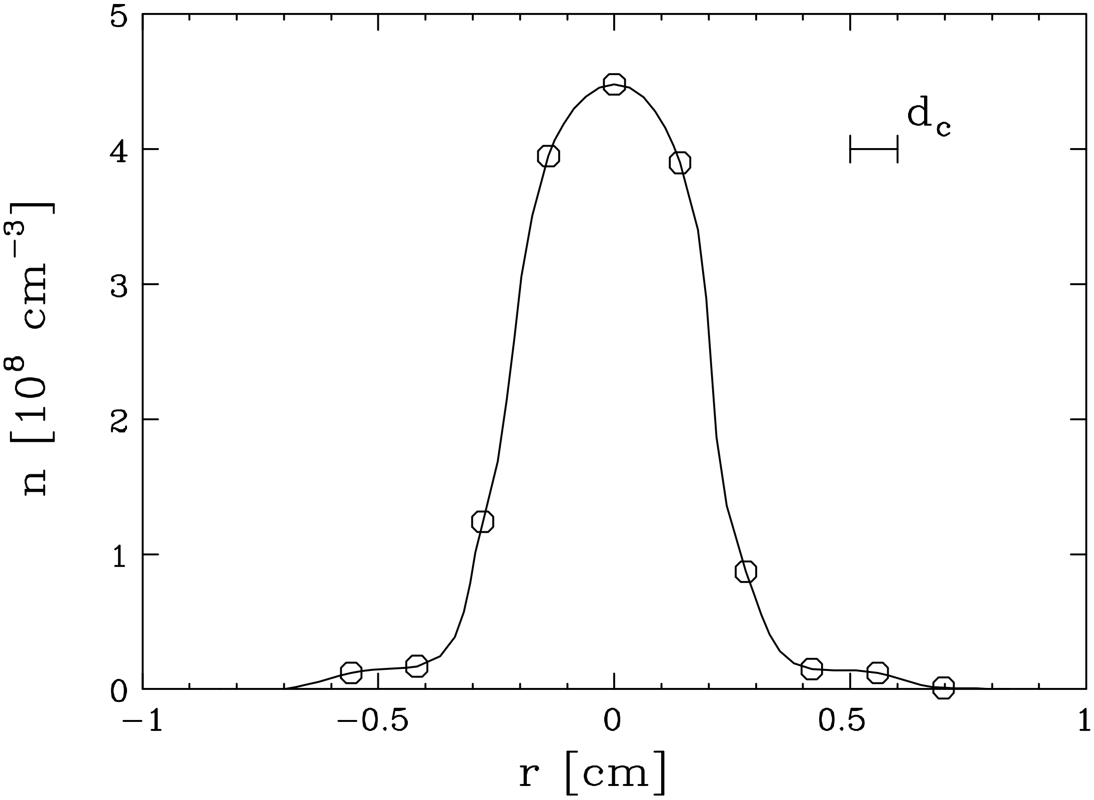

Figure 2.6: Radial density profile of electron plasma measured using collimator hole.

In electron plasmas, we also use the charge collection diagnostic to measure the parallel thermal energy $T_{\|}$. In this case, the collimator plate is removed, and the confining voltage is lowered at a rate $\nu_{dump} \equiv -(\partial V_c/\partial t)/T$ which is slow compared to the axial bounce frequency of a thermal particle but fast compared to the electron-electron collision rate. For a typical electron plasma experiment, for example, we have $n \simeq 5 \times 10^8\,\mathrm{cm}^{-3}$, $L_p \simeq 35$ cm, and $T \simeq 1$ eV, giving a thermal bounce frequency $f_b \equiv 2L_p/v \approx 6 \times 10^5\,\mathrm{s}^{-1}$ and an electron-electron collision rate $\nu_{ee} \equiv \frac{16}{15}\sqrt{\pi}\,(nvb^2)\ln(r_c/b) \approx 6 \times 10^3\,\mathrm{s}^{-1}$ (where $b \equiv e^2/T$ is the distance of closest approach of a thermal particle and $r_c = v/\Omega_c$ is the cyclotron radius). For these plasma parameters, we typically lower the end confinement potential of $V_c = 200$ V linearly in 20 ms, giving $\nu_{dump} \approx 10^4\,\mathrm{s}^{-1}$, so the condition $\nu_{ee} < \nu_{dump} < f_b$ is satisfied. With this inequality satisfied, the parallel electron temperature near the center of the plasma $T_{\|}(r \simeq 0)$ can be obtained from the measured collected charge as a function of time, $Q_F(t)$, since this signal reflects a sampling of the Maxwellian tail of the parallel thermal energy. This method of measuring electron temperature was developed extensively in previous experiments [22, 5].

2.4.3 Image Charge Diagnostic

The third diagnostic used in these experiments is the measurement of voltages induced on the conducting wall by the plasma. This is an essentially nondestructive diagnostic, and is the dominant diagnostic used here for the detection of modes which have been launched in the plasma.

The simplest example of an image charge diagnostic is the detection of the $m_\theta = 1$ "diocotron" mode. This is the mode in which the entire plasma column is translated off-axis and then $\mathbf{E} \times \mathbf{B}$ drifts about the trap axis under the influence of the image charges induced on the conducting trap walls. The image charge can be measured by "listening" to a wall sector (such as S11a on Figure 2.2, for example) with an amplifier. For small off-axis displacements, the image charge voltage oscillates at a frequency f_1 is given by:

$$\begin{aligned} f_1 &\simeq \frac{N_L}{\pi} \frac{ec}{BR_w^2} \\ &\approx (560\,\mathrm{s}^{-1}) \left(\frac{N_L}{10^7\,\mathrm{cm}^{-1}}\right) \left(\frac{B}{1\,\mathrm{T}}\right)^{-1} , \end{aligned} \tag{2.8}$$

where the line charge density is $N_L \equiv 2\pi \int n(r) r dr$. Measurement of the $m_\theta = 1$ diocotron frequency f_1 thus gives the value of the line charge density N_L. Here, we use the measurement of this mode frequency primarily as a double-check of the other diagnostics.

The $m_\theta = 1$ diocotron mode is found to self-excite and grow spontaneously in our electron plasma experiments, often causing an electron plasma to be lost to the wall on a time scale of several seconds. To avoid this, we generally measure and apply negative feedback to this mode using two wall sectors on ring S5. No self-excitation of this mode is seen in our ion plasmas.

2.5 Plasma Manipulations

2.5.1 Laser Heating/Cooling

In addition to serving as a useful diagnostic tool, laser beams with sufficient power can be used to manipulate the plasma temperature. Laser cooling was independently developed for ions bound in an electromagnetic trap [63] and for a gas of neutral atoms [26]. It has since become a standard technique in atomic physics, where cooling is highly desirable for the minimization of Doppler-broadening of transitions [65]. Here, we use laser cooling and laser heating as tools for increasing the temperature range over which plasma effects can be studied, and for creating temperature gradients in the plasma.

We use the simplest form of laser heating (or cooling) in our Mg^+ plasmas, based on the first-order Doppler shift. This form of heating is usable for ions with temperatures greater than ion-recoil limit, which is set by the linewidth $\Delta\nu_0$ of the atomic transition used; here the limiting temperature is $T_D \equiv h\Delta\nu_0/2 \simeq 10^{-7}$ eV, which is far below the temperature range discussed in this thesis, $10^{-4} < T < 10$ eV.

Laser heating or cooling occurs due to the small average change in ion energy which occurs in the absorption/re-emission process. To perform laser heating or cooling, we use a parallel ($\hat{z}$-aligned) laser beam. Referring to Figure 2.7, an ion absorbs a photon with momentum $h\mathbf{k} = (h/\lambda_0)\hat{z}$ and then immediately re-emits a photon with momentum $h\mathbf{k}'$. The emission process for the transitions used here follows a $I(\xi) = 1 + \cos^2\xi$ intensity distribution, where ξ is the angle between $\mathbf{k}'$ and $\hat{z}$. Thus, on average, no net momentum is lost in emission. The average momentum change of the ion is then $\Delta\mathbf{p} = h\mathbf{k}$ and the average energy change, ignoring the small

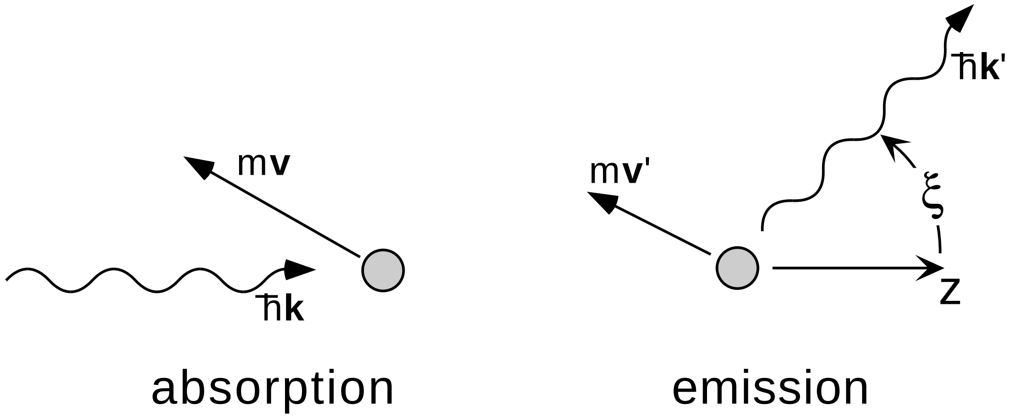

Figure 2.7: Illustration of photon absorption and re-emission, showing net momentum transfer to ion in $\hat{z}$-direction.

ion recoil energy, is $\Delta T_{||} \simeq \hbar \mathbf{k} \cdot \mathbf{v}$, where $\mathbf{v}$ is the ion velocity vector. For a Mg^{+} ion at $T = 1$ eV absorbing/re-emitting a $\lambda_0 = c/\nu_0 \simeq 280$ nm photon, this gives $\Delta T_{||} \simeq 3 \times 10^{-5}$ eV. Thus, of order 10^5 photon-ion collisions are necessary to cause substantial change of the ion energy. It is apparent that a cyclic transition must be used for useful laser heating or cooling of the ion.

To achieve laser heating of the plasma, the laser is detuned to the "blue" side of a cyclic transition ($\delta\nu > 0$); to achieve laser cooling, the laser is detuned to the "red" ($\delta\nu < 0$) side of the transition frequency ν_0. In the case of laser heating (laser frequency blue-shifted from resonance), ions moving away from the laser beam (in direction $\mathbf{k}$) are red-shifted back into resonance; so these ions absorb photons, giving $\Delta T_{||} \simeq \hbar \mathbf{k} \cdot \mathbf{v} > 0$, and the ions gain parallel energy. Conversely, in the case of laser cooling, ions moving toward the laser beam are Doppler-shifted into resonance, so $\Delta T_{||} < 0$ and ions loose parallel energy. For a Maxwellian distribution of velocities, the heating/cooling rate can be estimated to be proportional to $\delta\nu \exp[-(\delta\nu/\Delta\nu)^2]$, so the most efficient heating/cooling is expected to occur around $\delta\nu \simeq \Delta\nu$, i.e. if

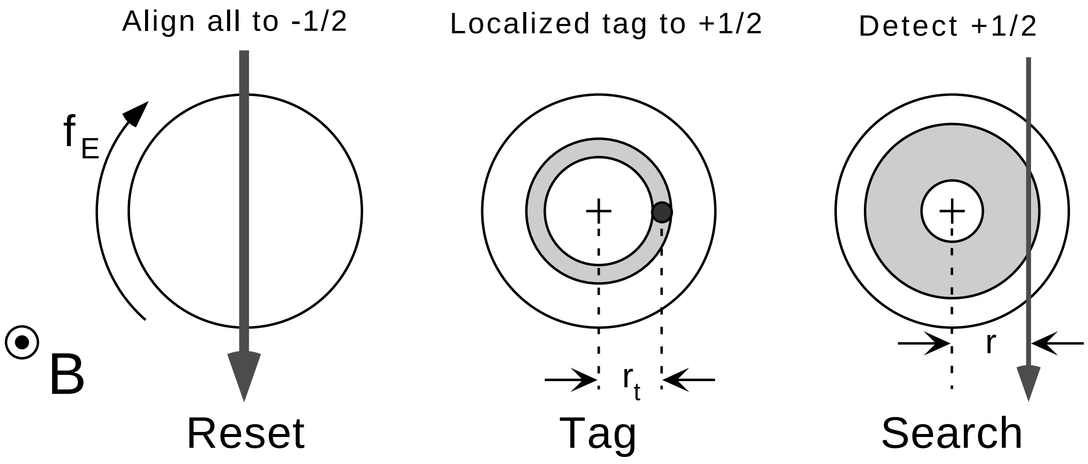

Figure 2.8: Experimental sequence used for test particle transport measurements.

the laser is detuned off resonance by the thermal broadening of the transition [64]. We observe this to be true in practice, so effective laser cooling/heating over a wide range of temperatures often requires modification of the laser detuning $\delta\nu$ as the plasma temperature changes.

2.5.2 Spin State Tagging

As described in Section 2.4.1, the ions in magnesium plasmas can be placed into either the $(3S_{1/2}, m_j = +1/2)$ or the $(3S_{1/2}, m_j = -1/2)$ ground state by driving an optical pumping transition with a laser. "Spin state tagging" refers to an experiment where a localized group of ions is placed in the opposite spin state as the rest of the plasma. These "test-particles" can then be observed with a diagnostic beam as they mix with the other ions in the plasma. Tagging of ions in a plasma was first demonstrated by Skiff *et al.* [56].

Spin state tagging typically requires very little laser power compared to laser heating/cooling. As discussed in the previous section, 10^5 photon-ion interactions are typically necessary to laser heat or cool a single ion in these experiments. By comparison, only several collisions are necessary, on-average, to spin-polarize an ion.

The tagged particles can be localized in either real-space or velocity-space; here we are concerned with real-space test-particle transport. A schematic of a spin state tagging sequence and test-particle transport experiment are shown in Figure 2.8. Here, the plasma cylinder is illustrated end-on. Three steps are required: in the first step (Reset), the plasma is completely spin-polarized into the -1/2 state by driving the peak of the $(3S_{1/2}, m_j = +1/2) \rightarrow (3P_{3/2}, m_j = -1/2)$ optical pumping transition. The beam passes through the center of the plasma perpendicular to the magnetic field. The beam is left on for a time ($\approx$ 10 s) which is long compared to the collision time, bounce time, and rotation time of the plasma; this ensures that all the ions in the plasma have interacted with the beam. In the second step (Tag), the spins of the particles at a chosen radial position r_t are reversed using a beam aligned parallel to the magnetic field. The beam is tuned to the peak of the $(3S_{1/2}, m_j = -1/2) \rightarrow (3P_{3/2}, m_j = +1/2)$ optical pumping transition and is left on for a time (typically 50 ms), which is long compared to the plasma rotation, bounce, and collision time scales, but short compared to the radial diffusion and spontaneous spin-depolarization times of the test particles. A large fraction (typically about 80%) of the ions in a shell at $r = r_t$ are thus pumped into the $+1/2$ ground state. In the third step (Search), the radial diffusion of this shell of test particles is monitored at some radius r with a probe beam tuned to the peak of the $(3S_{1/2}, m_j = +1/2) \rightarrow (3P_{3/2}, m_j = +3/2)$ cyclic transition.

2.5.3 Driving Electrostatic Modes

The third method of plasma manipulation used here is the launching of electrostatic modes in the plasma. As a mode is damped, the mode transfers its energy and angular momentum to the plasma, so driving electrostatic modes in the plasma can be an efficient method for changing the plasma energy and angular momentum.

Modes in these plasmas generally have density perturbations δn and potential perturbations $\delta\Phi$ which have the form $\delta n, \delta\phi \propto e^{ik_z z} e^{im_\theta \theta} e^{i\omega t}$, where $k_z \simeq m_z \pi / L_p$, with m_z, m_θ being integers. Modes with azimuthal dependence ($m_\theta \neq 0$) are launched using the sectored rings S5 or S11; $m_\theta = 0$ modes can be launched with any of the confinement rings. We refer to a rotating electrostatic perturbation applied using the sectored rings as a "rotating wall". We use positive m_θ to describe an applied perturbation which rotates in the same sense as the plasma rotation f_{tot}; $m_\theta < 0$ indicates a perturbation rotating in the opposite sense. To apply a $m_\theta = +2$ perturbation to the plasma, for example, a voltage $A_s \cos \omega_s t$ is applied to sector S11a and S11e, a voltage $A_s \cos(\omega_s t - \pi/2)$ is applied to S11b and S11f, a voltage $A_s \cos(\omega_s t + \pi)$ is applied to S11c and S11g, and a voltage $A_s \cos(\omega_s t + \pi/2)$ is applied to S11d and S11h (referring to Figures 2.2 and 2.9). Using the angular size of these sectors ($\Delta\phi_s \simeq 29°$), one finds that the resulting potential perturbation can be Fourier-decomposed in the θ-direction to give an applied potential $\delta\Phi$ at the wall $r = R_w$ of:

$$\begin{aligned} \delta\Phi(t, r = R_w) \simeq\ & .31 A_s \cos(2\theta - \omega_s t - 3\pi/4) + .21 A_s \cos(6\theta + \omega_s t - 5\pi/4) \\ & + .07 A_s \cos(10\theta - \omega_s t - 7\pi/4) + \ldots . \end{aligned} \tag{2.9}$$

The signal at $r = R_w$ therefore consists of an amplitude $.31 A_s$ wave moving in the θ-direction ($m_\theta = +2$); the next largest component being a $.21 A_s$ wave moving in the $-\theta$ direction ($m_\theta = -6$). At the plasma radius $r = R_p$, the relative magnitudes of these two signals will be: $\delta\Phi_{m_\theta=-6}(r = R_p) / \delta\Phi_{m_\theta=+2}(r = R_p) \simeq .7\,(R_p/R_w)^4$. Typically, we have $R_p/R_w \simeq .2$, so $\delta\Phi_{m_\theta=-6}(r = R_p)/\delta\Phi_{m_\theta=+2}(r = R_p) \simeq 10^{-3}$. The plasma therefore sees an almost pure $m_\theta = +2$ perturbation. A similar method can be used to create a $m_\theta = +1$ perturbation; in this case the largest harmonic is $m_\theta = -5$ (if 8 sectors are used), $m_\theta = -3$ (if 4 sectors are used), or $m_\theta = -1$ (if 2 sectors are used).

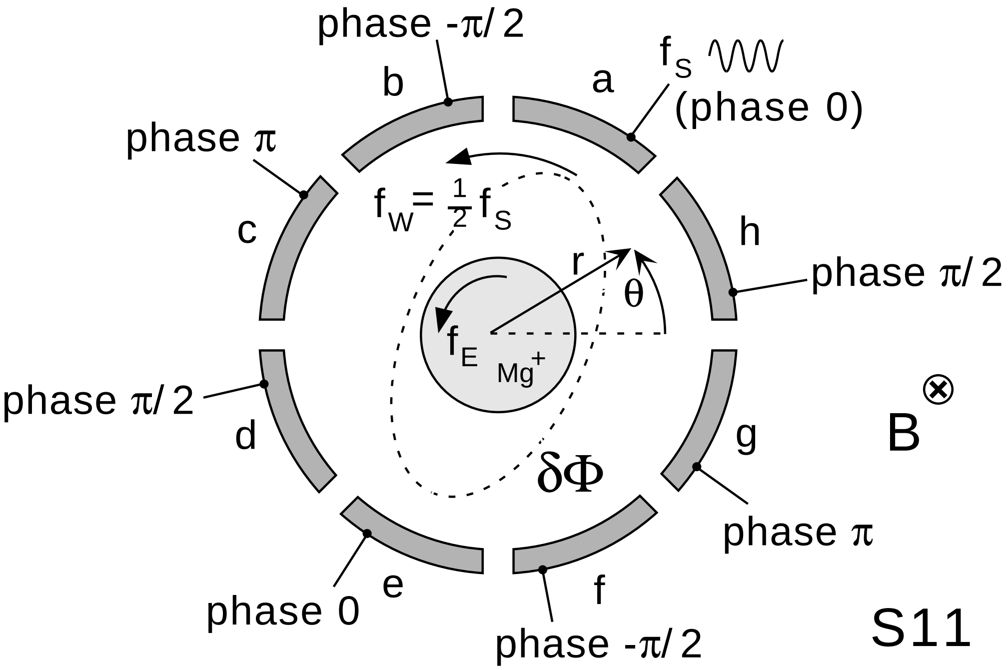

Figure 2.9: Schematic of $m_\theta = +2$ rotating wall setup for ions.

These applied perturbations rotate at a frequency f_w given by

$$f_w = f_s/m_\theta \ , \tag{2.10}$$

so the $m_\theta = 2$ perturbation of Figure 2.9, for example, rotates at $f_w = \frac{1}{2}f_s$.

The modes which are used in this work are the nonneutral analog of Trivelpiece-Gould modes [59]. Trivelpiece-Gould modes are electrostatic waves originally derived to describe waves in a plasma-filled waveguide. They also occur in nonneutral plasmas, the primary difference being a Doppler-shift in the lab-frame mode frequency due to the plasma rotation. For nonneutral plasmas far below the Brillouin limit, these modes can be grouped into three categories: diocotron modes, plasma modes, and cyclotron modes.

Diocotron modes are low-frequency ($\omega \sim \omega_E$) modes. We use the $m_\theta = 1$ diocotron mode primarily as a method of obtaining the plasma line-charge density, as described in Section 2.4.3. Diocotron modes have been studied extensively in previous experiments done in this group [24].

Plasma modes are intermediate-frequency ($\omega \sim \omega_p$) modes. We launch plasma modes in both electron and Mg^+ plasmas as a means of causing plasma heating and as a way of changing the plasma angular momentum. As expected, the $m_\theta = 0$ plasma modes are found to cause heating but no change in the plasma angular momentum, while $m_\theta \neq 0$ plasma modes are found to change both the plasma temperature and the plasma angular momentum. We often refer to the use of a $m_\theta = 0$ perturbation to heat the plasma as "wiggle heating". Since the plasma modes are at a frequency small compared with the cyclotron frequency, we expect heating from these modes to affect primarily the parallel plasma temperature. This is observed experimentally: in general, plasmas with applied wiggle heating are found to have a parallel temperature which is higher than the perpendicular temperature, i.e. $T_{\|} > T_{\perp}$. This anisotropy can be an undesirable characteristic of wiggle heating; it is desirable, however, for measuring the relaxation rate of an anisotropy between the parallel and perpendicular degrees of freedom, as is discussed in Chapter 4. The use of driven $m_\theta \neq 0$ plasma modes to change the plasma angular momentum is discussed in Chapter 3.

Cyclotron modes are high-frequency ($\omega \sim \Omega_c$) modes. Preliminary experiments indicate strong heating and little or no compression from $m_\theta = +1$ cyclotron modes and neither heating nor compression from $m_\theta = -1$ cyclotron modes. We have used driven cyclotron modes as a tool for heating Mg^+ plasmas; we usually refer to this as ion-cyclotron resonance heating (ICRH). These modes have also been used to perform cyclotron resonance spectroscopy, i.e. to determine the masses of the ions present in the plasma [54].

Chapter 3

Rotating Wall Confinement Technique

3.1 Overview

In this chapter, we demonstrate that the application of rotating electric fields to these plasmas allows us to achieve density control and steady-state confinement.

As discussed in Section 2.2, background neutral gas and imperfections in the trap symmetry exert a drag on nonneutral plasmas in Penning-Malmberg traps, slowing the plasma rotation and causing radial expansion and particle loss. Two methods which have been used in other experiments to counter this expansion are laser torquing and "side-band cooling". Laser torquing uses a laser beam aimed at the edge of the plasma in the direction of the plasma rotation to spin-up the plasma through transfer of momentum from the laser beam to the plasma. This method relies on the presence of an accessible atomic transition, thus being limited to a small number of ion species. Also, fluctuations in laser power, frequency, and pointing can make this method difficult to implement. Laser torquing has been used to provide steady-state confinement of 10^3 to 10^6 Be^+ ions in harmonic Penning traps [27]. Side-band cooling uses an applied rf field to parametrically couple the magnetron (rotation) motion with the collective axial bounce motion of a small plasma in a harmonic Penning trap. The bounce motion is then resistively cooled, which results in cooling of the magnetron motion and suppressed radial expansion. Side-band cooling has been used to compress 10^3 to 10^4 electrons trapped in harmonic wells [62]. This method becomes ineffective for large trapped plasmas, however, as the magnetron motion and collective bounce motion become dominated by plasma space-charge effects.

It has been found that the application of a rotating electric field, or "rotating wall" can provide steady-state confinement for small (about 10^6 ions) spheroidal Be^+ plasmas in harmonic traps [29]. In these experiments, the applied rotating electric field has very little axial dependence, being nearly uniform over the entire length of the plasma. These plasmas are cooled to a strongly-correlated state ($T \simeq 10$ mK) and are found to rotate phase-locked to the applied drive.

It is well-known that plasma waves can greatly enhance particle transport. Both spheroidal plasmas and long plasmas show strong confinement degradation when applied perturbations coincide with a plasma mode [43, 23]. In a long electron plasma at low magnetic field ($B \leq 400$ G), modest density and angular momentum increases were reported when the applied perturbation excited a plasma mode, but a large amount of heating was observed and background ionization made the technique impractical [42]. Compression of small spheroidal plasmas has been performed by driving plasma modes with an applied rotating electric field. This mode-enhanced rotating wall drive is observed to cause a larger torque and larger heating than is obtained with the phase-locked (non-modal) rotating wall mentioned in the previous paragraph [41].

We have found that the application of rotating electric fields to long nonneutral plasma columns can provide sufficient torque to provide density compression and steady-state confinement at central densities of up to about 10^9 cm^{-3} for electrons [1] and 5×10^8 cm^{-3} for ions [28]. The torque is measured on electron plasmas ranging in temperature from $T \simeq 0.2$ to 2 eV and on ion plasmas ranging from $T \simeq 10^{-4}$ to 4 eV. We find that a large enhancement in the torque is observed when the rotating wall frequency is chosen such that a Trivelpiece-Gould mode with length dependence ($k_z \neq 0$) and with azimuthal dependence ($m_\theta \neq 0$) is excited in the plasma. As discussed in Section 2.5.3, these modes can be grouped into diocotron (low-frequency), plasma (intermediate-frequency), and cyclotron (high-frequency modes); here, we present results obtained for plasma (intermediate-frequency) modes.

In Section 3.2, frequency measurements of these plasma modes are obtained from wall sector signals (mode transmission experiments). The observed mode frequencies are found to be in reasonably good agreement with numerical predictions. Next, in Section 3.3, measurements of the plasma density compression and expansion resulting from these modes are presented. Large peaks in the rotating wall torque are observed at the mode frequencies; no significant torque is obtained off-resonance. Modes rotating faster than the plasma are found to cause a positive torque, while modes rotating slower than the plasma are found to cause a negative torque (drag) on the plasma. The mode torque is found to scale linearly with applied drive amplitude, indicating a nonlinear coupling.

In Section 3.4, measurements of the mode damping rate are presented; the damping rate is found to be fairly constant as a function of temperature, in disagreement with predictions of linear Landau damping.

Section 3.5 shows measurements of the background expansion rate for these plasmas. The background expansion rate represents the drag on these plasmas which needs to be overcome by the rotating wall torque in order to provide compression and steady-state plasma confinement. Here, we find an electron plasma background expansion rate which scales like n_0^2, where $n_0 \equiv n(r = 0)$, consistent with measurements on previous machines. An ion plasma background expansion rate which is independent of density n_0 and temperature T is observed, which is not consistent with observations on previous machines.

3.2 Measurement of Plasma Mode Frequencies with Transmission Experiments

Azimuthally-dependent modes are driven and detected in these plasmas using the azimuthally-sectored confinement rings S5 and S11, as described in Sections 2.4.3 and 2.5.3. Two typical mode transmission experiments are shown in Figure 3.1. In Figure 3.1(a), $m_\theta = 1$ modes are launched in an electron plasma confined in the region S5→S11. A signal with frequency f_s and amplitude $A_w = 67$ mV is applied to sector S11a and a 180° phase-shifted signal with the same amplitude is applied to S11e. This way, both forwards and backwards propagating harmonics ($m_\theta = \pm 1$) are driven in the plasma. At the other end of the plasma, sector S5a is connected to a spectrum analyzer with a bandwidth of 300 Hz, centered about the drive frequency, f_s. After an electron plasma is injected, the drive frequency is ramped in 100 seconds from $f_s = 0.5$ to 2.5 MHz and the received signal is monitored on the spectrum analyzer.

We observe an enhancement in the signal transmission of up to about 40 dB when the drive frequency corresponds to a plasma mode frequency. We have a noise floor of about -130 dBm, corresponding to a noise signal of about 0.07 $\mu\mathrm{V_{rms}}$. 40 dB enhancement over the noise therefore corresponds to a received voltage $A_{rec} \simeq$ 7 $\mu\mathrm{V_{rms}}$. The plasma used here had parameters $L_p \simeq 35$ cm, $R_p \simeq 0.25$ cm, $n_0 \simeq 4 \times 10^8\,\mathrm{cm}^{-3}$, $T \simeq 0.1$ eV, and $N_{tot} \simeq 2.7 \times 10^9$. The plasma is expanding slowly during this measurement, with the total number of particles remaining constant, but this is not believed to affect the mode frequencies significantly since the plasma rotation frequency $f_E \simeq 140$ kHz is small compared to the mode frequencies.

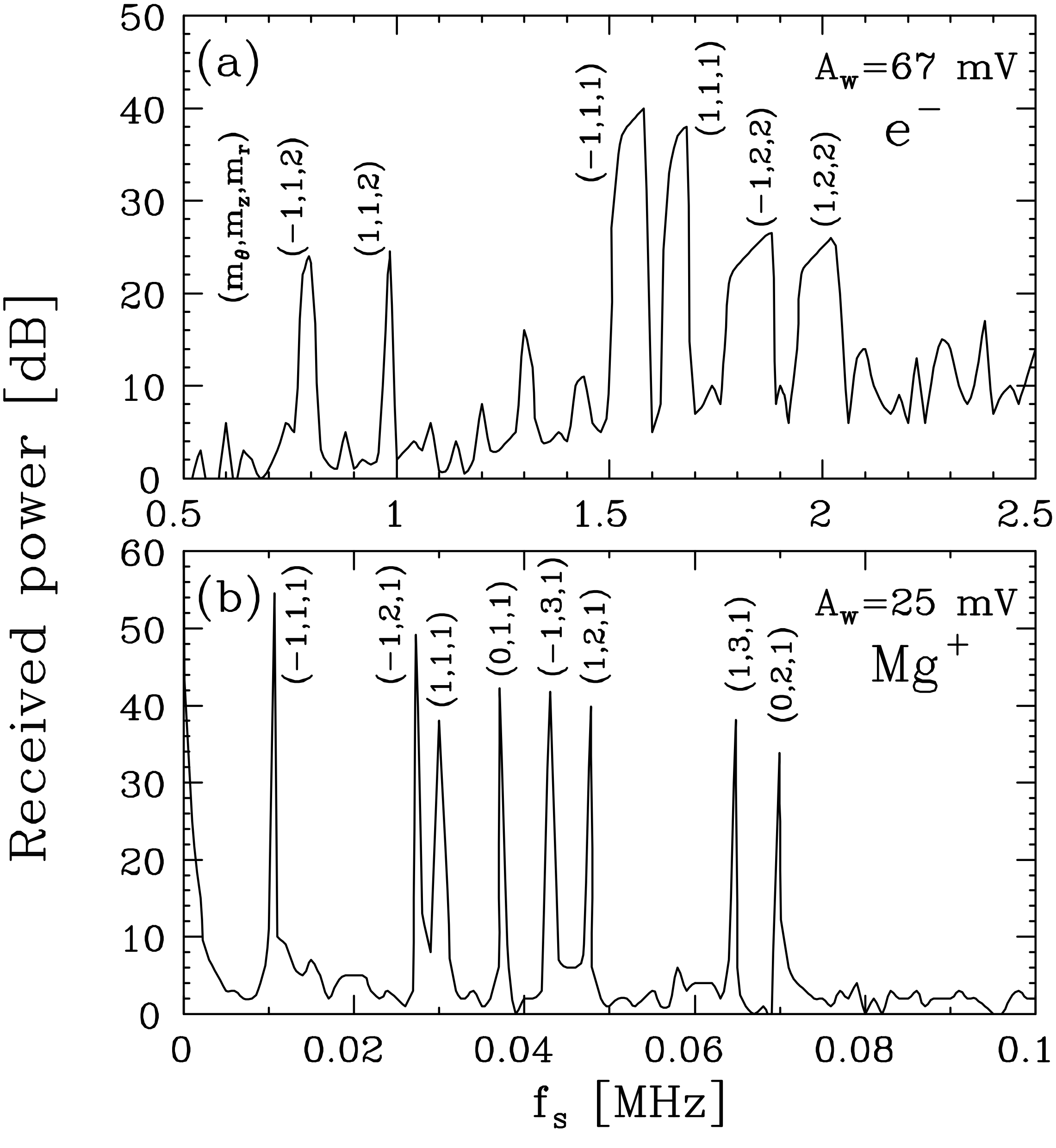

Figure 3.1: Small amplitude $m_\theta = \pm 1$ mode transmission experiment on electron (a) and ion (b) plasmas.

Figure 3.1(b) shows a similar transmission experiment performed on a magnesium ion plasma. Here, the plasma is kept from expanding by the application of a $f_w = 20$ kHz, $A_w = 0.4$ V, $m_\theta = +1$ rotating wall drive using the sectors on S11a, c, e, and g; this balances the inherent asymmetry drag on the plasma by coupling to the (1,1,1) mode, as will be described in the next section. A $m_\theta = \pm 1$, $A_w = 25$ mV signal is applied using sectors S11b and f. This drive signal is ramped in frequency from 0 to 100 kHz in 100 seconds while listening to sector S11d with the spectrum analyzer. As for the electron plasma, strong enhancement in the received power is observed when the drive frequency f_s corresponds to a plasma mode. Additionally, a strong peak is observed at $f_s = 20$ kHz because of direct coupling between sectors; this peak is observed even without a plasma, however, and is subtracted from the data presented in Figure 3.1(b). The plasma used here had parameters $n_0 \simeq 4.3 \times 10^7\,\mathrm{cm}^{-3}$, $L_p \simeq 14.5$ cm, $R_p \simeq 0.66$ cm, and $T \simeq 0.1$ eV.

The mode identifications in Figure 3.1 use the notation (m_θ, m_z, m_r). These identifications are obtained from numerically predicted mode frequencies. A reinforcement of the numerically obtained mode identifications of Figure 3.1 is achieved by performing several simple antenna configuration tests: the $m_\theta = -1$ modes are no longer observable when a forwards-phased $(m_\theta = +1)$ drive is used; similarly, the $m_\theta = +1$ modes are no longer observed when a reverse-phased $(m_\theta = -1)$ drive is used. Also, these modes could not be excited by a $m_\theta = 0$ or $m_\theta = 2$ drive. These results are consistent with the m_θ mode labels of Figure 3.1. For the long electron plasma, Figure 3.1(a), when driving the $m_\theta = 1$ modes while listening with two opposing sectors, S5a and S5c, connected together, no transmission peaks are observed. This verifies that the modes observed in Figure 3.1(a) correspond to an odd azimuthal mode number m_θ. Additionally, when driving $m_\theta = \pm 1$ modes and listening with sectors S11f, S11g, and S5d connected together, the mode peaks labeled by odd m_z numbers on Figure 3.1(a) are observed to drop by about 15 dB, while the mode peaks labeled by even m_z numbers where observed to rise by about 5 dB. Conversely, if sectors S11f, S11g, and S5b connected together are used for listening to the modes, the mode peaks labeled by even m_z numbers are observed to drop by about 15 dB while the mode peaks labeled by odd m_z numbers were observed to rise by about 5 dB. Together with the knowledge that these modes have odd azimuthal symmetry, this verifies that the modes in Figure 3.1(a) labeled with odd m_z are indeed odd in z, while the modes labeled with even m_z are indeed even in z. Additionally, for the ion plasma, Figure 3.1(b), coherent detection of the ion fluorescence at a given mode frequency was used to verify the expected radial mode shapes of the $m_\theta = 0$ and $m_\theta = 1$ modes as well as the odd vs. even nature of the $m_z = 1$, 2, and 3 modes.

The $m_\theta = 0$ modes seen in Figure 3.1(b) are driven by small imbalances in the nominally $m_\theta = \pm 1$ applied signal; in general, $m_\theta = 0$, $m_r = 1$ modes are found to be very easily driven in these plasmas. The identification of these modes is obtained from numerical predictions and by independent transmission experiments using a $m_\theta = 0$ drive. The associated modes with higher radial mode number, such as (0,2,2) and (0,1,2), are more difficult to excite and are only observed here when a strong $m_\theta = 0$ drive is applied to the plasma. In Figure 3.1(a), the (0,1,1) and (0,2,1) modes are off the horizontal scale, occurring at about 5 and 10 MHz, respectively.

We find that the measured frequencies of $m_\theta = 0$ and $m_\theta = 1$ modes are in reasonable agreement (typically within about 10%) with numerical solutions based on drift-kinetic theory (Equation B.3 of Appendix B). For $m_\theta = 2$ modes, the agreement between observed and numerically calculated frequencies is not as good (typically within 30%). The analytical solution of the mode dispersion relation for a top-hat density profile and small wavenumber k_z (Equation B.5) provides a good prediction of the $m_\theta = 0$ modes (typically within 10%), but is not as reliable for predicting the $m_\theta = 1$ or 2 modes (often incorrect by 50% or more).

Equation B.5 predicts a scaling for the mode angular frequency ω of:

$$\omega - m_\theta \omega_E \simeq \pm \frac{1}{j_{m_\theta m_r}} \omega_p R_p k_z \ , \tag{3.1}$$

where $j_{m_\theta m_r}$ is the m_rth zero of the m_θth Bessel function, and we have ignored the weak temperature dependence of these modes. Since $\omega_p R_p k_z \propto N_L^{1/2} L_p^{-1}$, we expect the Doppler-shifted mode frequencies to be inversely proportional to plasma length for fixed line density N_L.

The scaling of Equation 3.1 is verified experimentally: in Figure 3.2, we plot the mode frequencies $f = \omega/2\pi$ observed in transmission experiments as a function of the square root of the line density divided by the plasma length, $N_L^{1/2} L_p^{-1}$. The drive amplitude in these experiments is small ($A_w \le 25$ mV), so the temperature remains low ($T \simeq 0.1$ eV). The symbols correspond to the measured mode frequencies. In Figure 3.2(a), electron plasmas with lengths $L_p \simeq 17.5$, 23.4, 35.0, and 40.9 cm were used; the corresponding line-charge density was nearly constant: $N_L \simeq 10.0$, 9.0, 8.3, and $7.6 \times 10^7\,\text{cm}^{-1}$. The $\mathbf{E} \times \mathbf{B}$ rotation frequency, $f_E \simeq 150$ kHz, was small for the experiments of Figure 3.2(a). The lines through the data are numerical solutions of Equation B.3; dashed lines represent even m_z modes, while solid lines represent odd m_z modes. It can be seen that the observed modes are well-described by the numerical solutions. Also, it is apparent that the approximation $\omega - m_\theta \omega_E \propto N_L^{1/2} L_p^{-1}$ is reasonable for these plasmas.

Figure 3.2(b) shows that Equation 3.1 also holds for Mg$^+$ plasmas. Here, ion plasma lengths of $L_p \simeq 8.4$, 12.5, and 17.6 cm were used. The corresponding line-charge density values were $N_L \simeq 3.4$, 2.2, and $1.4 \times 10^7\,\text{cm}^{-1}$, respectively. As for the electron plasmas of Figure 3.2(a), it can be seen that the observed modes are well-described by the numerical solutions and that the approximation $\omega - m_\theta \omega_E \propto$

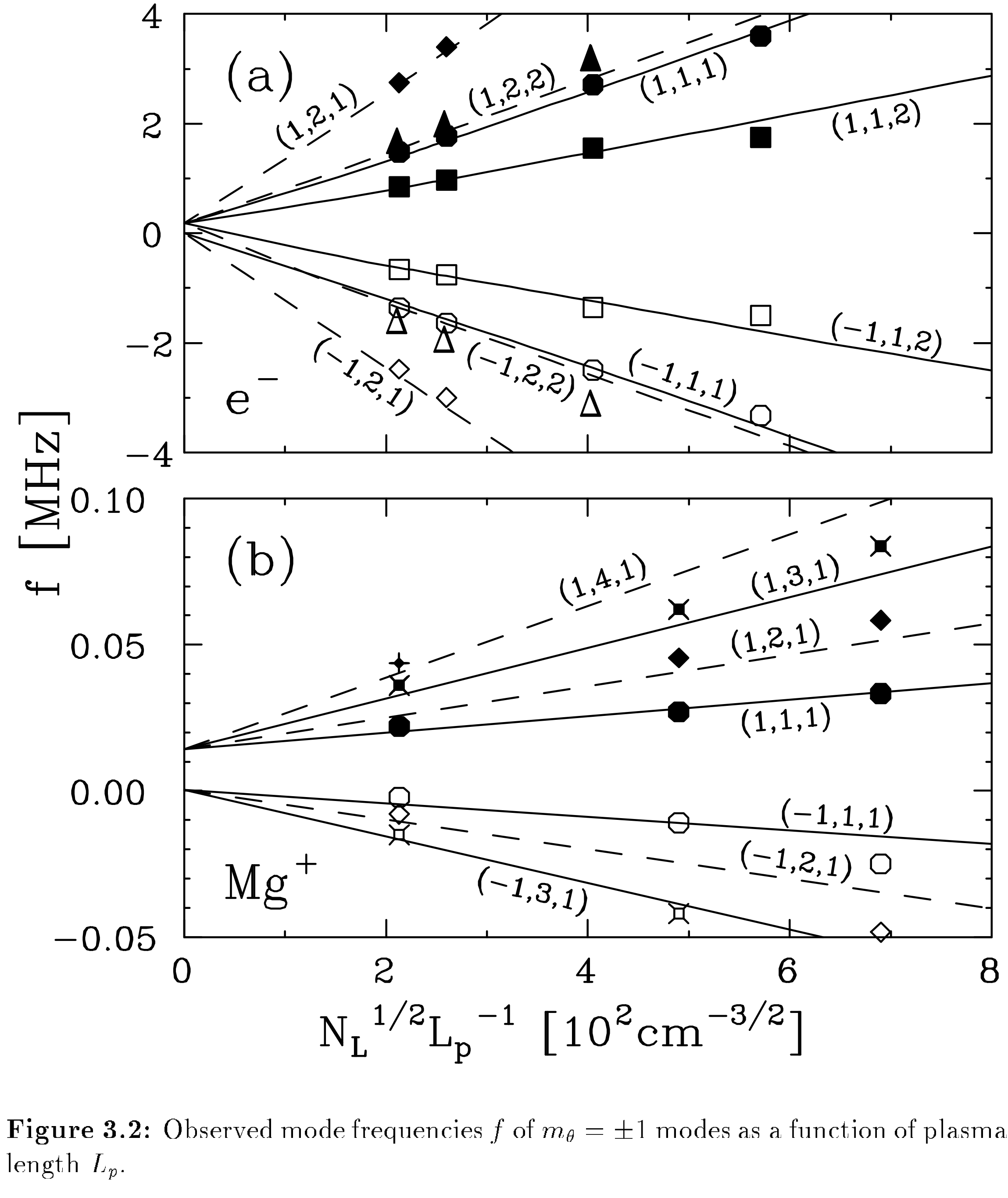

Figure 3.2: Observed mode frequencies f of $m_\theta = \pm 1$ modes as a function of plasma length L_p.

$N_L^{1/2} L_p^{-1}$ is reasonable for these plasmas. For the ion plasmas, the $\mathbf{E} \times \mathbf{B}$ rotation frequency $f_E \simeq 14$ kHz is not negligible compared to the mode frequencies; this can be seen from the f_E offset of the predicted $m_\theta = +1$ modes at $k_z = 0$.

A slight upward shift in the mode frequencies is to be expected as the plasma temperature increases (from the $(v/v_\phi)^2 \propto T$ term of the analytical solution, Equation B.5); this shift is expected to be more pronounced for modes with larger axial phase velocity $v_\phi \equiv (\omega - m_\theta \omega_E)/k_z$. This is found to be true in practice: the observed mode frequencies are seen to shift upward with increasing T. This shift is larger for modes with smaller phase velocities; $m_\theta = 0$ modes, for example, which tend to have a larger phase velocity, are observed to shift only slightly with increasing temperature, while $m_\theta = 1, m_r = 2$ modes, for example, which tend to have a lower phase velocity, are observed to shift more with increasing temperature.

Figure 3.3 shows the observed frequencies f of three $m_\theta = 1$ modes as a function of plasma temperature T. Aside from the temperature, the parameters are the same as for the plasma used in Figure 3.1(a). Plasma heating was obtained by applying a sine wave signal on ring R10 at 0.8 MHz (far off $m_\theta = 0$ resonance) at an amplitude of up to $A_w = 1$ V; this gave plasma temperatures ranging between 0.1 and 1.5 eV. This heating could result from weak excitation of $m_\theta = 0$ modes; similar temperatures can be obtained by using a lower amplitude $m_\theta = 0$ drive on-resonance (by driving the (0,1,1) mode at $f \simeq 5$ MHz, for example), but the higher-amplitude, off-resonance $m_\theta = 0$ heating was found to be more stable in practice. Presumably, heating might also be occuring as a result of single-particle effects, such as adiabatic, resonant particle, or stochiastic heating [10, 11].

In Figure 3.3, it can be seen that the $m_\theta = 1$ modes shift upwards slightly as the plasma temperature is increased. As predicted by the analytical solution, this shift is stronger for modes with lower phase velocity ($m_r = 2$). The lines in Figure 3.3

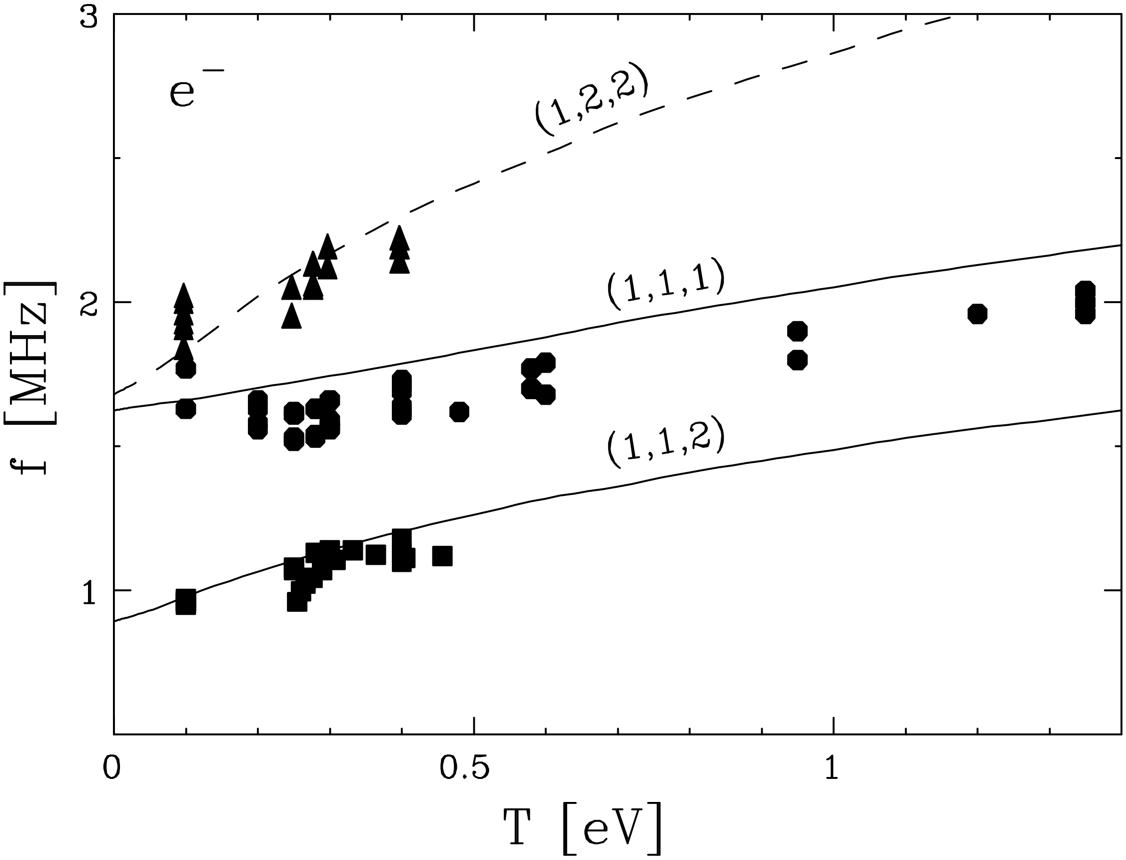

Figure 3.3: Dependence of $m_\theta = 1$ electron plasma mode frequencies on plasma temperature T.

are the numerical predictions of Equation B.3; it can be seen that the observed temperature variation is captured reasonably well by the numerical solution.

3.3 Measurements of Torque from Driven Plasma Modes

Since the plasma angular momentum is proportional to $\langle r^2 \rangle$ (Equation 2.1), we can measure the torque on a plasma by measuring the rate of change of the mean-square radius, i.e. $\dot{\langle r^2 \rangle}$. For a plasma which evolves self-similarly, measurement of the rate of change of the central density $\dot{n}_0$ is sufficient, since, in this case, $\dot{n}_0/n_0 = -\dot{\langle r^2 \rangle}/\langle r^2 \rangle$. In practice, we typically observe $\dot{n}_0/n_0 = -\dot{\langle r^2 \rangle}/\langle r^2 \rangle$ to be satisfied within a factor 3, so measuring the rate of change of central density can be expected to give a qualitative measure of the torque on the plasma.

Figure 3.4 shows examples of radial density profiles $n(r)$ resulting from mode-driven plasma expansion and compression. For each profile, the symbols indicate actual data; the lines are smooth fits to the data. In Figure 3.4(a), profile B shows a typical electron plasma ($L_p \simeq 35$ cm and $N_{tot} \simeq 2.7 \times 10^9$) measured 5 seconds after injection. Profile A shows the same electron plasma after being expanded by driving a backwards-rotating mode; and profile C shows the same electron plasma after being compressed by a forwards-rotating mode.

In Figure 3.4(b), profile D shows an ion plasma ($L_p \simeq 8$ cm and $N_{tot} \simeq 2{\times}10^8$) held in steady-state equilibrium with a $A_w = 1$ V, $f_s = 15$ kHz, $m_\theta = +2$ rotating wall drive. Profile E shows the same plasma after being moderately compressed and profile F shows the same plasma after being compressed by a factor of about 10 in central density n_0. The experimental conditions under which this data was measured will be described in more detail later.

Figure 3.5 shows the normalized rate of change of central density, $\dot{n}_0/n_0$, measured on a typical electron plasma (profile B of Figure 3.4(a)) as a function of drive frequency f_s. The central density of the plasma is measured as a function of time for a small amplitude ($A_w = 25$ mV), forwards-phased $m_\theta = 1$ rotating wall drive turned on at $t = 5$ seconds after inject. We obtain the initial compression rate due to the rotating wall by calculating $\dot{n}_0/n_0$ at $t = 5$ seconds. The entire process is then repeated at a different f_s. This small-amplitude drive creates very little heating, so $T \simeq 0.1$ eV. The measured background expansion rate of $\dot{n}_0/n_0 = -3 \times 10^{-3}\,\mathrm{s}^{-1}$ of this plasma has been subtracted from the data, so the plot indicates compression from the rotating wall alone.

The locations of the mode transmission peaks observed in this plasma are shown as down arrows, while the numerically calculated values for the corresponding

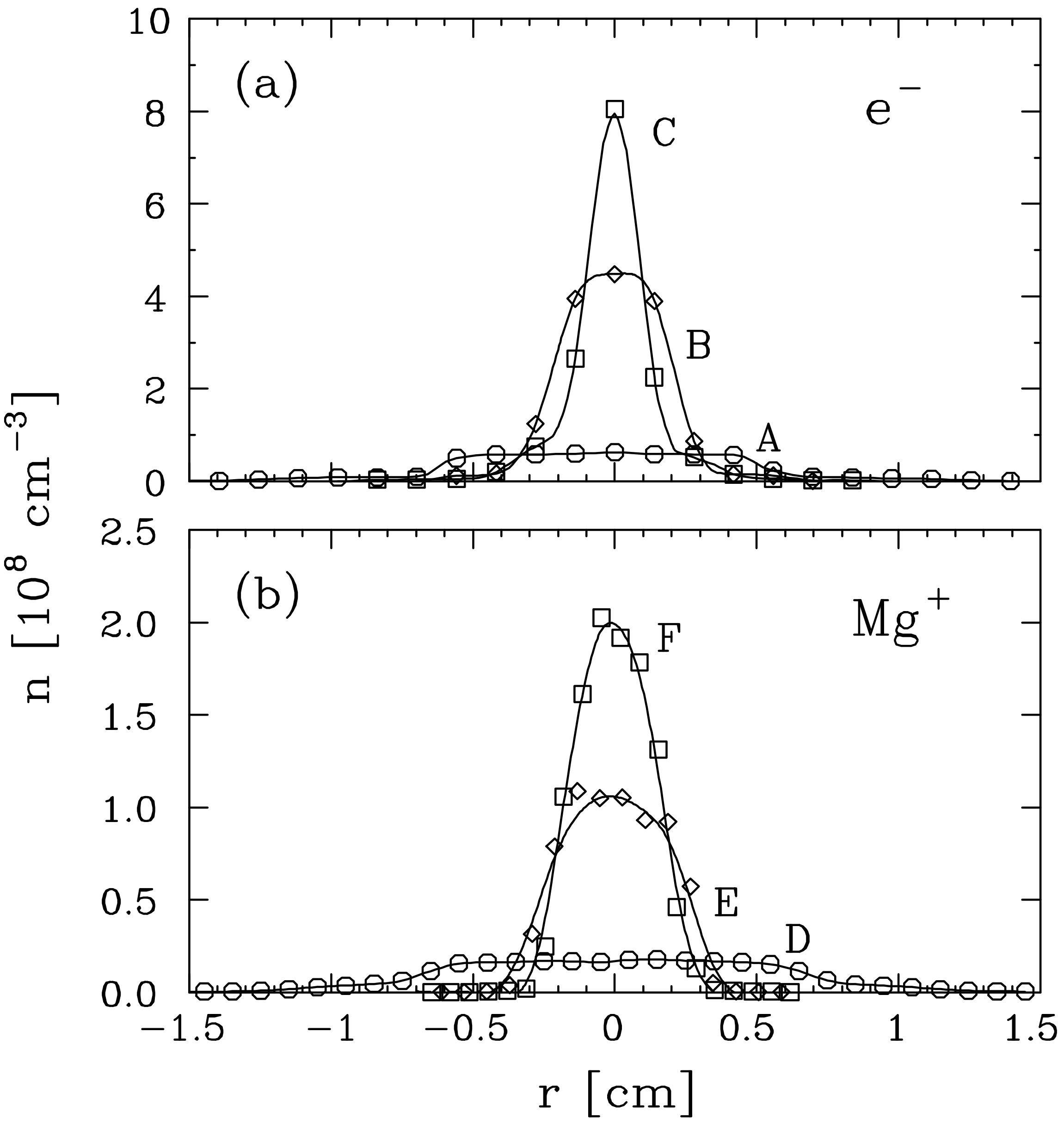

Figure 3.4: Measured radial density profiles for electron plasma (a) and ion plasma (b) showing rotating wall compression and expansion.

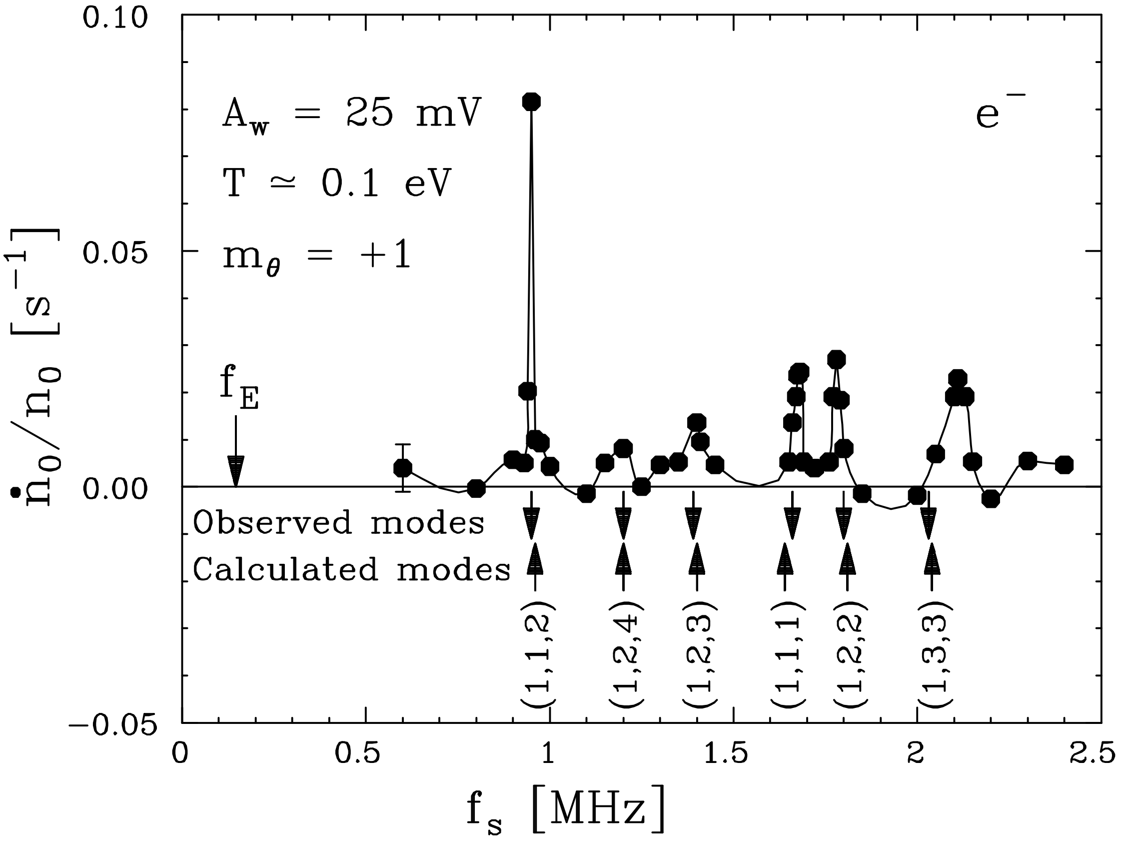

Figure 3.5: Measured central density compression rate, $\dot{n}_0/n_0$, of an electron plasma as a function of applied $m_\theta = 1$ perturbation frequency, f_s, for a small applied signal, $A_w = 25$ mV.

modes are shown with up arrows. It is apparent that good quantitative agreement is obtained between the predicted and observed mode frequencies for this plasma, and that plasma compression is associated with each of these modes.

We find that significant plasma compression and long-term confinement is only possible with larger-amplitude ($A_w \geq 0.2$ V) rotating wall drives. Figure 3.6(a) shows the same experiment as Figure 3.5, but with a large ($A_w = 0.4$ V) rotating wall drive. Figure 3.6(a) also includes data from reverse-phased ($m_\theta = -1$) application of the rotating wall drive, which we have displayed here as negative values of f_s. It is apparent that backwards-rotating modes cause enhanced expansion, while forwards-rotating modes cause plasma compression; this is consistent with basic thermodynamic arguments [12]. It can also be seen that increasing the amplitude

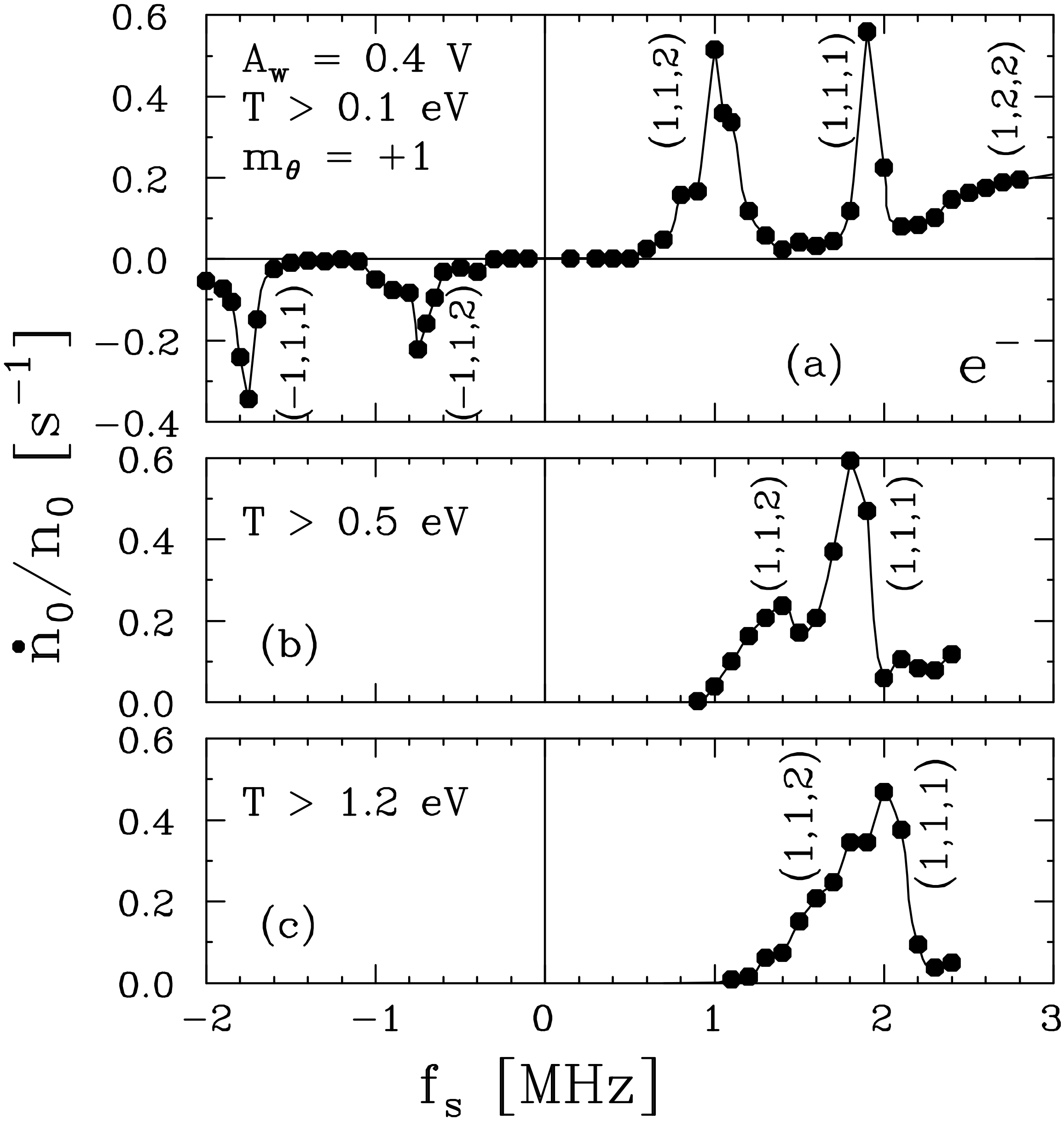

Figure 3.6: Measured central density compression rate $\dot{n}_0/n_0$ of an electron plasma as a function of applied $m_\theta = 1$ drive frequency f_s for plasmas at three different heating levels.

of the rotating wall drive has not only increased the magnitude of the torque on the plasma, but has also resulted in frequency shifts and broadening of the mode peaks. Corresponding broadening and shifts are observed in the transmission peaks at large amplitudes; i.e. the small amplitude peaks of Figure 3.1, for example, are observed to broaden and overlap at large A_w.

The correspondence between the observed torque peaks and the mode peaks observed in the transmission experiments was verified by repeating the experiment of Figure 3.6(a) with the plasma length changed from 35 to 17.5 cm. The length change moved the (1,1,2) transmission peak from 0.97 to 1.75 MHz; and the measured (1,1,2) torque peak followed, moving from 1.0 to 1.8 MHz. This shift is also reasonably consistent with the numerical solution, which predicts a change from 1.04 to 1.98 MHz.

This larger-amplitude drive causes significant plasma heating. On the peak of the (1,1,1) mode, for example, the rotating wall drive causes the plasma to heat at a rate of about 4 eV/s to a maximum temperature of about 2 eV; while on the peak of the (1,1,2) mode, the plasma heats at a rate of about 2 eV/s to a maximum temperature of about 1 eV. Far away from the resonance peaks, that is, around $f_s \simeq 0$, very little heating is observed, and T remains at about 0.1 eV. The upward shift of the mode frequencies seen in Figure 3.6(a) is believed to result primarily from this plasma heating; this is supported by numerical calculations and independent transmission measurements such as shown in Figure 3.3. Also, further upward shifts in the mode peaks can be observed if additional external heating is applied to the plasma.

In Figure 3.6(b), the experiment shown in Figure 3.6(a) is repeated, but with additional heating from an $A_w = .12$ V, $f_s = 0.8$ MHz, $m_\theta = 0$ drive on ring R10, which heats the plasma to about 0.5 eV in the absence of the rotating wall drive.

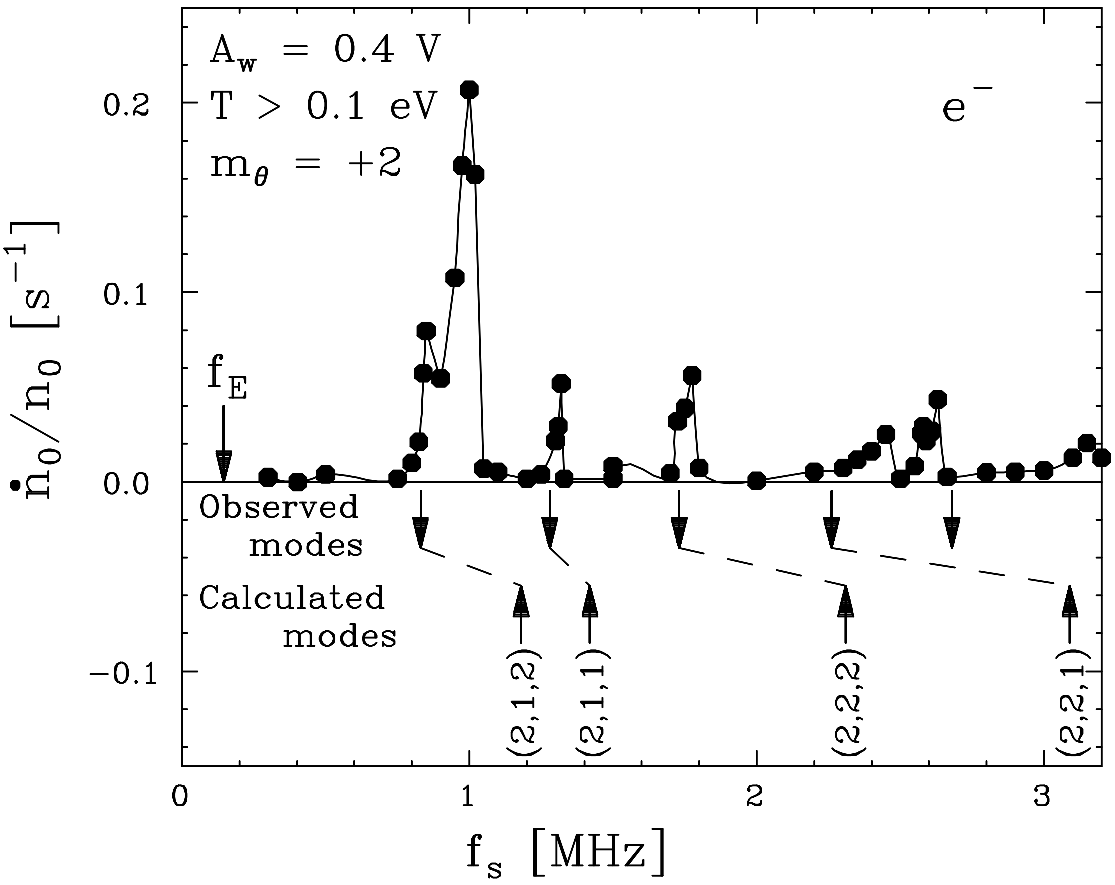

Figure 3.7: Measured central density compression rate, $\dot{n}_0/n_0$, for electron plasma as a function of applied $m_\theta = 2$ perturbation frequency, f_s.

The additional heating appears to cause further broadening of the modes. Also, the (1,1,2) torque peak is seen to move up significantly in frequency; presumably the (1,1,2) mode, because of its lower phase velocity, is more temperature sensitive than the (1,1,1) mode. In Figure 3.6(c), the $m_\theta = 0$ heating drive amplitude is increased to $A_w = .3$ V, giving a minimum plasma temperature of 1.2 eV. Here, it can be seen that the (1,1,2) mode peak has merged with the (1,1,1) peak, resulting in a single broad compression peak.

Driven $m_\theta = 2$ modes are also observed to torque on the plasma. The analog of Figure 3.6(a), but using a $m_\theta = 2$ drive, is shown in Figure 3.7. As for $m_\theta = 1$, all the modes observed in transmission also cause a measurable torque on the plasma. Here, down arrows denote modes observed in transmission experiments, while up

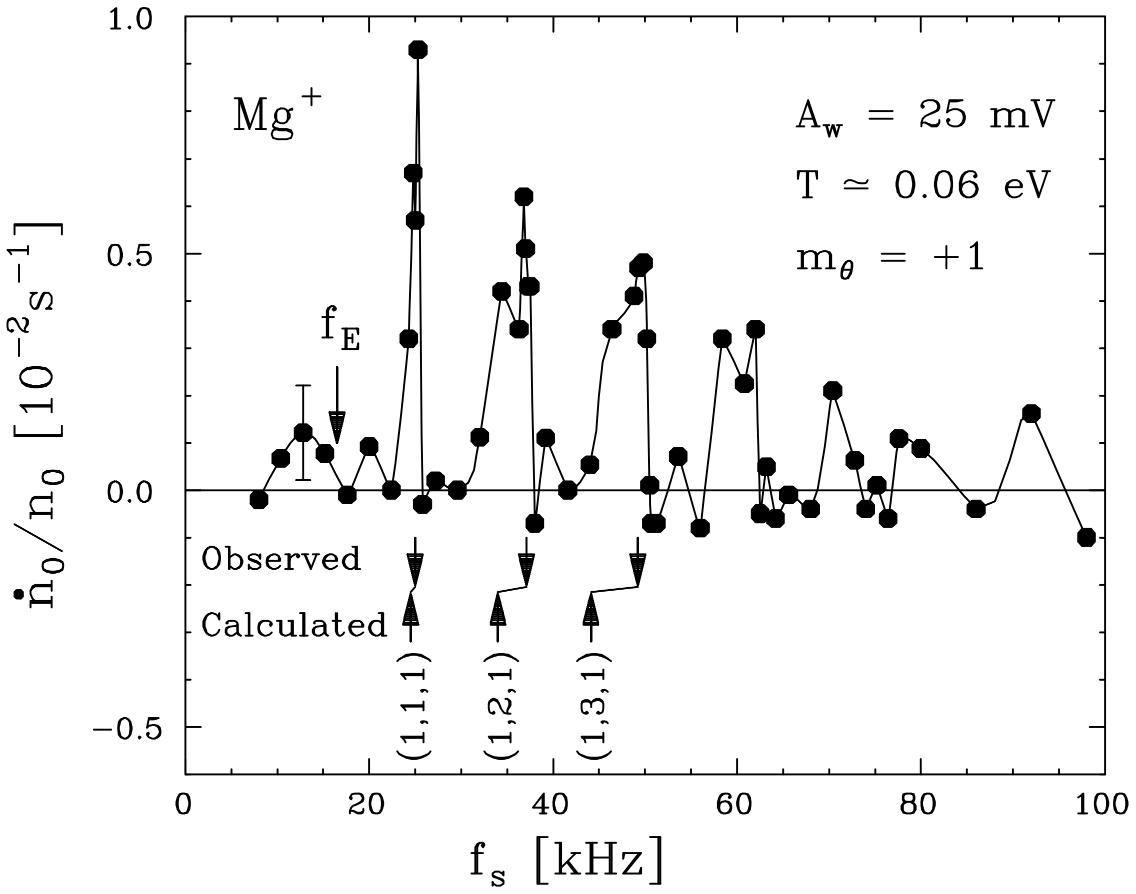

Figure 3.8: Measured central density compression rate, $\dot{n}_0/n_0$, for Mg$^+$ plasma as a function of applied $m_\theta = 1$ perturbation frequency, f_s, with small applied signal, $A_w = 25$ mV.

arrows represent the numerical mode frequency predictions; the numerical prediction tends to overestimate the observed $m_\theta = 2$ mode frequencies for this plasma. The negative peaks in $\dot{n}_0/n_0$ for $m_\theta = -2$ (not shown) were not observed as clearly as for $m_\theta = -1$, although a definite enhanced expansion rate was measured.

Comparison with Figure 3.6(a) shows that the torque due to the $m_\theta = 2$ modes is about half the magnitude of the torque due to $m_\theta = 1$ modes for the same amplitude drive; presumably, this is a consequence of the r^m dependence of the vacuum potentials. The heating rate resulting from driven $m_\theta = 2$ modes was also about half as large as observed for a $m_\theta = 1$ drive of the same amplitude.

As for electrons, azimuthally-dependent modes observed in ion plasma transmission experiments are also observed to cause a torque on the plasma. This is shown in Figure 3.8: here, a small amplitude (A_w = 25 mV) $m_\theta = +1$ rotating wall drive is applied to a Mg^+ plasma with $n_0 \simeq 4.6 \times 10^7\,\mathrm{cm}^{-3}$, $L_p \simeq 12.2$ cm, $R_p \simeq 0.41$ cm, and $T \simeq 0.06$ eV. We plot the measured compression rate $\dot{n}_0/n_0$ as a function of applied frequency f_s. The small measured background expansion rate, $\dot{n}_0/n_0 = 1.4 \times 10^{-3}\,\mathrm{s}^{-1}$, is subtracted from the measured compression rate so that the data represents the torque due to the rotating wall only. The $m_\theta = 1$ modes observed in transmission experiments for this plasma are shown as down arrows. It can be seen that, as for the electron plasmas, there is good agreement between the observed transmission peaks and the observed plasma compression peaks. The numerically calculated modes for this plasma are shown as up arrows. Here, the calculated modes are observed to be somewhat lower than the measured modes. Only very slight heating is observed due to this small-amplitude rotating perturbation: the temperature of the plasma is observed to reach a maximum of about 0.08 eV when driven on a resonance peak.

To obtain experimentally useful torques and long-term confinement of these ion plasmas, larger rotating wall amplitudes ($A_w \geq 0.2$ V) are necessary. Figure 3.9(a) shows an experiment similar to that of Figure 3.8, but using a large rotating wall signal amplitude ($A_w = 0.5$ V) and a higher-density plasma ($n_0 \simeq 10^8\,\mathrm{cm}^{-3}$). Here, we plot the measured total plasma compression $-\dot{\langle r^2\rangle}/\langle r^2\rangle$ as a function of applied rotating wall signal frequency f_s. The arrows indicate calculated mode frequencies for this plasma. The observed torque peaks are qualitatively consistent with torque coupling through driven electrostatic modes, but the individual modes are not well-resolved. Here, the higher axial wave numbers ($m_z \geq 4$) are probably not excited because the rotating wall ring S11 overlaps with about one-fourth of the

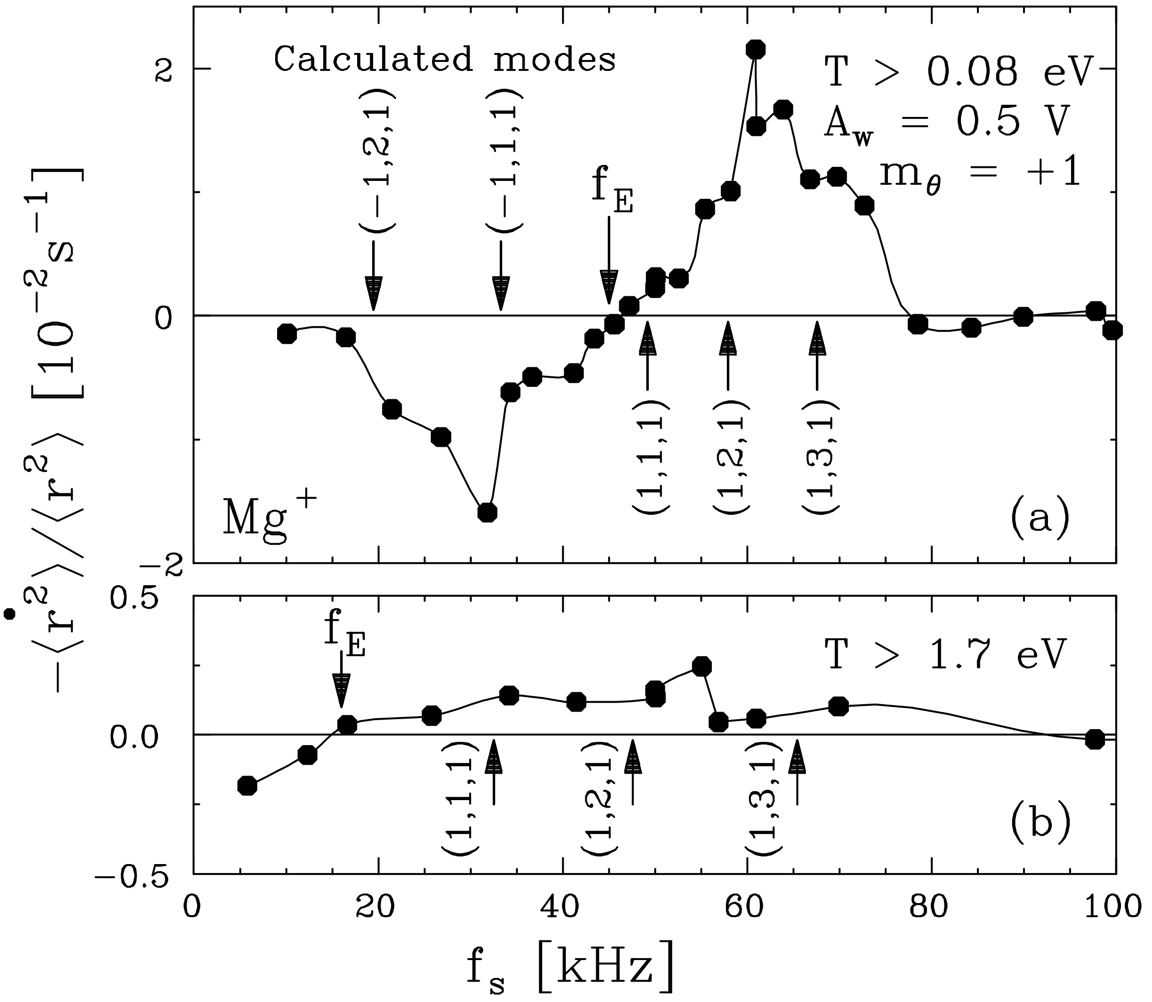

Figure 3.9: Measured total compression rate, $-\langle \dot{r^2}\rangle/\langle r^2\rangle$, as a function of $m_\theta = 1$ signal frequency f_s with large applied signal (A_w = 0.5 V) for two Mg$^+$ plasmas differing primarily in their temperature T.

length of the plasma.

Figure 3.9(b) shows compression data for an externally heated ion plasma ($T \simeq 1.7$ eV) with central density $n_0 \simeq 5.1 \times 10^7\,\mathrm{cm}^{-3}$. Again, the arrows indicate calculated mode frequencies for this plasma. It can be seen that the calculated mode locations are qualitatively consistent with the measured compression for this plasma, although apparently an extreme broadening of the torque peaks has taken place. Also, the magnitude of the torque obtained is about a factor of ten smaller than in Figure 3.9(b).

Together with the drop in the magnitude of the torque, the upward shift of the mode frequencies as the plasma is heated results in an increased "slip" between the drive frequency and the rotation frequency of plasma held in equilibrium by the rotating wall drive. For a given applied frequency f_s, hotter plasmas will tend to come to steady-state equilibrium, where the rotating wall torque balances the background drag, at a lower rotation frequency f_E, implying a larger slip frequency Δf defined by

$$\Delta f \equiv f_s/m_\theta - f_E \ . \tag{3.2}$$

For the equilibrium plasmas used in Figure 3.9, for example, the slip frequency is $\Delta f = 9$ kHz at $T = .08$ eV (Figure 3.9(a)) in contrast to a slip frequency $\Delta f = 32$ kHz at $T = 1.7$ eV (Figure 3.9(b)). This is qualitatively consistent with previous measurements (Figure 3 of Reference [28]), which found that the equilibrium slip frequency between an ion plasma and the rotating wall scaled approximately as the square root of plasma temperature, i.e. $\Delta f \propto \mathrm{T}^{1/2}$.

As can be seen from Figures 3.5 through 3.9, these plasma modes provide a large enhancement in the rotating wall torque. At the $(m_\theta, m_z, m_r) = (1,1,1)$ mode, for example, when driven with a drive amplitude of $A_w = 0.4$ V, a central density compression of $\dot{n}_0/n_0 \simeq 0.55\,\mathrm{s}^{-1}$ is observed for a typical electron plasma ($n_0 \simeq 4 \times 10^8\,\mathrm{cm}^{-3}$), and $\dot{n}_0/n_0 \simeq .08\,\mathrm{s}^{-1}$ is observed for a typical ion plasma ($n_0 \simeq 4 \times 10^7\,\mathrm{cm}^{-3}$). This is far larger in magnitude than the measured background expansion rate resulting from inherent trap asymmetries acting on these plasmas: $(\dot{n}_0/n_0)_{bkg} \simeq -3 \times 10^{-3}\,\mathrm{s}^{-1}$ for electrons and $(\dot{n}_0/n_0)_{bkg} \simeq -1.4 \times 10^{-3}\,\mathrm{s}^{-1}$ for ions.

Far from the observed mode frequencies, the applied field does not create an observable torque; the accuracy of this measurement is approximately $\dot{n}_0/n_0 \approx \pm 10^{-3}\,\mathrm{s}^{-1}$, so we estimate an on-resonance improvement in plasma compression of at least 500 for the electron plasma and at least 80 for the ion plasma.

We are only able to create a significant torque on long ion or electron plasma columns when driving z-dependent ($k_z \neq 0$), low frequency ($\omega \sim \omega_p$) electrostatic modes. We have not been able to measure a torque or achieve steady-state confinement in these plasmas with driven length-independent ($k_z = 0$) modes. Also, preliminary measurements show large heating (ion-cyclotron resonance heating) but no torque as a result of driving high-frequency ($\omega \sim \Omega_c$) electrostatic modes in a long Mg^+ plasma. This is inconsistent with experiments on small, laser-cooled spheroidal plasmas, which observe a large torque when driving $k_z = 0$, high-frequency ($\omega \sim \Omega_c$) electrostatic modes [41].

3.3.1 Density ramp using rotating wall

A ramped-frequency rotating wall drive can create a smooth increase of the plasma density, as illustrated in Figure 3.10. Here, the squares show measured central density and temperature of a typical electron plasma as a function of the drive frequency f_s for a slow ramp of a $m_\theta = +1$, $A_w = 0.4$ V rotating wall drive. f_s is ramped linearly from 0.5 to 2.13 MHz in 1000 seconds, starting from the injected profile B of Figure 3.4(a). In the range $0.5 < f_s < 0.7$ MHz, there is no torque on the plasma, and the plasma expands slowly. In the range $0.7 < f_s < 1.4$ MHz, the plasma is being slowly compressed by the (1,1,2) mode. At each frequency, the plasma can be thought of as being in an equilibrium state where the mode torque is balancing the background drag on the plasma, i.e. $(\dot{n}_0/n_0)_{rw} + (\dot{n}_0/n_0)_{bck} = 0$. At each of these equilibrium points, the ramp in f_s can be stopped and the plasma held in steady-state confinement. The heating resulting from the increasing applied torque causes the mode to shift upwards in frequency, as was demonstrated Figure 3.6, so there is a relatively smooth transition to the region $1.4 < f_s < 2$ MHz, where the plasma is being compressed by the both the (1,1,2) mode and the (1,1,1) mode. For $f_s > 2$ MHz, the rotating wall torque is not sufficiently strong to balance the

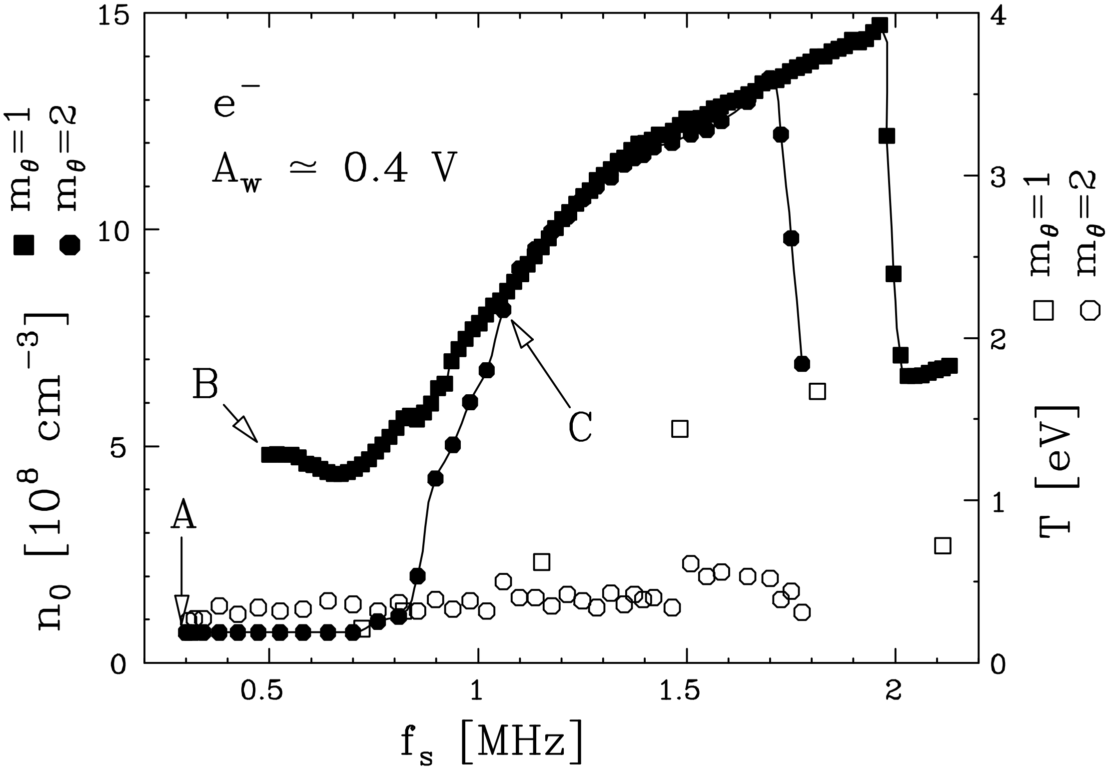

Figure 3.10: Electron plasma compression using rotating wall frequency ramp.

background drag and the density rapidly decreases a factor of two until a different equilibrium is reached; presumably the plasma is experiencing a torque from the (1,2,2) mode at this point.

A similar electron plasma experiment but using a $m_\theta = +2$ drive is shown by the circles in Figure 3.10. Here, the drive frequency ramp was begun from an initially expanded plasma, corresponding to profile A of Figure 3.4(a); this was done to illustrate a density compression of a factor of 20. This expanded plasma was obtained from the injected profile B by applying a $m_\theta = -2$ perturbation at 1 MHz for 50 seconds. A $m_\theta = +2$ drive was then ramped from 0.3 to 1.8 MHz in 415 seconds.

No compression is observed for the beginning of the frequency ramp ($0.3 < f_s < 0.8$ MHz), but compression occurs when the rotating wall ramp approaches

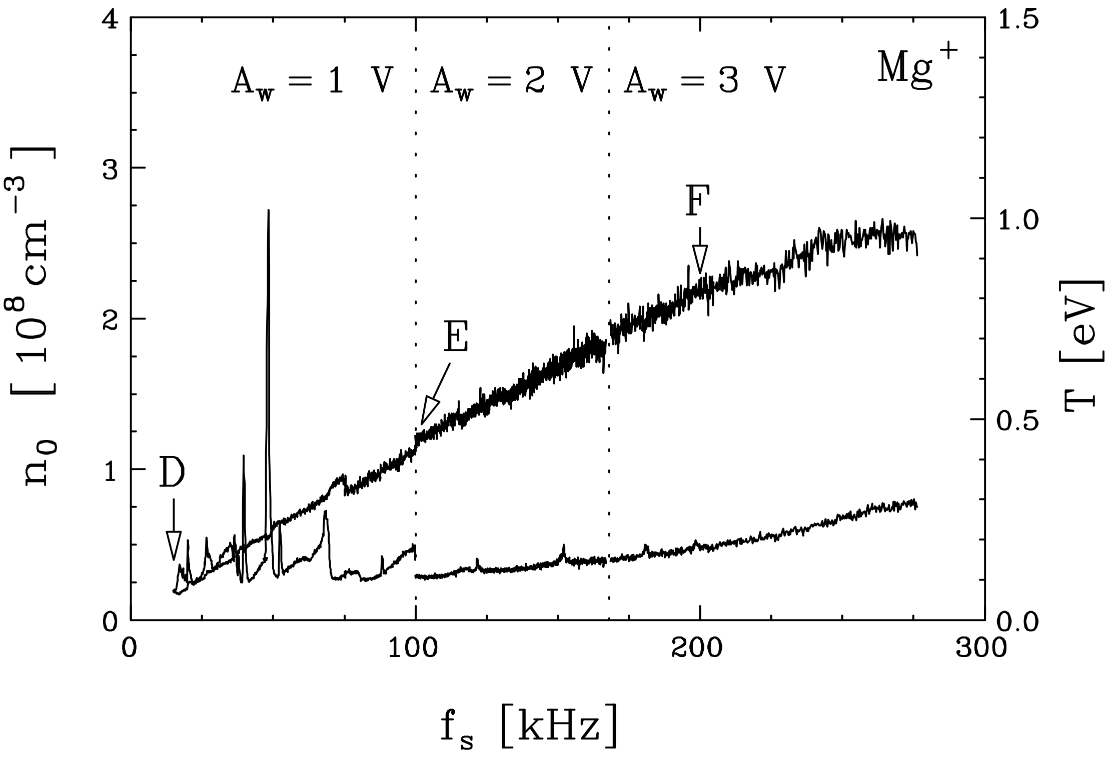

Figure 3.11: Ion plasma compression using $m_\theta = +2$ rotating wall frequency ramp.

the frequency of the (2,1,2) mode ($f_s \approx 0.8$ MHz). Profile C of Figure 3.4(a) was measured after ramping to $f_s = 1.05$ MHz. As in the $m_\theta = +1$ ramp, a fairly smooth density compression is obtained. This smooth density compression despite the distinct torque peaks observed in Figure 3.7 is a result of the torque peaks widening, shifting upward, and merging together, as seen for the $m_\theta = +1$ drive in Figure 3.6.

A ramp of ion plasma density is shown in Figure 3.11. Here, we plot central density n_0 and temperature T measured during a slow upward frequency ramp of a $m_\theta = +2$ rotating wall perturbation. A short ion plasma was used here ($L_p \simeq 8$ cm). The ramp begins with a typical ion plasma (profile D of Figure 3.4(b)) held with applied frequency $f_s = 15$ kHz. The frequency f_s is then increased from 15 to 280 kHz at a rate of about 20 seconds per kHz, and the rotating wall amplitude is increased from $A_w = 1$ to 2 to 3 V during the frequency ramp to maintain plasma compression. The spikes in the temperature at lower f_s are identified as resulting from $m_\theta = 0$ modes launched by small imbalances in the rotating wall drive. Profiles E and F of Figure 3.4(b) are taken at $f_s = 100$ and 200 kHz, respectively, of this ramp.

This ramp of f_s is sufficiently slow that each point on the curve indicates an equilibrium state where the rotating wall torque is balanced by the background torque, so the ramp can be stopped and the plasma held in steady-state at any point. This technique has been used to hold ion plasmas in a desired steady-state equilibrium for periods of up to two weeks. Similar results to Figure 3.11 are obtained using a $m_\theta = +1$ rotating wall on ion plasmas.

For both electron and ion plasmas, we find a maximum density n_0 to which a given plasma can be compressed. This result seems to indicate that the rotating wall torque increases more weakly with increasing density n_0 than does the background drag. Measurements on electron plasmas are consistent with this model: we find a rotating wall compression rate which decreases slightly as n_0 is increased; the background expansion rate, however, is found to increase strongly with n_0, scaling as $(\dot{n}_0/n_0)_{bck} \propto n_0^2$. In the ion plasmas discussed here, however, no clear density dependence was observed in mode-driven compression or in the background drag. It is possible that the plasma heating associated with the rotating wall compression is important in limiting the maximum compression of ion plasmas: measurements such as Figure 3.9 indicate a decrease in mode-driven torque with increasing temperature in ion plasmas, while no clear temperature dependence of the background drag is found. Measurements of the background drag in these plasmas are presented in Section 3.5. Normally, we attain central density compression of up to about 20% of the Brillouin limit, n_B, in ion plasmas; with the application of laser cooling, $n_0 \simeq .25\, n_B$ was achieved.

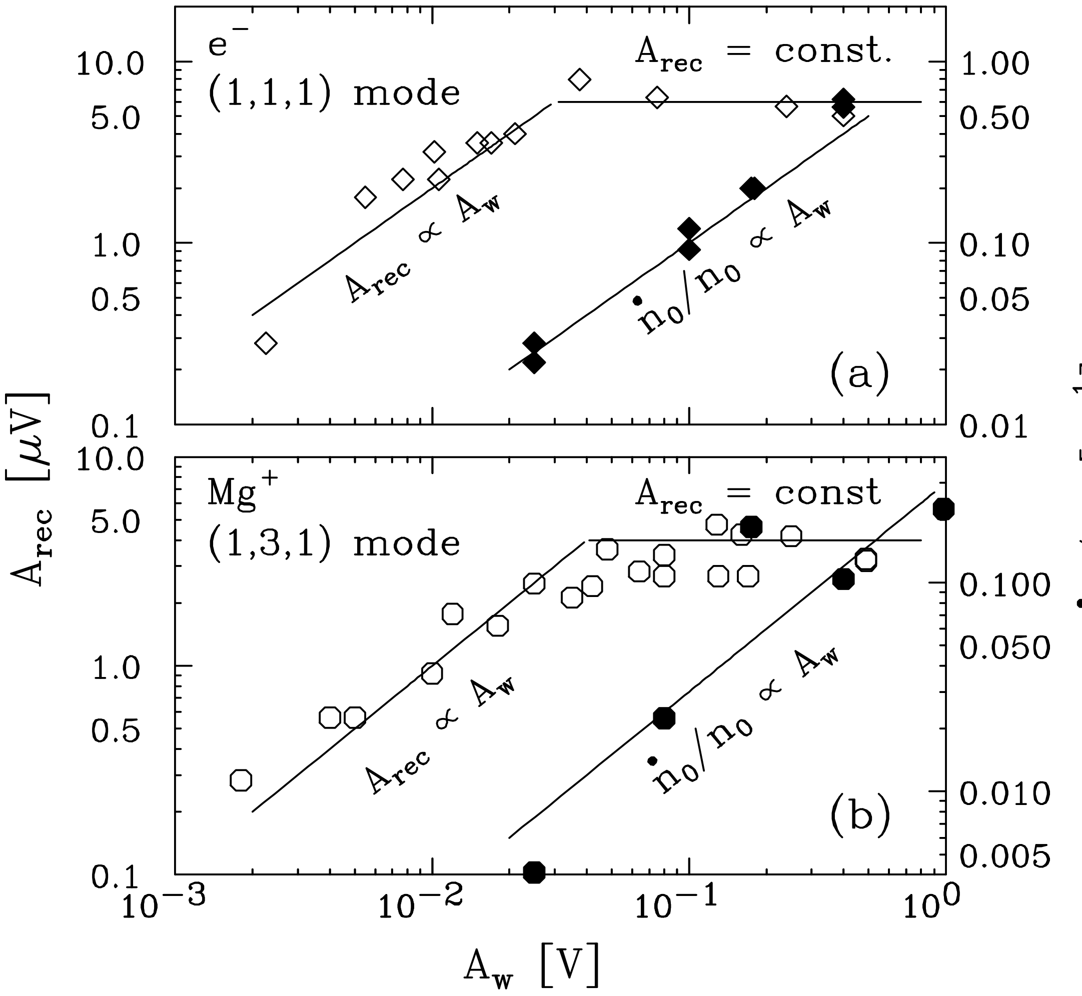

Figure 3.12: Peak density compression rate $\dot{n}_0/n_0$ and amplitude of signal received in mode transmission A_{rec} as a function of drive amplitude A_w for electron plasma (a) and ion plasma (b).

3.3.2 Mode torque scaling with drive amplitude

The mode-driven compression rate scales as the drive amplitude A_w, as opposed to the A_w^2 that might be expected from linear perturbation theory. This is shown in Figure 3.12, where we plot the measured compression rate as a function of drive amplitude when the rotating wall drive is applied on a mode peak. The scaling of the rotating wall compression due to the (1,1,1) mode in a typical electron plasma (profile B of Figure 3.4) is shown in Figure 3.12(a). Here, the solid diamonds indicate measured compression $\dot{n}_0/n_0$ as a function of the applied $m_\theta = 1$ drive amplitude

A_w. The drive frequency f_s is tuned to the peak of the mode, $f_s \simeq 1.6$ MHz. It can be seen that the measured compression rate is approximately linear in applied signal, i.e. $\dot{n}_0/n_0 \propto A_w$. For comparison, the amplitude of the signal received in transmission experiments under the same experimental conditions is shown as hollow diamonds. The received signal is roughly proportional to the drive amplitude, then saturates in the region of interest ($A_w > 0.03\,\mathrm{V}$).

A similar amplitude dependence is found to occur in ion plasmas, as shown in Figure 3.12(b). Here, we plot the measured compression rate at the peak of the (1,3,1) mode as a function of the drive amplitude. It can be seen that the measured compression rate (solid circles) is roughly linear in A_w; the received signal, however, is linear in A_w at low drive amplitudes ($A_w < 0.03$ V), but constant at higher drive amplitudes.

The results of Figure 3.12 suggest that at low drive amplitudes ($A_w \lesssim 0.02$ V), the mode compression would be linear, corresponding to a mode amplitude which rises linearly with applied amplitude and a mode torque which is (presumably) proportional to the applied amplitude squared (i.e. $\dot{n}_0/n_0 \propto A_w^2$). At higher drive amplitudes ($A_w \gtrsim 0.02$ V), the mode becomes saturated, and the mode amplitude no longer increases with drive amplitude; this results in a mode compression which is linear with applied amplitude.

The mechanism for this mode saturation is not understood at present. It is possible that the mode saturation occurs because the fractional perturbed density is reaching order unity, i.e. $|\delta n/n| \approx 1$. However, estimates of the mode amplitude corresponding to maximum received signal, $A_{rec} \simeq 5\ \mu V$ for the plasmas of Figure 3.12 give $|\delta n/n| \approx 0.01$ to 0.10; this calculation is complicated by the fact that the mode shape at the end of the plasma is not well known. In ion plasmas, the mode amplitude can also be estimated from the magnitude of the component of the

LIF signal which oscillates coherently with the mode; these measurements give an estimated fractional density perturbation $|\delta n/n| \approx 0.01$. Thus, these preliminary estimates indicate that the fractional perturbed density of the saturated modes is much smaller than unity; i.e. $|\delta n/n| \ll 1$.

Another possible explanation for the observed mode saturation is that the mode has become nonlinearly Landau damped, resulting in a parallel distribution function has become strongly perturbed in the region of the wave phase velocity. Careful observation of the parallel distribution function of ion plasmas with the LIF diagnostic, however, has not revealed any measurable deviation from a parallel Maxwellian for the range of plasma temperatures relevant to this paper. It is possible that low density plasma at large radii, outside the bulk of the plasma and below the noise level of the LIF diagnostic, plays an important role in the mode damping. Also, finite-length effects might be significant in determining the mode damping in these trapped plasmas.

3.4 Measurements of Plasma Mode Damping

In this section, we observe that the plasma mode damping in these plasmas is not described by simple linear Landau damping. We present measurements of the damping rate of the $(m_\theta, m_z, m_r) = (1,3,1)$ mode in a typical ion plasma ($n_0 \simeq 3 \times 10^7\ \mathrm{cm}^{-3}$, $L_p \simeq 12$ cm). The damping rate was obtained by driving the mode on resonance with a $m_\theta = +1$ drive for about 0.2 seconds; the received signal was observed to increase then level off to a constant amplitude within 10 ms. The drive was then turned off and the rate at which the received signal A_{rec} decreased was fit to an exponential decay with rate γ, i.e. $A_{rec}(t) = A_{rec}(0)\mathrm{e}^{-\gamma t}$.

In Figure 3.13, we plot the measured mode quality $Q \equiv \omega/2\gamma$ as a function of temperature T, where $\omega \simeq 2\pi(60\mathrm{kHz})$. In this experiment, the plasma temperature

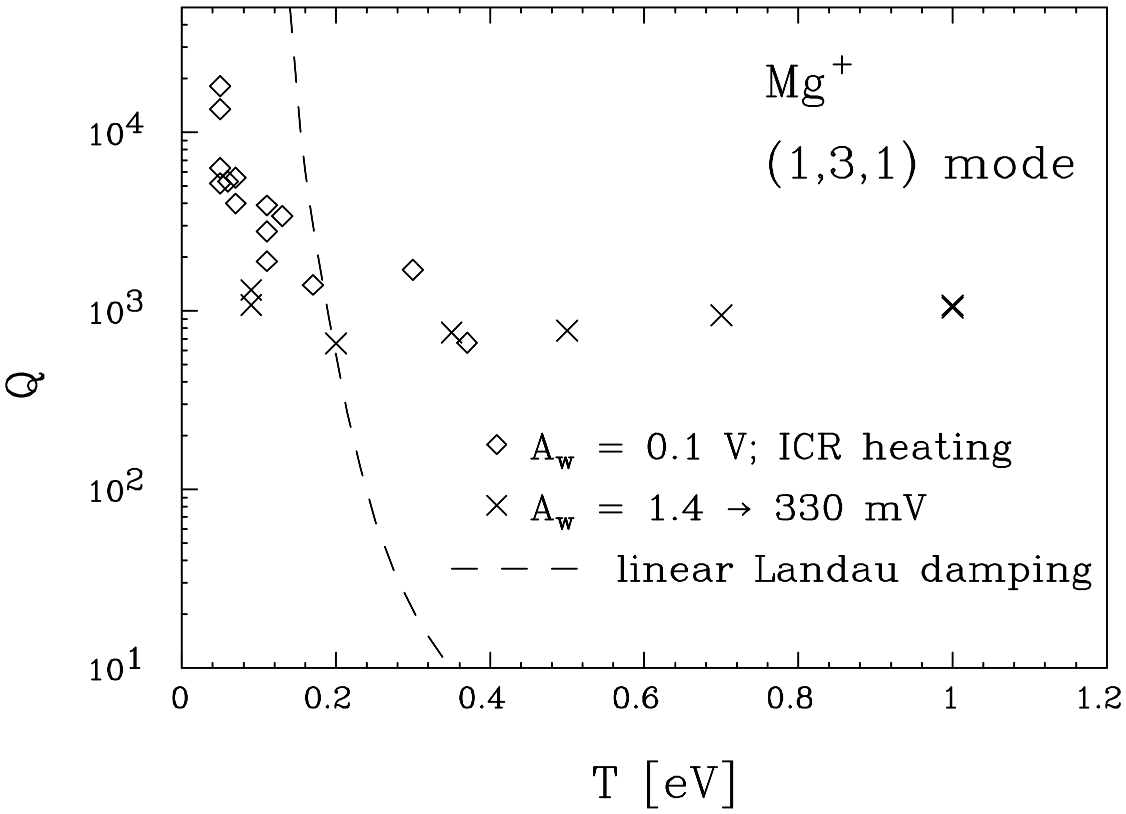

Figure 3.13: (1,3,1) mode damping vs. temperature.
Measured damping of (1,3,1) mode in Mg$^+$ plasma as a function of temperature.

was varied in two fashions: either by varying the amplitude of the mode drive A_w, or by fixing A_w and applying varying levels of ion-cyclotron resonance heating (ICRH). In the first method, the amplitude of the $m_\theta = 1$ drive was varied from $A_w = 1.4$ to 335 mV to provide plasma temperatures ranging from $T = 0.05$ to 0.4 eV. In the second method, the amplitude of the drive was fixed at $A_w = 100$ mV and a signal at the ion cyclotron frequency Ω_c was applied to one sector on S11. The amplitude of the cyclotron-frequency signal was varied from $A_{ICRH} = 0$ to 130 mV, giving equilibrium temperatures ranging from .08 eV to 1.0 eV.

These measurements are relevant because predicting the torque resulting from a driven mode requires an understanding of the mode damping rate. For comparison to the data, the estimate of linear Landau damping (Equation B.6) for this mode is plotted. It is apparent that the observed mode damping is not described by the simple linear Landau damping model. This disagreement is especially surprising for $T \gtrsim 0.4$ eV, where Landau damping is predicted to become extremely strong for this mode.

The results suggest that linear Landau damping theory cannot be applied to these trapped particle distributions, where driven waves can cause arbitrarily large variations in the particle distribution function. Preliminary damping experiments done on the (1,1,1) and (1,1,2) modes in a typical electron plasma find a mode quality $Q \simeq 2 \times 10^3$ to 6×10^3, which is similar in magnitude to the values shown here.

3.5 Measurements of Inherent Asymmetry Transport in the IV Apparatus

In this section, we present measurements of the inherent asymmetry-induced transport rate in the IV apparatus for electrons and ions. The plasmas discussed in this thesis are typically observed to have an inherent background transport which causes them to expand radially on a time scale of $\tau_m \simeq 100$ to 1000 seconds, where τ_m is defined as the time required for the plasma central density to decrease by a factor of two. This expansion is believed to occur as a result of small static magnetic and electric field errors. These field errors break the azimuthal symmetry of the confinement geometry, and can thus drag on the spinning plasma column, resulting in spin-down and radial plasma expansion.

Extensive measurements of the inherent asymmetry transport rate have been made for electron plasmas in other Penning-Malmberg traps. In general, these measurements find that the plasmas expand radially at a rate $\tau_m^{-1} \propto (L_p/B)^2$ [16]. Thus, shorter plasmas with stronger magnetic fields are better confined than longer

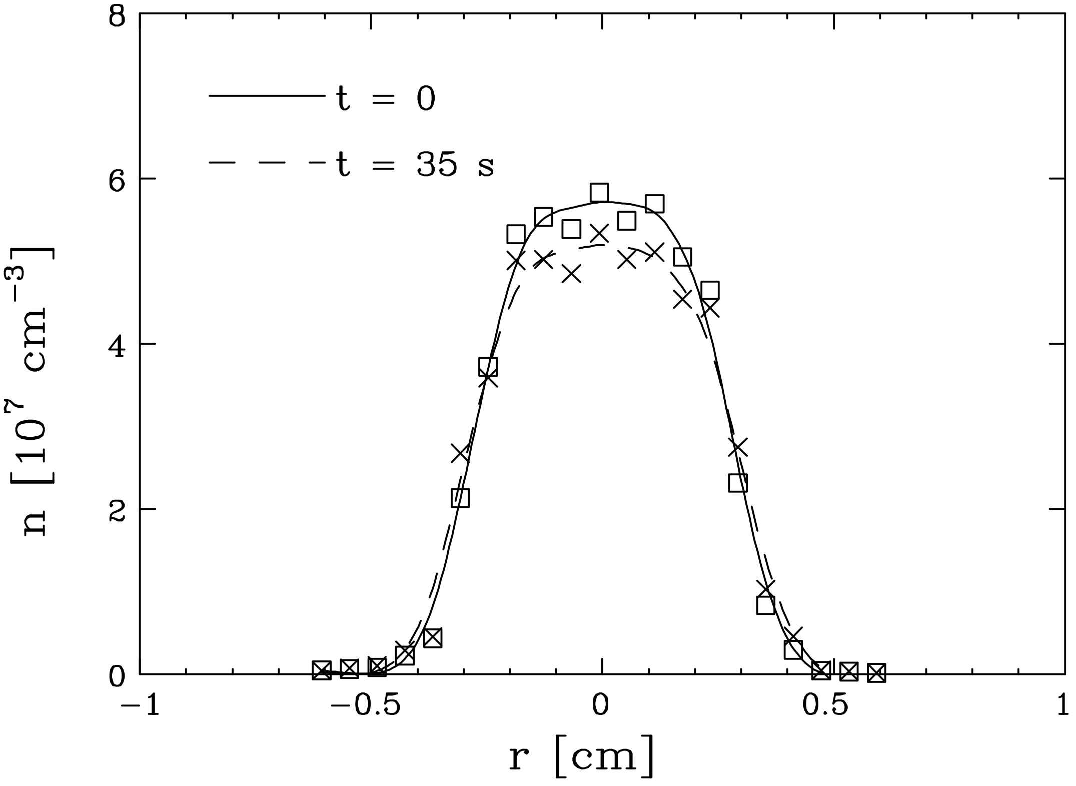

Figure 3.14: Measured free expansion of an ion cloud demonstrating radial transport resulting from inherent trap asymmetries.

plasmas with weaker magnetic fields. A more general scaling consistent with many measurements is $\tau_m^{-1} \propto \mathcal{R}^{-2} \propto n_0^2 L_p^2 / B^2 T$ where $\mathcal{R}$ is the central plasma “rigidity” $\mathcal{R} \equiv f_b(r=0)/f_E(r=0)$ [36].

A typical radial expansion measurement is shown in Figure 3.14. Here, an ion plasma is initially held in the steady-state radial density profile labeled $t = 0$ with a $f_s = 20$ kHz, $A_w = 0.5$ V, $m_\theta = +1$ rotating wall. At time $t = 0$, the rotating wall field is turned off, and the plasma begins to expand radially. The density and temperature are measured every 5 seconds with the LIF diagnostic; here, we show $t = 0$ and $t = 35$ seconds.

The rate of change of central density of freely expanding electron plasmas was measured at magnetic field $B = 4$ T, temperature $T \simeq 0.2$ eV, and central densities

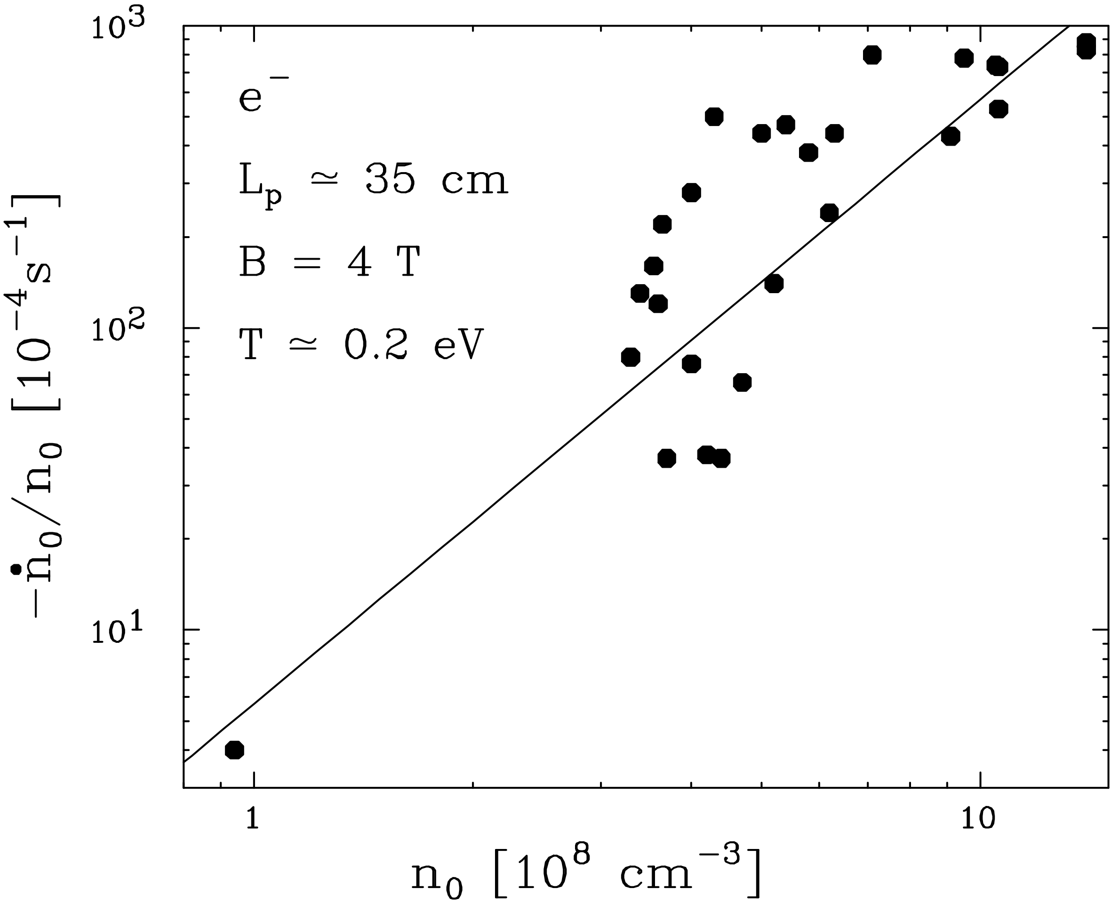

Figure 3.15: Measured background expansion rate $-\dot{n}_0/n_0$ of electron plasmas as a function of central density n_0 showing $-\dot{n}_0/n_0 \propto n_0^2$ scaling.

$n_0 \simeq 10^8$ to $10^9\,\mathrm{cm}^{-3}$. In Figure 3.15, the measured expansion rate $-\dot{n}_0/n_0 \equiv \tau_{bck}^{-1}$ is plotted as a function of central density n_0. The straight line is $\tau_{bck}^{-1} = (5.7 \times 10^{-6}\,\mathrm{s}^{-1})(n/10^7\,\mathrm{cm}^{-3})^2$, which is seen to provide a good fit to the measured expansion rate.

Background radial expansion measurements were performed on ion plasmas at magnetic field $B = 4$ T, length $L_p \simeq 12$ cm, and background pressure $P_N \simeq 4 \times 10^{-9}$ Torr. On average, we observe no clear temperature or density dependence in the measured total expansion rate $\tau_{\langle r^2 \rangle}^{-1} \equiv \langle \dot{r^2} \rangle / \langle r^2 \rangle$.

In Figure 3.16, the measured ion expansion rate $\tau_{\langle r^2 \rangle}^{-1}$ is displayed as a function of temperature T for ion plasmas with central densities in the range $6 \times 10^7 < n <$

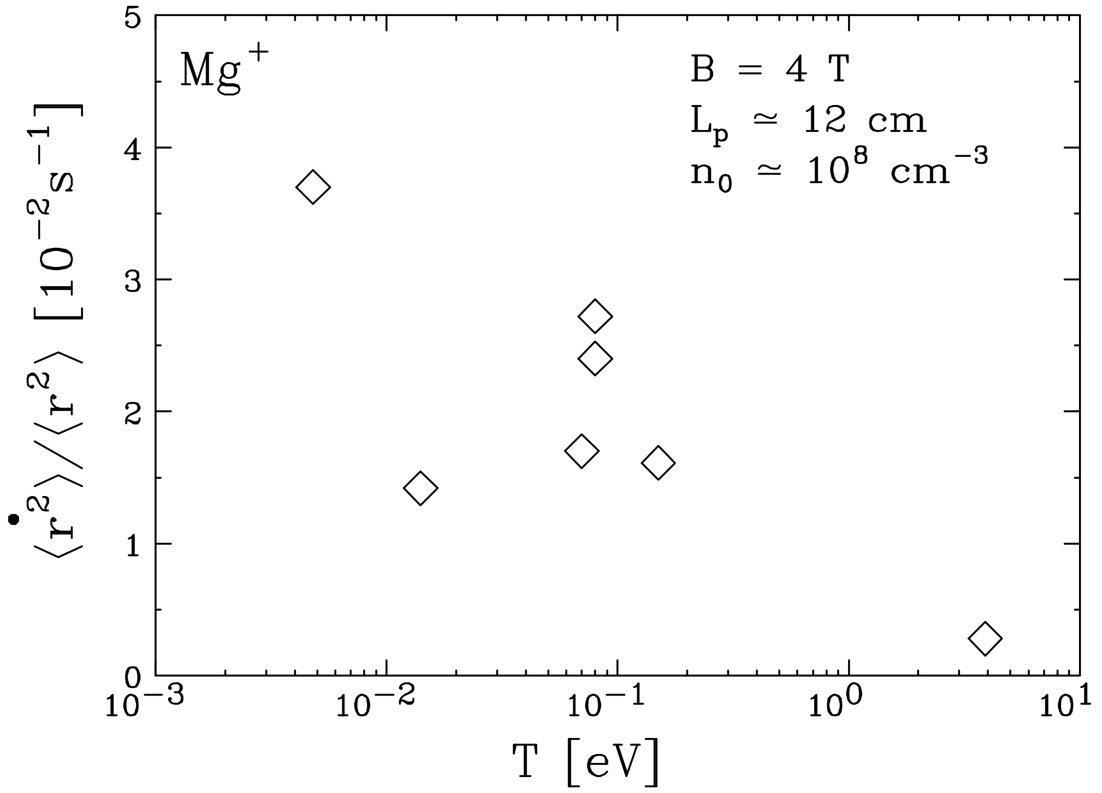

Figure 3.16: Measured free expansion rate of $\langle \dot{r^2} \rangle / \langle r^2 \rangle$ of ion plasmas as a function of temperature T, showing relatively weak temperature dependence.

$1.4 \times 10^8\,\mathrm{cm}^{-3}$. The plasmas for this data have mean radii in the range $0.3 < R_p < 0.4$ cm, except for the highest temperature point ($T = 3.9$ eV), which has $R_p \simeq 0.9$ cm. The temperature range covered by the data is $5 \times 10^{-3} < T < 4$ eV; despite this large (three orders of magnitude) variation in the temperature, only a factor of ten variation is seen in the measured expansion rate; we thus conclude that there is no strong temperature dependence to the expansion rate of ion plasmas under these conditions.

In Figure 3.17, the measured expansion rate $\tau^{-1}_{\langle r^2 \rangle}$ is displayed as a function of central density n_0 over a range $10^7 < n < 13.8 \times 10^7\,\mathrm{cm}^{-3}$. These plasmas have mean radii in the range $0.3 < R_p < 0.5$ cm and temperatures $0.1 < T < 1.9$ eV. It can be seen that the expansion rate does not display a significant trend in central

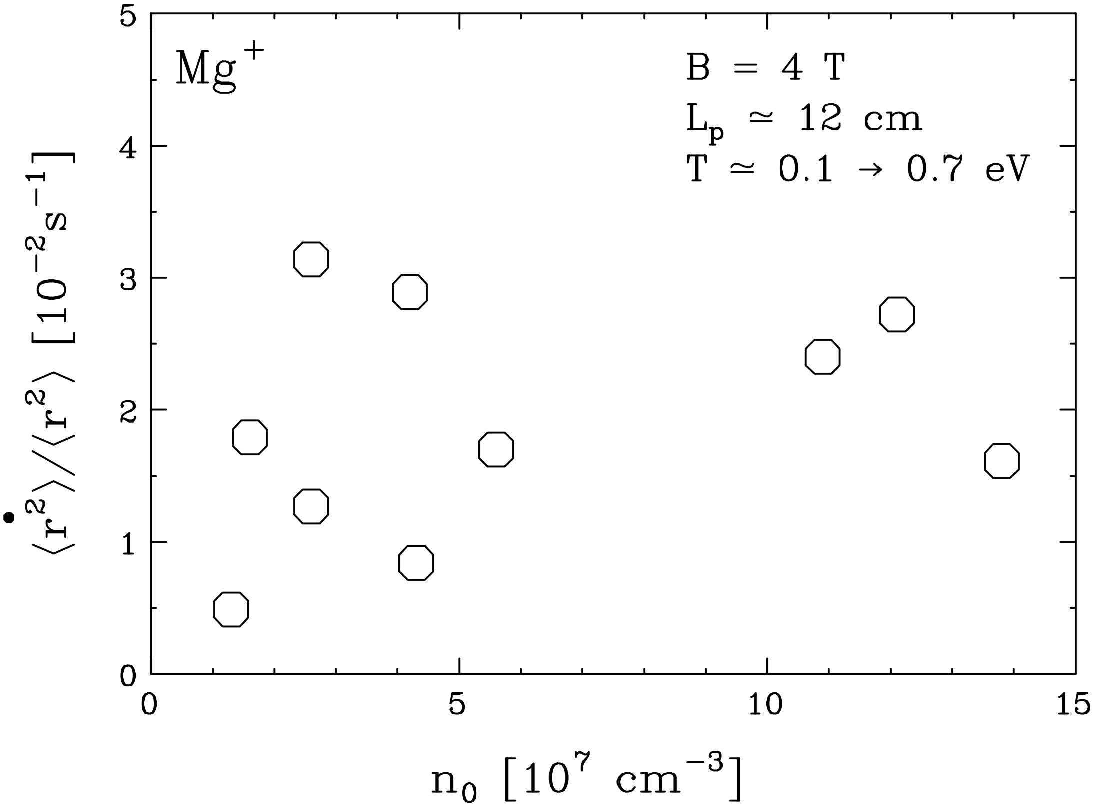

Figure 3.17: Measured free expansion rate of $\langle \dot{r^2} \rangle / \langle r^2 \rangle$ of ion plasmas as a function of central density n_0, showing no clear density dependence.

density.

A summary of current data on the background expansion rate of plasmas in these traps is shown in Figure 3.18. Here, we plot the measured background expansion rate as a function of the plasma rigidity R. The expansion rate is scaled by $M^{1/2}$ where $M \equiv m/m_e$ is the particle-to-electron mass ratio; this scales out the anticipated $M^{1/2}$ scaling for transport time scales in these plasmas [15].

The dashed line and solid line correspond to a fit to background expansion data from two different Penning-Malmberg experiments, "V$'$ " and "EV" [16]. The ranges of the lines indicate the range of the data from the experiments; over this range, the data is well-fit by the scaling $\tau_m^{-1} \propto R^{-2}$. For the V$'$ and EV data, the variation in R was accomplished by varying magnetic field B and plasma length L_p,

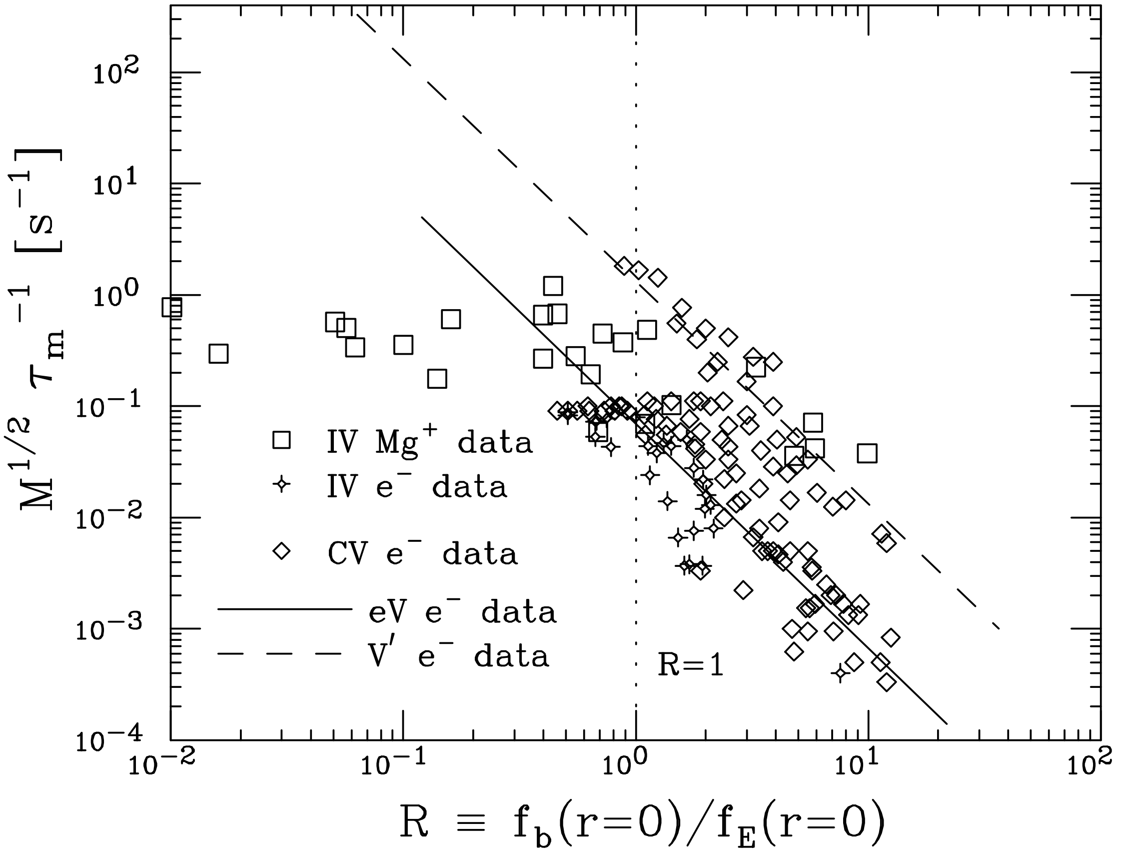

Figure 3.18: Measurements of free expansion rate τ_m^{-1} resulting from inherent trap asymmetries as a function of plasma rigidity R.

so this data indicates a background expansion rate $\tau_m^{-1} \propto (L_p/B)^2$.

The diamonds correspond to measured expansion rates τ_m^{-1} measured on electron plasmas in a third Penning-Malmberg trap, "CV". For the CV data, the variation in R was accomplished by varying magnetic field B, temperature T, and density n_0. The data can be seen to be in rough agreement with a $\tau_m^{-1} \propto R^{-2}$ scaling, although there is some indication that this scaling is not obeyed for data with $R < 1$.

The stars in Figure 3.18 correspond to the IV machine electron data of Figure 3.15; here we plot the expansion rate $\tau_{bck}^{-1} \simeq \tau_m^{-1}$ as a function of R. The squares in Figure 3.18 correspond to Mg$^+$ ion data from the IV machine; here we plot the scaled expansion rate $M^{1/2}\tau_{\langle r^2\rangle}^{-1}$ as a function of R, where $M^{1/2} = 210$ and $\tau_{\langle r^2\rangle}^{-1} \simeq \tau_m^{-1}$. For this data, the variation in R is achieved by varying the central density over the range $10^7 < n_0 < 10^8$ cm^{-3} and the temperature over the range $10^{-3} < T < 2$ eV at $B = 4$ T and $L_p \simeq 12$ cm.

For ions, we find no clear temperature or density scaling in the measured $\tau^{-1}_{\langle r^2 \rangle}$; this contradicts the $\tau_m^{-1} \propto R^{-2}$ scaling indicated in the other experiments. A possible reason for this discrepancy is the collisionality of the plasmas: the electron experiments shown in Figure 3.18 tend to have electron-electron collision frequencies which are low compared with the thermal bounce frequency, $\nu_{ee}/f_b < 1$; much of the ion data, however, is in the opposite regime, i.e. $\nu_{ii}/f_b > 1$.

Chapter 4

Measurement of Collisional Heat Transport

4.1 Collisional Transport Background

Chapters 4 and 5 of this thesis discuss collisional transport measurements in pure ion plasmas. Transport in plasmas can be broadly categorized as collisional or turbulent. Collisional transport is driven by fluctuating fields from the thermal motion of individual particles; whereas turbulent transport is driven by non-thermal fluctuations such as unstable collective modes, and can therefore be much larger than collisional transport. In neutral plasma experiments, transport is often turbulent in nature because of the many instabilities which can lead to turbulence. Nonneutral plasmas, on the other hand, are relatively stable, and can be confined in a quiescent near-thermal equilibrium state. This allows collisional transport to be observed without being masked by turbulent transport.

In collisional transport, collisions can be categorized as binary (two-particle) or wave-mediated collisions. In a binary collision, two particles interact directly through their mutual electric field, resulting in an exchange of energy. In a plasma, these direct binary collisions can occur over distances up to the Debye shielding length $\lambda_D \equiv \sqrt{T/4\pi n e^2}$. In a wave-mediated collision, a particle's thermal motion excites a plasma wave (or phonon) which is absorbed by a particle at a different location. This allows a transfer of energy and angular momentum over distances up to the plasma dimensions, provided that the wave is not strongly damped. For heat transport, for example, wave-mediated collisions are believed to be important in sufficiently large plasmas (with thermal gradient scale length $L_T > 100\,\lambda_D$) and in strongly-correlated plasmas.

The nature of binary collisions between particles depends on the impact parameter ρ compared with the cyclotron radius r_c. Classical transport theory analyzes collisions with $\rho \leq r_c$, which cause a scattering between the perpendicular and parallel velocities of the particles. These "short-range" collisions, which occur in all plasmas, cause thermalization of the parallel and perpendicular velocity distributions. They also cause a random cross-field step of the particle guiding centers by a distance of order r_c, resulting in cross-field diffusion of particles, momentum, and heat.

In a plasma with $\lambda_D > r_c$, particles can also interact via "long-range" collisions with impact parameters $r_c < \rho < \lambda_D$. In a long-range collision, a particle traveling along one magnetic field line interacts with a particle on a different field line separated by a distance ρ. These collisions can result in an exchange of parallel velocities, which gives rise to a heat flux in the presence of a temperature gradient. Also, the particles can $\mathbf{E} \times \mathbf{B}$ drift in each other's electric fields; this produces negligible heat transport, but is important for particle transport (as will be discussed in Chapter 5) and angular momentum transport [36]. These long-range collisions have very little effect on the perpendicular velocities of the particles: the collisions occur on a time scale which is long compared with the cyclotron orbit time, so the cyclotron action $J_\perp \equiv mv_\perp^2/B$ remains a good adiabatic invariant.

Figure 4.1 illustrates the fundamental differences between short-range and long-range collisions. In the top half of the figure, showing a short-range collision,

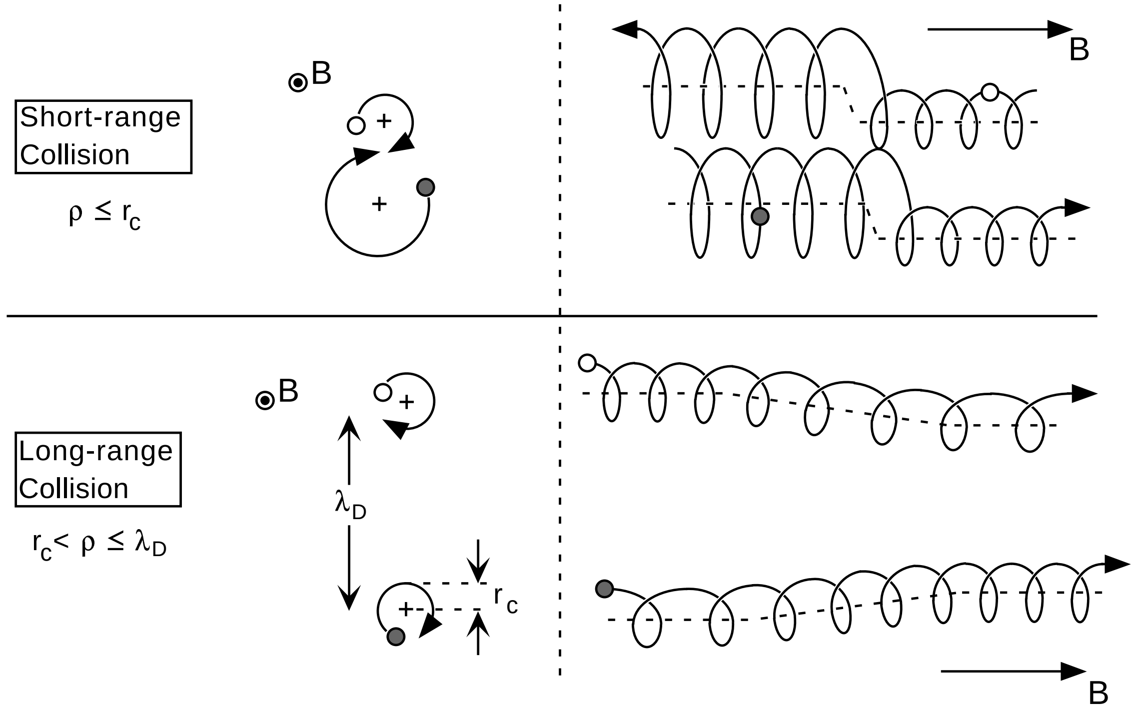

Figure 4.1: Illustration of short-range vs. long-range collisions.

a white particle, with small perpendicular temperature (small cyclotron radius), collides with a shaded particle, with large perpendicular temperature (large cyclotron radius). As a result of the 3-D velocity-scattering collision, the white particle gains perpendicular or parallel energy and steps radially, as the dotted guiding-center line indicates; the shaded particle loses the same energy and also steps radially.

In the lower half of the figure, showing a long-range collision, a white particle with small parallel energy interacts with a distant shaded particle with large parallel energy. As a result of the interaction, both particles drift across the field lines and the white particle gains parallel energy at the expense of the shaded particle.

Both short-range and long-range collisions cause cross-field transport; the dominant transport mechanisms for different plasma regimes are summarized in Table 4.1. Here, we display the test particle diffusion coefficient D, the thermal diffusivity χ, the kinematic viscosity η/nm, and appropriate references. For plasmas with

Regime and mechanism	Test Particle Transport D	Heat Transport χ	Viscous Transport η/nm
$\lambda_D \ll r_c$ short-range collisions	$\frac{5}{4}\nu_{ii}r_c^2$ [58, 39]	$\nu_{ii}r_c^2$ [52]	$\frac{3}{8}\nu_{ii}r_c^2$ [55, 39]
$\lambda_D \gg r_c$ 3-D long-range collisions	$6\sqrt{\pi}(nvb^2)r_c^2\ \ln(\lambda_D/r_c)$ $\times\ \ln\left[v/\left(\nu_{ii}v^2\sqrt{\lambda_D r_c}\right)^{1/3}\right]$ [19]; est. in [38]	$0.49(nvb^2)\lambda_D^2$ $+$ wave term [20]; est. of wave term in [53]	$\sim (nvb^2)\lambda_D^2$ $+$ wave term [46]
$\lambda_D \gg r_c$ $f_b \gg f_E$ 2-D bounce-averaged long-range collisions	$\sim (nvb^2)r_c^2$ [18]	N/A	$\sim (nvb^2)d_{res}^2$ [18]

Table 4.1: Transport coefficients for collisional cross-magnetic-field transport.

$\lambda_D \ll r_c$, no long-range collisions can occur, and collisional transport occurs as a result of short-range collisions only; the predicted transport coefficients are displayed in row 1 of Table 4.1. For plasmas with $\lambda_D \gg r_c$, both long-range and short-range collisions can occur; and in general long-range collisions dominate the transport, with the transport coefficients displayed in row 2. In plasmas where the axial bounce frequency is large compared with the rotation frequency, i.e. $f_b \gg f_E$, the long-range collisional transport becomes essentially 2-D in nature; and the resulting transport coefficients are shown in the last row. The term d_{res} of Table 4.1 is the maximum distance over which the charge rods can remain in rotational resonance; this is set by the level of rotational shear in the plasma [21].

4.1.1 Anisotropic Temperature Relaxation

In Section 4.2, we provide measurements of the classical ion-ion collision frequency in Mg$^+$ plasmas. Often, the rate at which these collisions occur is characterized by the ion-ion "momentum transfer" collision rate ν_{ii} (ν_{ee} for electrons)

[47]:

$$\begin{aligned} \nu_{ii} &= \frac{16}{15}\sqrt{\pi}\left(n v b^2\right)\ln(r_c/b) \qquad (4.1) \\ &\approx \left(1.0\,\mathrm{s}^{-1}\right)\left(\frac{T}{1\,\mathrm{eV}}\right)^{-3/2}\left(\frac{n}{10^7\,\mathrm{cm}^{-3}}\right)\left\{1 + 0.08\ln\left[\left(\frac{T}{1\,\mathrm{eV}}\right)^{3/2}\left(\frac{B}{1\,\mathrm{T}}\right)^{-1}\right]\right\}. \end{aligned}$$

The numerical form given in the second line of Equation 4.1 is appropriate for $^{24}\mathrm{Mg}^+$ ions. We have used the value of ν_{ii} calculated for a neutral plasma in a magnetic field [33] but with the Coulomb logarithm $\ln(r_c/b)$ appropriate for the ordering $\lambda_D > r_c$ [44]; for neutral plasmas with $\lambda_D < r_c$, the standard Coulomb logarithm $\ln(\lambda_D/b)$ would be used. Also, we have taken the limit of small anisotropy, $T_{\|} \simeq T_{\perp}$, and have neglected the lower impact parameter multiplier in the Coulomb logarithm (that is, we assume $\ln(A r_c/b) \simeq \ln(r_c/b)$, where we typically have $r_c/b \simeq 10^5$ and numerical estimates give $A \simeq 2.1$ [25]).

As can be seen from the first row of Table 4.1, classical short-range collisions result in transport coefficients which are proportional to $\nu_{ii}\, r_c^2$. In the plasmas studied here, the resulting classical transport is small compared with the transport resulting from long-range collisions (second row of Table 4.1); this will be verified in the present chapter for heat transport and in Chapter 5 for test particle transport. The measurements of the ion-ion collision frequency ν_{ii} presented in Section 4.2 thus represent our best test of classical transport in these plasmas; the cross-field transport measurements of Section 4.2 and Chapter 5 essentially provide tests of the second row of Table 4.1.

To measure the short-range velocity-scattering collision rate ν_{ii}, we measure the rate at which the temperature parallel to the magnetic field $T_{\|}$ becomes equilibrated with the temperature perpendicular to the magnetic field $T_{\perp}$. This anisotropic temperature relaxation rate is also referred to as the “equipartition rate”. In non-neutral plasmas at sufficiently low neutral gas pressures, the equipartition rate is dominated by short-range collisions. Because they act on a time scale which is long compared with the cyclotron motion, long-range collisions with impact parameters $r_c < \rho \leq \lambda_D$ are not expected to contribute to these measurements. Thus, the equipartition rate provides a measurement of the short-range ion-ion collision rate ν_{ii} in these systems.

The equipartition rate has been measured previously in pure electron plasmas over a wide range of temperatures, densities, and magnetic fields [6, 5, 31, 30]. Good agreement was found between the observed rate and the rate predicted for short-range electron-electron collisions [44, 33].

The equipartition experiments are performed by heating $T_{||}$ alone and measuring the relaxation back to $T_{||} = T_{\perp}$. To do this, a $m_\theta = 0$ signal is applied to one end of the plasma. As described in Section 2.5.3 and in Chapter 3, this "wiggle heating" deposits energy primarily into the parallel degree of freedom. This parallel heating is balanced by cooling from ion-neutral collisions, which act on both the parallel and perpendicular degrees of freedom. As a result, plasmas heated in this manner come to a equilibrium state in which the parallel temperature is larger than the perpendicular temperature. The rate at which the temperatures are observed to relax to a common value upon removing the wiggle heating gives the equipartition rate. The measured relaxation rate is found to agree well with the rate predicted for classical, short-range ion-ion collisions, ν_{ii}.

4.1.2 Collisional Cross-Magnetic-Field Heat Transport

The study of heat transport in plasmas is an area of research relevant to a wide variety of fields. For example, heat transport can be important in modeling the formation and dynamics of astrophysical objects, such as galactic clusters [50] or neutron stars [32]. In plasma processing, understanding of heat and particle transport is important in the design of plasma sources which are effective in etching small features on chips [60]. Heat and particle transport play a crucial role in magnetic fusion plasmas [61], where it is desirable to have good thermal confinement to generate fusion power, yet have imperfect particle confinement so that helium ash can be removed from the plasma.

Here, we present measurements of collisional heat transport in pure ion plasmas. As discussed in the previous sections, collisions in these plasmas can be grouped into classical short-range collisions and long-range collisions. Classical collisions are velocity-scattering collisions with impact parameter $\rho \leq r_c$. In the presence of a temperature gradient, short-range collisions result in a classical cross-field heat flux

$$\Gamma_{q,c} = -(5/2) n \chi_c \nabla T \,, \tag{4.2}$$

where χ_c is the classical thermal diffusivity of Table 4.1:

$$\begin{aligned} \chi_c &= \nu_{ii} r_c^2 \\ &\approx (2.5 \times 10^{-3}\,\mathrm{cm^2 s^{-1}}) \left(\frac{T}{1\,\mathrm{eV}}\right)^{-1/2} \left(\frac{B}{1\,\mathrm{T}}\right)^{-2} \left(\frac{n}{10^7\,\mathrm{cm^{-3}}}\right) \\ &\times \left\{1 + 0.08 \ln\left[\left(\frac{T}{1\,\mathrm{eV}}\right)^{3/2} \left(\frac{B}{1\,\mathrm{T}}\right)^{-1}\right]\right\} . \end{aligned} \tag{4.3}$$

We will show in Section 4.3 that a larger heat transport can result from long-range collisions. In plasmas with $\lambda_D > r_c$, for sufficiently gradual thermal gradient length scales (i.e. $L_T > \lambda_D$), we expect a diffusive heat flux due to these collisions of

$$\Gamma_{q,L} = -(5/2) n \chi_L \nabla T_{\|} \,. \tag{4.4}$$

The thermal diffusivity resulting from long-range collisions, χ_L, can be estimated as follows: particles on separate field lines can exchange energy up to a distance λ_D, so we take a step size for the diffusion process of $\Delta r \sim \lambda_D$. Interacting particles with very different velocities will not exchange energy: a very fast particle on field line 1 passing by a stationary particle on field line 2 at $\Delta r \simeq \lambda_D$ will push the particle forward as it approaches, then push the particle backward as recedes, resulting in no net transfer of energy. Of course, this does not apply for head-on collisions, but since $\lambda_D \gg b$, head-on collisions can be neglected here. Significant exchange of energy will occur if the relative kinetic energy of the particles is comparable to the mutual electrostatic energy, i.e. $m\Delta(v^2) \sim e^2/\lambda_D$, so we expect the transport to be dominated by particles with $\Delta v \sim e^2/(mv\lambda_D) = v\,(b/\lambda_D)$. The number of particles satisfying this velocity difference are: $\Delta n \sim n\,(\Delta v/v) \sim n\,(b/\lambda_D)$. The estimated thermal diffusivity is then: $\chi_L \sim (\Delta n \Delta v \lambda_D^2)\,\lambda_D^2 \sim (nvb^2)\,\lambda_D^2$. A more detailed calculation of the long-range thermal diffusivity gives the thermal diffusivity of Table 4.1 [20]:

$$\begin{aligned} \chi_L &= 0.49\left(nvb^2\right)\lambda_D^2 \\ &\approx \left(1.1 \times 10^{-3}\,\mathrm{cm^2 s^{-1}}\right)\left(\frac{T}{1\,\mathrm{eV}}\right)^{-1/2} . \end{aligned} \tag{4.5}$$

Thus, we expect to observe a total cross-field heat flux Γ_q given by:

$$\Gamma_q = -\frac{5}{2} n (\chi_L \nabla T_{\|} + \chi_c \nabla T) + \Gamma_{ND} \,, \tag{4.6}$$

where $\nabla \equiv \partial/\partial r$. We have separately identified $T_{\|}$ to emphasize the unusual nature of χ_L, but for the data presented here we can approximate $T_{\perp} \simeq T_{\|} \simeq T$ to adequate accuracy. The term Γ_{ND} represents a possible heat flux due to non-diffusive effects such as waves or convection. In general, we observe no consistent signature of these effects, so we take $\Gamma_{ND} = 0$.

Comparing Equations 4.3 and 4.5 suggests that the collisional heat transport will be dominated by long-range collisions in plasmas with $\lambda_D \gtrsim 7\,r_c$. Nonneutral plasmas are commonly in this regime due to the Brillouin density limit [8, 14] and electrons in some neutral plasmas are in this regime, i.e. $\lambda_D \gtrsim 7\,r_{c,e}$.

Here, heat transport measurements are made on plasmas consisting of uncorrelated Mg^+ ions with temperatures $5 \times 10^{-4} < T < 0.5$ eV, densities $2 \times 10^7 < n < 10^8\,\mathrm{cm}^{-3}$, and magnetic fields $1 < B < 4$ T. The thermal gradient length scales for these measurements are in the range $\lambda_D < L_T < 100\,\lambda_D$. These parameters correspond to the regime in which the heat transport is predicted to be diffusive and dominated by long-range collisions, i.e. we expect $\chi \simeq \chi_L \gg \chi_c$ and $\Gamma_{ND} = 0$; for $L_T > 100\,\lambda_D$, wave (non-diffusive) transport is predicted to become important [20], but this has not been observed here.

These measurements are complicated by the presence of small heat sources, which can change the plasma temperature at a given radius even in the absence of radial heat flow. In these experiments, the dominant sources of heat are believed to be Joule heating, rotating wall heating, and collisions with neutral molecules. Joule heating results from plasma expansion, in which electrostatic energy is converted into kinetic energy. As discussed in Chapter 3, the radial expansion of plasmas confined in these traps is believed to be dominated by trap asymmetries which drag on the plasma. This radial expansion can be counteracted by applying a rotating wall field to the plasma; in this case Joule heating from the plasma expansion is replaced by (generally slightly stronger) heating from the rotating wall drive. Collisions with background (H_2) neutral molecules will tend to bring the plasma into thermal equilibrium with the room-temperature walls, so we expect plasma heating for temperatures $T \lesssim 0.03$ eV and plasma cooling for $T \gtrsim 0.03$ eV.

We represent these small heat sources by a term $\dot{q}_{ext}$ added to the conservation of energy equation:

$$\dot{q} = -\nabla \cdot \Gamma_q + \dot{q}_{ext} \,, \tag{4.7}$$

where the kinetic energy density q is:

$$q \equiv \frac{3}{2} n T \,. \tag{4.8}$$

In the heat transport experiments presented here, the particle density n is essentially constant with time, so $\dot{q} = d/dt(\frac{3}{2}nT) \simeq \frac{3}{2}n\, dT/dt$.

Two different methods of measuring and analyzing the heat transport are presented here, which we will designate as "large temperature gradient method" and "small temperature gradient method". The fundamental difference between the two methods is the way in which the external heating correction $\dot{q}_{ext}$ is removed from the measured $\dot{q}$. In both methods, a plasma is initially prevented from expanding by applying a rotating wall field. Both the large temperature gradient and small temperature gradient methods give a radial heat flux which is diffusive in nature and dominated by long-range collisions; that is, we measure a thermal diffusivity $\chi \approx \chi_L$ and a non-diffusive contribution $\Gamma_{ND} \simeq 0$.

For the large temperature gradient method, the plasma is initially cooled or heated by a strong, narrow manipulating beam passed along the central axis ($r = 0$) of the plasma. In general, this creates a large radial temperature gradient in the plasma; for some initial conditions, the central plasma temperature is less than 10^{-3} eV, while the edges of the plasma are at about 0.05 eV (corresponding to a radial temperature variation of more than a factor 50 across the plasma). At time $t = 0$, the manipulating beam and rotating wall are switched off; the plasma is then observed to evolve toward a flat radial temperature profile. This temperature evolution occurs dominantly as a result of radial heat flux driven by the large temperature gradient. The heat sources are a small contribution to the temperature evolution; these terms are obtained from independent measurements and subtracted from the data to obtain the heat flux.

For the small temperature gradient method, the plasma is *uniformly* heated or cooled by a strong, wide manipulating beam passed at an angle through the plasma. This wide manipulating beam continuously illuminates a large area of the ion cloud and is used to create an initial equilibrium state characterized by a flat radial temperature profile. To create a temperature gradient in the plasma, a weaker, narrow manipulating beam is then passed along the central axis ($r = 0$) of the plasma. This results in a second equilibrium state characterized by a small temperature gradient (typically a factor of 2 or less variation in temperature across the plasma). At time $t = 0$, the narrow manipulating beam is switched off; the plasma is then observed to evolve from the second (small temperature gradient) equilibrium to the first (no temperature gradient) equilibrium. Here, the background heating terms are estimated by linearizing about the first equilibrium state, where it is know that the external heating terms sum to zero at each radius. Conservation of energy is then used to calculated the magnitude of the external terms from the measurements. The background heating terms are assumed to depend only weakly on radius, but otherwise no knowledge of these terms is presumed.

In the final section of this chapter, measurements of the background heat sources resulting from Joule heating and neutral collisions are presented. The measurements are found to be in reasonable agreement with a simple model of Joule heating based on an empirical fit to observed plasma expansion rates plus neutral heating based on the known polarizability of H_2 molecules. These results are used to estimate the small corrections used in the large temperature gradient heat transport measurements.

4.2 Equipartition Rate Measurements

A typical initial condition used for measuring the equipartition rate is shown in Figure 4.2. Here, a magnesium ion plasma of length $L_p \simeq 12$ cm is trapped in the region S11→R13 in a magnetic field $B = 4$ T. Radial expansion is counteracted by a $m_\theta = +1$, $f_s = 10$ kHz, $A_w = 1$ V rotating wall field applied using ring S11. The plasma is heated by applying a $m_\theta = 0$, $f_s = 15$ kHz, $A_w = 1$ V signal on ring R13. This “wiggle heating” heats the parallel degree of freedom, resulting in an initial condition with parallel temperature $T_\| \simeq 1.6$ eV and perpendicular temperature $T_\perp \simeq 1.1$ eV. Both parallel and perpendicular degrees of freedom are

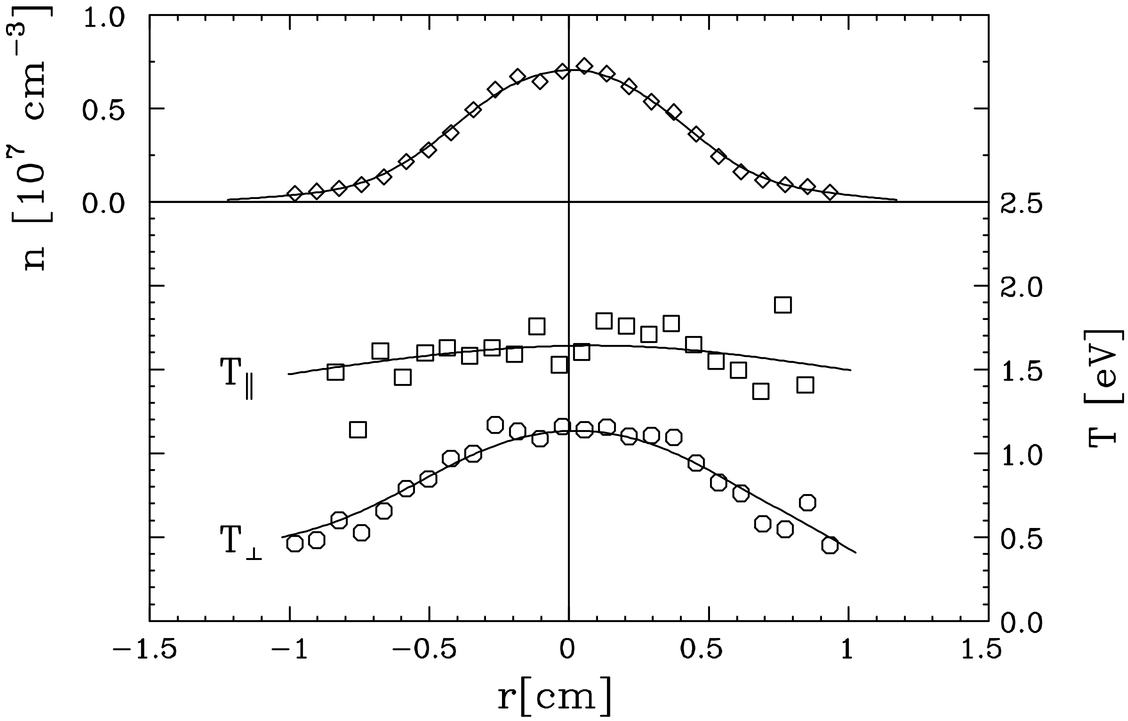

Figure 4.2: Radial profile with wiggle heating showing anisotropy $T_\parallel > T_\perp$ between parallel and perpendicular temperatures.

cooled through collisions with the room-temperature background neutrals. Aside from chemical reactions which occur on a very slow ($\sim$ 1 day) time scale, the plasma is in steady-state equilibrium. The radial temperature gradients in the plasma are gradual, so we expect radial heat transport to be small here.

The parallel and perpendicular temperatures at each radial position are expected to evolve as:

$$\begin{aligned} dT_\parallel/dt &= -\frac{2}{3}\nu_{\perp 0}(T_\parallel - T_\perp) - \nu_{iN}(T_\parallel - T_N) + \nu_{\rm wig}T_\parallel \\ dT_\perp/dt &= -\frac{1}{3}\nu_{\perp 0}(T_\perp - T_\parallel) - \nu_{iN}(T_\perp - T_N)\ . \end{aligned} \tag{4.9}$$

Here, we neglect radial heat flow and the small heating terms resulting from the rotating wall field and/or the plasma expansion. The term $\nu_{\rm wig}T_\parallel$ in Equation 4.9 represents the wiggle heating of the parallel degree of freedom; the precise form of this term is not important here. ν_{iN} is the ion-neutral collision frequency, $T_N = 0.026$ eV is the temperature of the neutral atoms, and $\nu_{\perp 0}$ is the equipartition rate resulting from short-range ion-ion collisions. This equipartition rate can also be characterized by $\nu_{\perp\|}$, where $\nu_{\perp 0} = 1.5\nu_{ii} = 3\nu_{\perp\|}$.

The collisional equipartition rate $\nu_{\perp 0}$ is measured by turning off the wiggle heating and rotating wall at time $t = 0$ and measuring the resulting time evolution of $T_\perp$ and $T_\|$. All the temperature evolution measurements discussed here are taken at the center of the plasma, $r = 0$.

For times $t > 0$ the wiggle heating is turned off, so $\nu_{\mathbf{wig}} = 0$. Equation 4.9 then gives:

$$\Delta T(t) = \Delta T(0) \mathrm{e}^{-\nu_{eq}\Delta T} \ , \tag{4.10}$$

where $\Delta T(t) \equiv T_\|(t) - T_\perp(t)$ is the temperature anisotropy and $\nu_{eq} \equiv \nu_{\perp 0} + \nu_{iN}$ is the total equipartition rate. In the initial ($t \leq 0$) steady-state condition, we have $d/dt = 0$, so ν_{iN} is known from Equation 4.8:

$$\nu_{iN} = \nu_{\perp 0} \frac{\Delta T(0)}{3(T_\perp(0) - T_N)} \ . \tag{4.11}$$

The equipartition rate $\nu_{\perp 0}$ can thus be obtained from the total (measured) equipartition rate ν_{eq}, the known neutral temperature T_N, and the known initial plasma temperature $T(t = 0)$:

$$\nu_{\perp 0} = \nu_{eq} \frac{(T_\perp(0) - T_N)}{(T(0) - T_N)} \ . \tag{4.12}$$

Here, we have approximated $\nu_{\perp 0}$ and ν_{iN} as being constant over the range of temperatures covered in the experiment.

Figure 4.3 shows the measured central ($r = 0$) temperature relaxation of the initial condition shown in Figure 4.2. The measured time evolution of the temperatures $T_\|(t)$ and $T_\perp(t)$ is plotted, as well as the difference, $\Delta T(t)$. It can be seen that the temperatures are constant for the initial condition $t \leq 0$. After the rotating wall

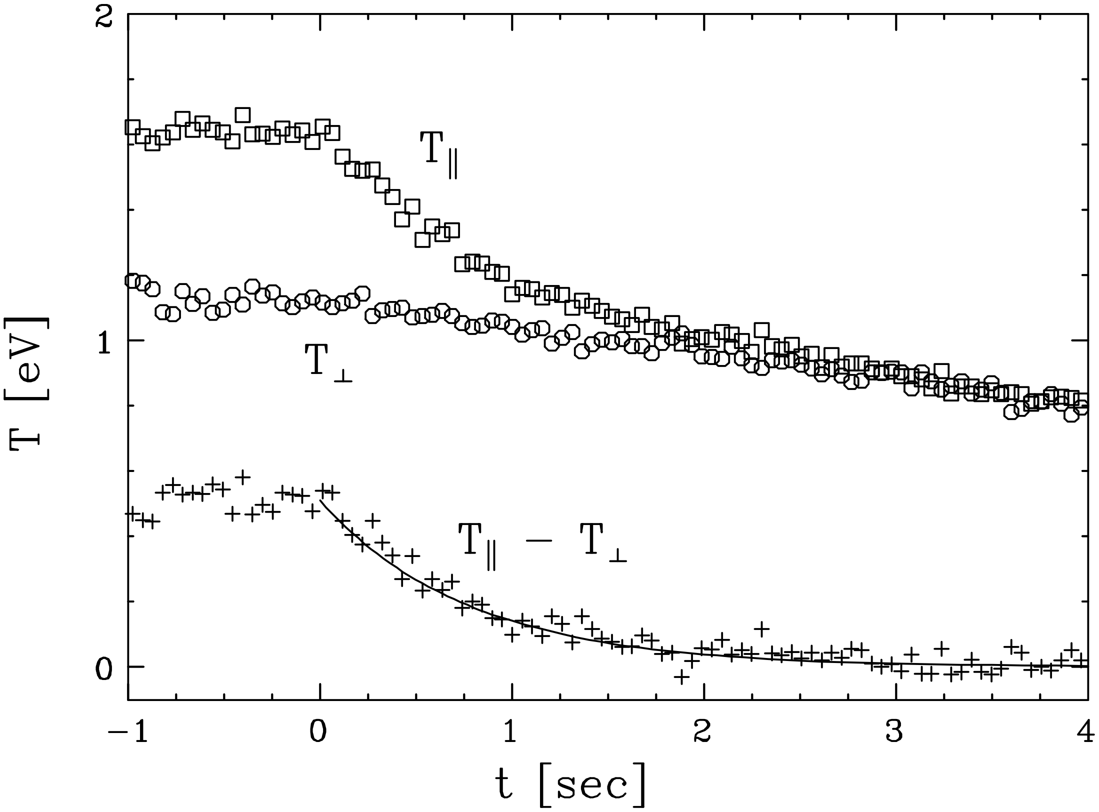

Figure 4.3: Relaxation of the initial temperature anisotropy measured at $r = 0$.

and wiggle heating are turned off (at $t = 0$), the temperatures are seen to equilibrate within about 2 seconds as a result of ion-ion collisions. A slow cooling of the plasma toward $T \simeq T_N \simeq 0.026$ eV as a result of ion-neutral collisions then dominates the temperature evolution. The solid curve is a fit to $\Delta T(t)$ of the form given in Equation 4.10 using the adjustable parameter $\nu_{eq} = 1.29\,\mathrm{s}^{-1}$ and the measured quantity $\Delta T(t = 0) = 0.51$ eV. It can be seen that the measured temperature evolution is well-described by the expected exponential relaxation of Equation 4.10. The collisional equipartition rate is then obtained from Equation 4.12, giving $\nu_{\perp 0} \simeq 1.1\,\mathrm{s}^{-1}$ at an average temperature $T \simeq 1.3$ eV and a density $n \simeq 7.0 \times 10^6\,\mathrm{cm}^{-3}$.

The equipartition rate was measured for initial conditions with average temperatures $0.6 \leq T \leq 2.0$ eV, densities $5 \times 10^6 \leq n \leq 5 \times 10^7\,\mathrm{cm}^{-3}$, and magnetic field $B = 4$ T. The value of $\nu_{\perp 0}$ obtained from the measurements is plotted in Figure 4.4

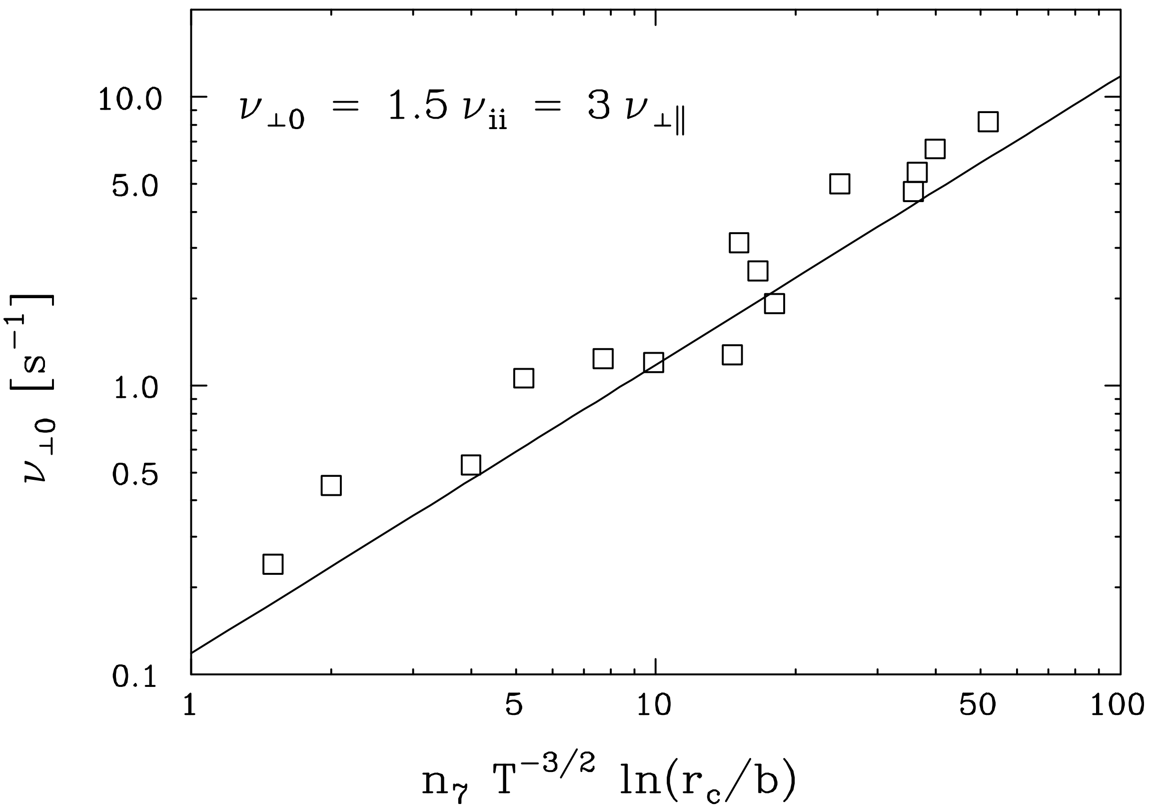

Figure 4.4: Measured collisional relaxation rate $\nu_{\perp 0}$ as a function of scaled density n_7 and temperature T.

as a function of $n_7 T^{-3/2} \ln(r_c/b)$, where $n_7 \equiv n/10^7\,\text{cm}^{-3}$ and T is in eV.

The expected value for the equipartition rate resulting from ion-ion collisions is $\nu_{\perp 0} = \frac{3}{2}\nu_{ii}$, where ν_{ii} is the short-range (momentum-transfer) collision rate of Equation 4.1. The solid line in Figure 4.4 corresponds to the prediction of Equation 4.1. It can be seen that the observed temperature relaxation rate is well-fit by the classical prediction. Based on these measurements, we believe that the classical description of short-range ion-ion collisions at rate ν_{ii} is correct for the ion plasmas discussed here. These short-range collisions are expected to give classical cross-field transport coefficients described by the first row of Table 4.1.

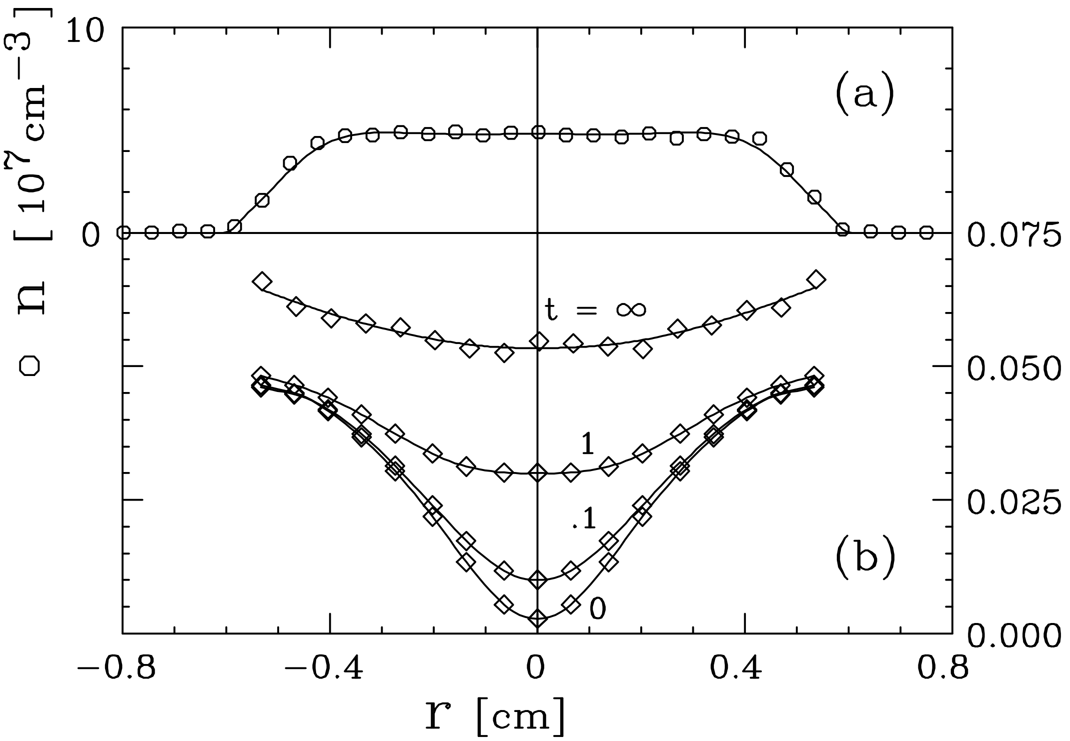

Figure 4.5: Measured thermal diffusion starting with large temperature gradient created by local cooling at $r = 0$. Data points at $t = 0$, 0.1, and 1 are smoothed radially; data at $t = \infty$ is unsmoothed and shows the characteristic level of scatter in the data.

4.3 Measurements of Cross-Magnetic-Field Heat Transport

4.3.1 Large Temperature Gradient Method

"Large temperature gradient" heat transport experiments are performed by locally heating or cooling along the $r = 0$ axis of the plasma with a strong ($\approx$ 1 mW), narrow manipulating beam, thus creating an initial condition with a strong radial temperature gradient. The manipulating beam is then blocked with the shutter, and the resulting rapid time evolution of the plasma temperatures $T_\perp(r,t)$ and $T_\parallel(r,t)$ is measured using a weak ($\approx 10\,\mu$W) probe beam. For the data discussed here, $T_\perp \simeq T_\parallel \simeq T$.

A typical heat flux experiment is shown in Figure 4.5. Here, a length $L_p \simeq 12$ cm plasma in a vacuum of $P_N \simeq 4 \times 10^{-9}$ Torr is initially held in steady-state at $n \simeq 5 \times 10^7\,\mathrm{cm}^{-3}$ through application of a $f_s = 20$ kHz, $A_w = 0.5$ V, $m_\theta = +1$ rotating wall field. The plasma is cooled at $r = 0$ to an initial steady-state central temperature of $T(r = 0, t = 0) \simeq 3 \times 10^{-3}$ eV. At $t = 0$, the manipulating beam and the rotating wall field are turned off and the plasma temperature is observed to flatten and move toward the normal (unperturbed) equilibrium temperature of $T \simeq 0.05$ eV.

The temperature evolution seen in Figure 4.5 is measured using a single weak probe beam. The time evolution of the temperature can only be measured one radius at a time; repeating the heat flux experiment is thus necessary to reconstruct $T(r,t)$, the time evolution of the entire radial temperature profile. The initial ($t \leq 0$) steady-state density and temperature profiles and the subsequent time evolution of the temperature $T(r,t)$ are measured using the LIF technique described in section 2.4.1. For clarity, only times $t = 0$, 0.1, 1 second, and the final equilibrium state $t \to \infty$ are shown; actually, the temperature evolution is measured with 100 time steps over $0 < t < 4$ sec for each radial position. The $t \to \infty$ data is measured separately when the plasma has reached steady-state ($t \gtrsim 50\,\mathrm{s}$). The data points plotted at $t = 0$, 0.1, and 1 correspond to smoothed curves with forced radial symmetry; the points on the $t \to \infty$ curve are actual data and show the level of scatter in T characteristic to this measurement. The manipulating beam is chopped for these experiments (typically at 50 Hz) and the scattered photons from the probe beam are counted synchronously with the chopper to avoid counting photons from the manipulating beam.

The temperature evolution of Figure 4.5 results from radial heat flux plus small external heating terms. The radial heat flux Γ_q is obtained from the measured

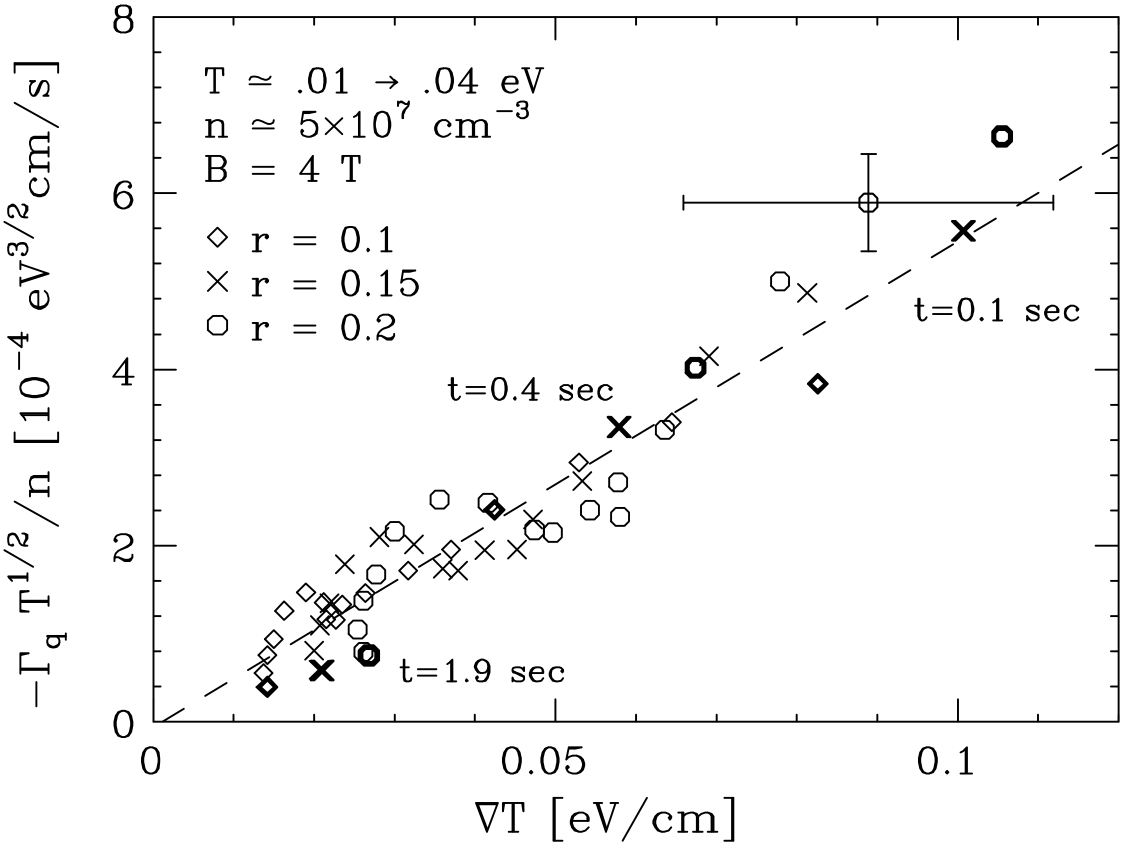

Figure 4.6: Measured normalized radial heat flux vs. temperature gradient for experiment shown in Figure 4.5, demonstrating diffusive heat transport. Error bars are characteristic for all data points.

change in local temperature $\dot{T}(r,t)$ by integrating Equation 4.7:

$$\Gamma_q(r,t) = -\frac{1}{r}\int_0^r r'dr'\,[\dot{q}(r',t) - \dot{q}_{ext}(r',t)]\ , \tag{4.13}$$

where $\dot{q} = \frac{3}{2}n\dot{T}$ and the weak external heating or cooling term $\dot{q}_{ext}$ is known from measurements described in Section 4.3. An improved estimate of $\dot{q}_{ext}$ is obtained for each time step by normalizing $\dot{q}_{ext}$ to maintain energy conservation in the evolution: that is, we require $\int_0^{R_w} rdr\dot{q} = \int_0^{R_w} rdr\dot{q}_{ext}$. Typically, we find a normalization factor between 1 and 3, consistent with the factor-of-two uncertainty in the model. For the heat transport data presented here, the correction to Γ_q due to the external heating terms is small, since $\dot{q}_{ext}/\dot{q} \simeq 0.1$ in the regions with a large temperature gradient.

In Figure 4.6, we plot the measured radial heat flux Γ_q as a function of the temperature gradient ∇T obtained from the data of Figure 4.5. We plot the heat flux measured at radii $r = 0.1$, 0.15, and 0.2 cm, and at times $t = 0.1$ to 1.9 sec; these radii were chosen here because they have a strong gradient and strong signal, i.e. $\dot{q} \gg \dot{q}_{ext}$. It can be seen that the gradients and fluxes are largest at early times, and decrease as the temperature profile relaxes toward equilibrium. Classical theory predicts a heat flux

$$\Gamma_{q,c} \propto n\chi_c \nabla T \propto n^2 T^{-1/2} \nabla T \ , \tag{4.14}$$

while long-range theory predicts

$$\Gamma_{q,L} \propto n\chi_L \nabla T \propto n T^{-1/2} \nabla T \ . \tag{4.15}$$

Here, we anticipate that long-range collisions will dominate, so we divide the displayed Γ_q by $nT^{-1/2}$ to better illustrate the proportionality of flux with ∇T. Typically, the density n does not vary significantly over the region of valid data and the temperature T varies by about a factor 2, so this normalization does not significantly effect the results shown here. The dashed line shown in Figure 4.6 is an unconstrained (arbitrary offset, error-weighted) linear fit to the data. The small non-zero intercept could represent a non-diffusive flux; but here it seems to be insignificant, arising from uncertainties in the data or imperfect corrections $\dot{q}_{ext}$; thus, Figure 4.6 demonstrates diffusive heat transport.

We calculate the local thermal diffusivity χ for each data point of Figure 4.6 using

$$\chi(n, B, T) = -\frac{2}{5n} \left(\Gamma_q / \nabla T \right) \ . \tag{4.16}$$

Values of $\chi(n, B, T)$ were obtained for different equilibrium plasmas covering a range of 50 in density, 10^3 in temperature, and 4 in magnetic field.

In Figure 4.7, we plot the measured χ as a function of temperature T. Here, to reduce the number of data points displayed, we plot a single average χ of each evo-

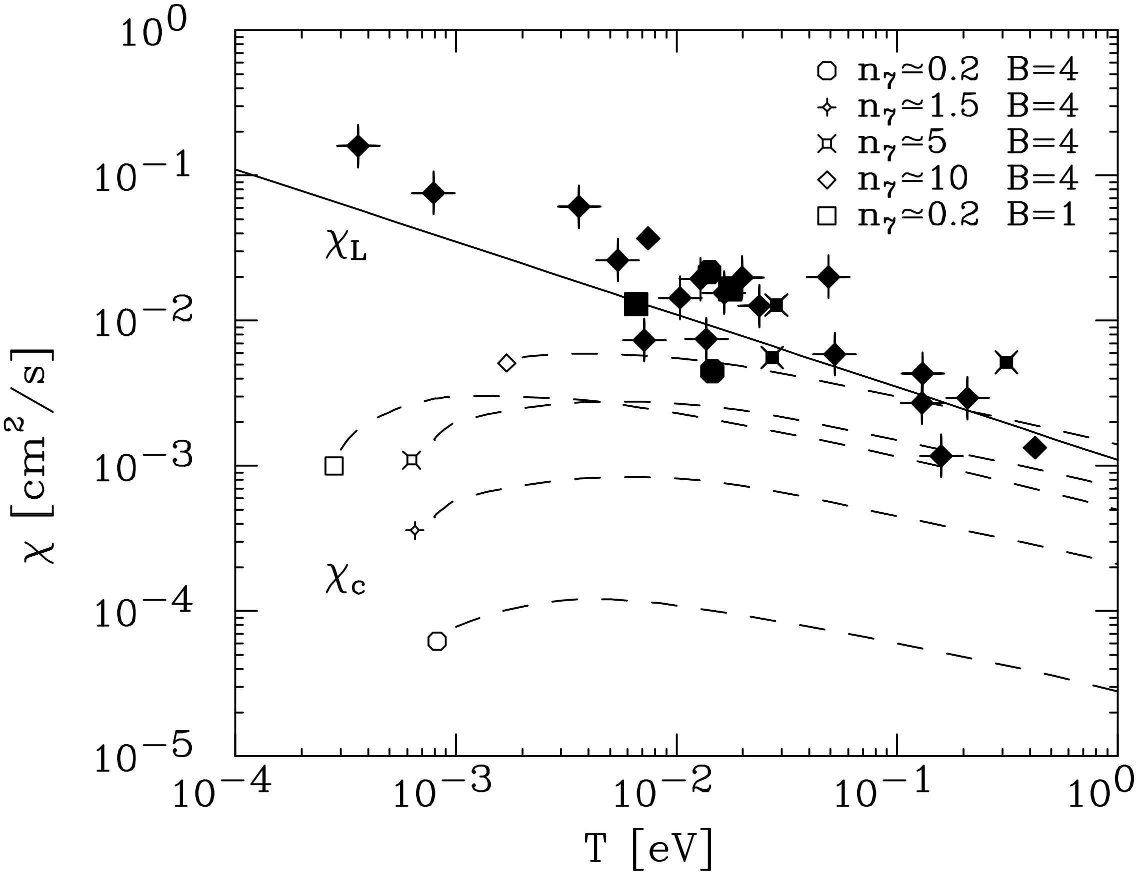

Figure 4.7: Measured cross-magnetic-field thermal diffusivity χ plotted as a function of temperature T for large temperature gradient data. Hollow points label theory curves; each solid point corresponds to the average measured χ from an experiment such as Figure 4.5.

lution such as Figure 4.6; that is, we plot $\chi \simeq \frac{2}{5}\langle \Gamma_q T^{1/2}/n\nabla T\rangle\langle T\rangle^{-1/2}$ as a function of $T \simeq \langle T\rangle$ where the brackets $\langle\ \rangle$ represent an error-weighted average over the data points of the evolution. This averaging, which is introduced to reduce the number of data points displayed, is of little consequence since the ranges of n, T, and χ in a single evolution are small. The dashed curves in Figure 4.7 show the predicted classical thermal diffusivities χ_c for the 5 densities and magnetic fields used. The solid line shows the predicted long-range thermal diffusivity χ_L, which depends only on temperature.

The measured thermal diffusivities are up to 100 times larger than the classical prediction, and are independent of B and n. The $T^{-1/2}$ scaling is observed over 3 decades in T, and extends into the low-temperature regime where $r_c \approx b$. A fit to Figure 4.7 with $\chi \propto T^{-1/2}$ gives $\chi = [(1.92 \pm 1) \times 10^{-3}\ \mathrm{cm}^2\mathrm{s}^{-1}]\,(T/1\,\mathrm{eV})^{-1/2} = (0.84 \pm .5)\ \nu\lambda_D^2$. We therefore measure a thermal diffusivity $\chi \simeq 1.7\,\chi_L$, which we take to be a reasonable agreement with the expected value $\chi = \chi_c + \chi_L \simeq \chi_L$, given the scatter in the data of Figure 4.7.

4.3.2 Small Temperature Gradient Method

In this section, cross-field heat transport results are presented for plasmas which have been perturbed with two manipulating beams: a strong ($\approx$ 1 mW) wide, angled beam is used to uniformly heat or cool the entire plasma, and a strong ($\approx$ 1 mW) narrow, aligned beam is used to create a small additional localized temperature perturbation along the central axis of the plasma. The narrow cooling beam is then blocked with a shutter, and the subsequent temperature evolution is measured using a weak ($\approx$ 10 μW) probe beam. The rotating wall is left on during this process, so these experiments can be thought of as perturbations about a known equilibrium. The measurement method used is the same as described in the previous section; that is, standard frequency-scan LIF is used to obtain the density and temperature profiles of the equilibrium states, while the peaks of the velocity distribution functions are probed to obtain the rapid temperature evolutions.

A typical small temperature gradient heat transport experiment is shown in Figure 4.8. Here, the ion plasma is prevented from expanding radially by applying a f_s = 10 kHz, A_w = 1 V, m_θ = +1 rotating wall field. The plasma is cooled uniformly to a temperature $T \simeq 7 \times 10^{-4}$ eV with a wide manipulating beam which passes through the spinning ion cloud at an angle; the resulting equilibrium state is shown by the temperature curve $t = \infty$. Initially, additional cooling is provided at $r = 0$ by applying a narrow manipulating beam which passes along the axis of the

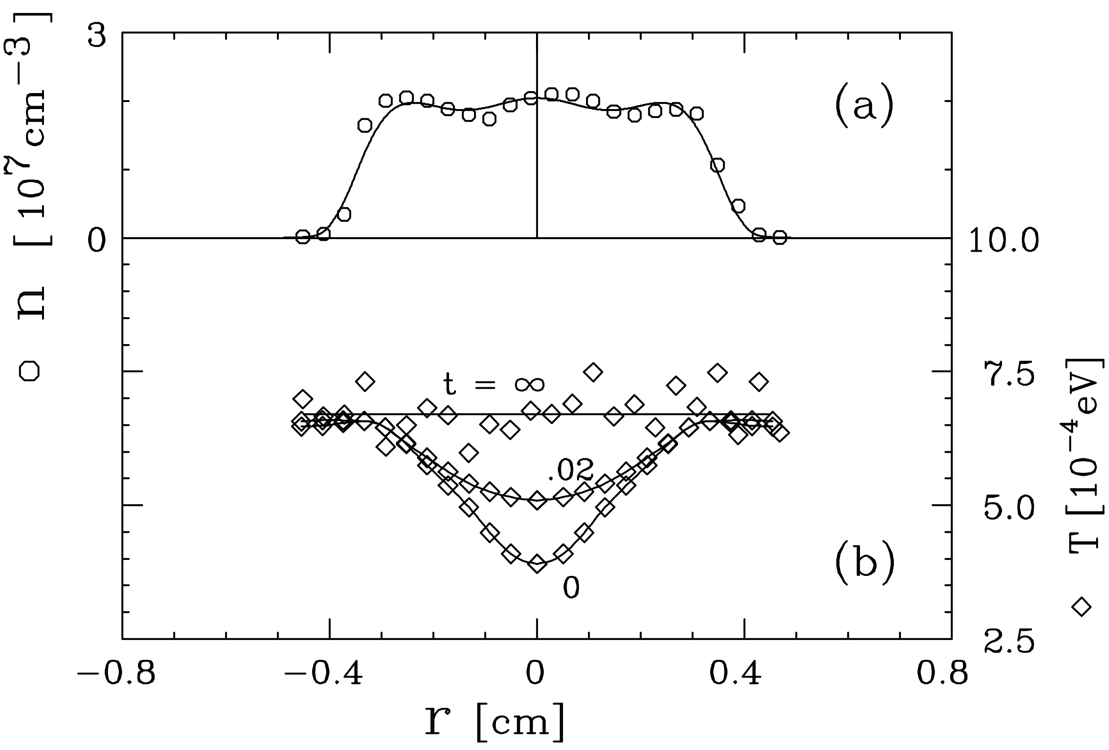

Figure 4.8: Measured thermal diffusion in a globally cooled plasma starting with a small temperature gradient created by additional local cooling at $r = 0$. Data points at $t = 0$ and 0.02 are smoothed radially; data at $t = \infty$ is unsmoothed and shows the characteristic level of scatter in the data.

plasma; this results in a central temperature of $T \simeq 4 \times 10^{-4}$ eV, as seen on the curve labeled $t = 0$.

At time $t = 0$, the narrow manipulating beam is turned off and the plasma temperature relaxes toward the $t = \infty$ equilibrium state. Here, for clarity, we show only the time steps $t = 0$ and 0.02 seconds of this temperature evolution in Figure 4.8(b). The data points marked on the $t = 0$ and $t = 0.02$ line are smoothed, interpolated values with forced radial symmetry. The points on the $t = \infty$ curve are actual data and are displayed to show the level of scatter in the data.

The radial heat flux Γ_q for this experiment is obtained from the measured temperature evolution $T(r, t)$ using Equation 4.13, as was done for the large temperature gradient experiments. Here, however, we will not assume the external source term $\dot{q}_{ext}$ to be known from separate measurements; instead we linearize the source terms about the final equilibrium condition $T_\infty \equiv T(t = \infty)$:

$$\dot{q}_{ext}(r, T) \simeq \dot{q}_{ext}(r, T_\infty) + \delta T \, \frac{\partial}{\partial T}(\dot{q}_{ext}(r, T_\infty)) \; , \tag{4.17}$$

where $\delta T \equiv T - T_\infty$. We know that the final equilibrium condition is steady-state, i.e. $\dot{q}_{ext}(r, T_\infty) \simeq 0$. We assume that the radial variation of $\frac{\partial}{\partial T}(\dot{q}_{ext}(r, T_\infty))$ is small over the region where δT is large. We can then approximate the external heating as:

$$\dot{q}_{ext}(r, T) \simeq \beta \, \delta T(r, t) \; , \tag{4.18}$$

where $\beta \equiv \frac{\partial}{\partial T}\dot{q}_{ext}(T_\infty)$ is known from energy conservation: $\beta = (\int \dot{q} r dr)/(\int \delta T r dr)$.

In Figure 4.9, we plot the measured radial heat flux Γ_q as a function of the temperature gradient ∇T obtained from the data of Figure 4.8 using β to correct for external heating terms. We plot the heat flux measured at radii $r = 0.05$, 0.1, and 0.15 cm, and at times $t = 0.01$ to 0.05 sec. Again, we divide the displayed Γ_q by $nT^{-1/2}$ to better illustrate the proportionality of flux with ∇T. The dashed line shown in Figure 4.9 is an unconstrained fit to the data. A larger non-zero intercept is seen than was observed in Figure 4.6; but this offset is believed to arise from uncertainties in the data or imperfect corrections $\dot{q}_{ext}$. We thus calculate the thermal diffusivity χ for each point of Figure 4.9 from a straight line fit passing through the origin (Equation 4.16).

The small temperature gradient method was used to obtain the thermal diffusivity χ for plasmas with densities $n \simeq 5 \times 10^6$ and $2.4 \times 10^7\ \mathrm{cm}^{-3}$, magnetic field $B = 1$ and 4 Tesla, and temperatures $5 \times 10^{-4} < T < 0.2$ eV. The resulting values of χ are displayed in Figure 4.10; again, as in Figure 4.7, we display an average χ for each temperature evolution such as Figure 4.8. A fit to Figure 4.10 with $\chi \propto T^{-1/2}$ gives $\chi = ((1.61 \pm 0.8) \times 10^{-3}\,\mathrm{cm^2 s^{-1}})\,(T/1\,\mathrm{eV})^{-1/2} = (0.70 \pm .4)\ \nu \lambda_D^2$. We thus obtain $\chi \simeq 1.4\,\chi_L$, which is in reasonable agreement with the result of the previous section $\chi \simeq 1.7\,\chi_L$ and with the expected value $\chi = \chi_c + \chi_L \simeq \chi_L$.

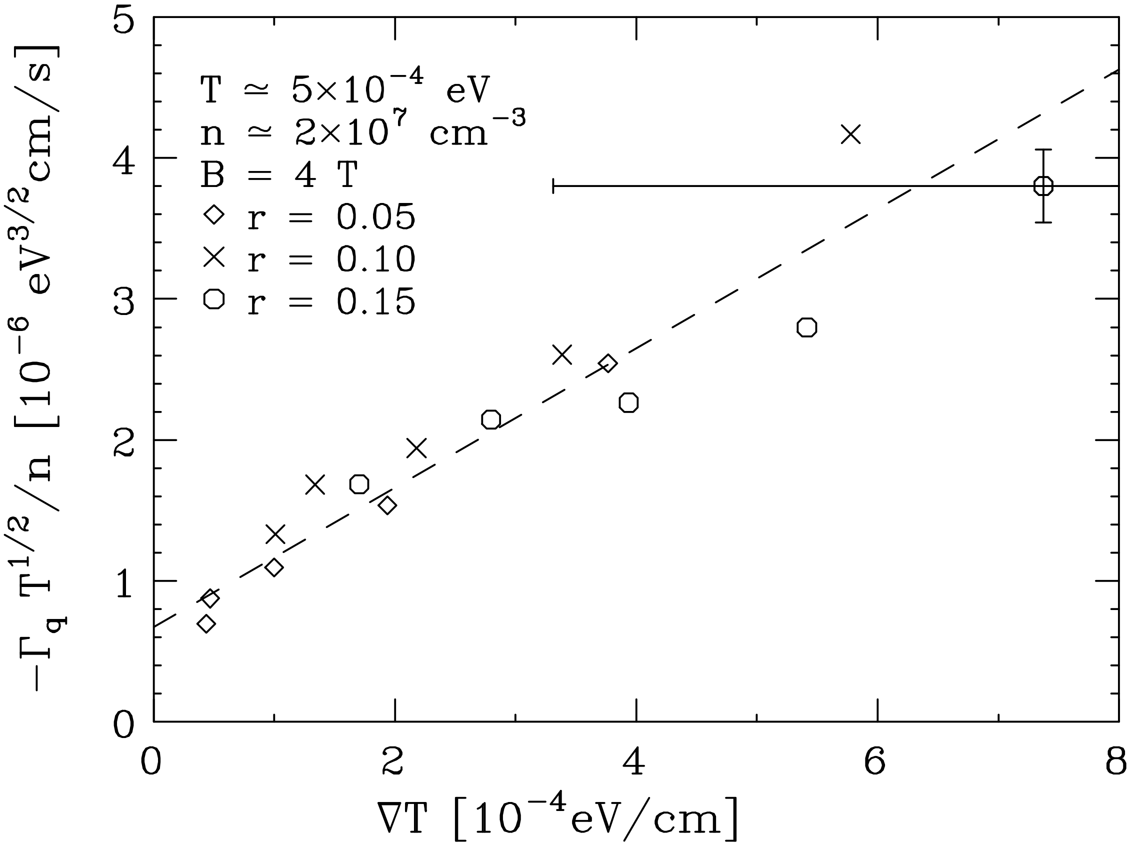

Figure 4.9: Measured normalized radial heat flux vs. temperature gradient for experiment shown in Figure 4.8, demonstrating diffusive heat transport. Error bars are characteristic for all data points.

4.3.3 Background Heating Corrections

In this section, models are presented to predict the ion plasma heating resulting from plasma expansion and the heating or cooling resulting from collisions with neutrals. Measurements of the heating and cooling rates of ion plasmas are presented; the measurements are found to be in reasonable agreement with the predicted rates.

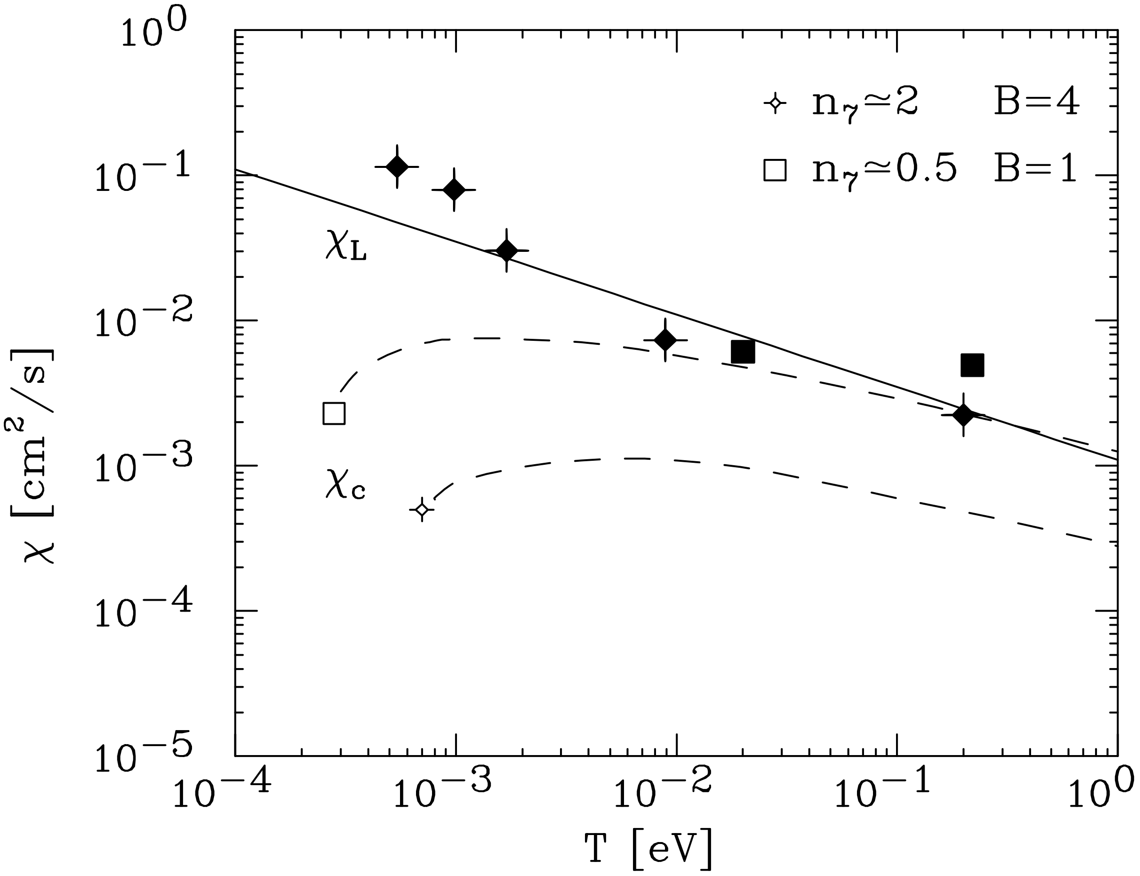

Figure 4.10: Measured thermal diffusivity χ for data taken with small temperature gradient method. Hollow points label theory curves; each solid point corresponds to the average measured χ from an experiment such as Figure 4.8.

Joule Heating Rate

The radial expansion of these plasmas as a result of coupling to inherent trap asymmetries converts electrostatic energy into kinetic energy; this is referred to as "Joule heating". In Appendix D, an empirical model for the radial particle flux Γ_m of a radially-expanding ion plasma is presented (Equation D.3). If we assume that the radial transport results from static field errors, then the energy of the plasma in the lab frame is conserved. Converting the loss of electrostatic energy at each radius into local heating gives:

$$\dot{q}_J = \mathbf{J} \cdot \mathbf{E} = env_r E_r = \frac{eB}{c} 2\pi f_E r \Gamma_m \qquad (4.19)$$

$$\approx \left(1.7\times10^{4}\,\mathrm{eV cm^{-3}s^{-1}}\right)\left(\frac{B}{1\,\mathrm{T}}\right)^{-1}\left(\frac{L_p}{10\,\mathrm{cm}}\right)^{2}\left(\frac{r}{R_p}\right)^{2}\left(\frac{n}{10^7\,\mathrm{cm^{-3}}}\right)\left(\frac{f_E}{1\,\mathrm{kHz}}\right),$$

where $\dot{q}_J$ is the local change of kinetic energy density resulting from Joule heating. Averaging the Joule heating over the plasma gives:

$$\begin{aligned}\dot{Q}_J &= 2\pi L_p \int \dot{q}_J r\,dr \\ &\approx (8.6\times10^{-4}\mathrm{eV/s})\left(\frac{f_E}{1\,\mathrm{kHz}}\right)\left(\frac{B}{1\,\mathrm{T}}\right)^{-1}\left(\frac{L_p}{10\,\mathrm{cm}}\right)^{2} N_{tot}\,,\end{aligned} \tag{4.20}$$

where $\dot{Q}_J$ is the total Joule heating of the plasma.

Neutral Heating Rate

Collisions between ions and neutrals can result in plasma heating or cooling. Typically, the experiments discussed here operate in a vacuum of $P_N \simeq 4\times10^{-9}$ Torr. This corresponds to a neutral density of $n_N \simeq 1.3\times10^{8}$ cm^{-3}, which is comparable to the plasma densities under consideration. Also, the masses of the neutral particles (dominantly hydrogen H_2) have a mass which is comparable to the ions, so it is not unreasonable to expect significant cooling or heating to result from ion-neutral collisions. For typical operating parameters, the neutral atoms have a mean free path which is large compared with the trap dimensions, so the neutrals bounce off the trap walls many times before colliding with an ion. The neutrals can therefore be expected to be in thermal equilibrium with the room-temperature trap walls, i.e. $T_N \simeq 0.026$ eV.

The heating rate $\partial T/\partial t$ of an ion plasma immersed in a bath of neutrals at temperature T_N is estimated in Equation C.12 of Appendix C. The resulting rate of change of the plasma kinetic energy density q is:

$$\begin{aligned}\dot{q}_N &\simeq -\frac{15}{2}\pi n n_N e\sqrt{\alpha/\mu}\,\frac{m m_N}{(m+m_N)^2}(T-T_{N,eff}) \\ &\approx -\left(8.8\times10^{4}\,\mathrm{cm^{-3}s^{-1}}\right)(T-T_{N,eff})\left(\frac{P_N}{10^{-9}\,\mathrm{Torr}}\right)\left(\frac{n}{10^7\,\mathrm{cm^{-3}}}\right),\end{aligned} \tag{4.21}$$

where $T_{N,eff} \approx T_N$ is given by Equation C.13. Equation 4.21 can be integrated over the plasma to give the average expected total heating rate resulting from ion-neutral collisions:

$$\begin{aligned} \dot{Q}_N &= 2\pi L_p \int \dot{q}_N r dr \\ &\approx \left(8.8 \times 10^{-3}\mathrm{s}^{-1}\right)(T - T_N)\left(\frac{P_N}{10^{-9}\ \mathrm{Torr}}\right) N_{tot}\ . \end{aligned} \tag{4.22}$$

Measurement of Background Heating Terms

The background heat sources are measured by uniformly heating or cooling the plasma with a manipulating beam, then measuring the subsequent temperature evolution after the cooling beam is turned off. Here, we use a wide manipulating beam which is shone through the ion plasma at an angle (see Figure 2.2) so most of the ions in the cloud rotate through the beam. This allows an initial condition to be created where the temperature is flat as a function of radius. The time-evolution of this initial condition is then measured after blocking the manipulating beam.

A typical external heating measurement is shown in Figure 4.11. Here, a length $L_p \simeq 13.5$ cm plasma in a vacuum of $P_N \simeq 4 \times 10^{-9}$ Torr is initially held in steady-state at $n \simeq 5.4 \times 10^7\ \mathrm{cm}^{-3}$ through application of a $f_s = 20$ kHz, $A_s = 0.5$ V, $m_\theta = +1$ rotating wall field. The plasma is uniformly cooled to a steady-state initial temperature of $T(r, t = 0) \simeq 3 \times 10^{-3}$ eV with a wide, angled manipulating beam.

The rate of change of temperature of Figure 4.11 gives the background heating terms $\dot{q}_{ext}$, since we expect radial heat flow to be small in the absence of temperature gradients; that is, $\Gamma_q = 0$ in Equation 4.6, so $\dot{q} = \dot{q}_{ext}$. Our model for $\dot{q}_{ext}$ is $\dot{q}_{ext} = \dot{q}_J + \dot{q}_N$ where $\dot{q}_J$ is estimated in Equation 4.19 and $\dot{q}_N$ is estimated in Equation 4.21. Our model for the total heating rate $\dot{Q}$ is given by $\dot{Q} = \dot{Q}_J + \dot{Q}_N$, where $\dot{Q}_J$ is estimated in Equation 4.20 and $\dot{Q}_N$ is estimated in Equation 4.22.

The measured heating $\dot{q}$ at $t = 0.15$ sec of Figure 4.11(b) is plotted in Fig-

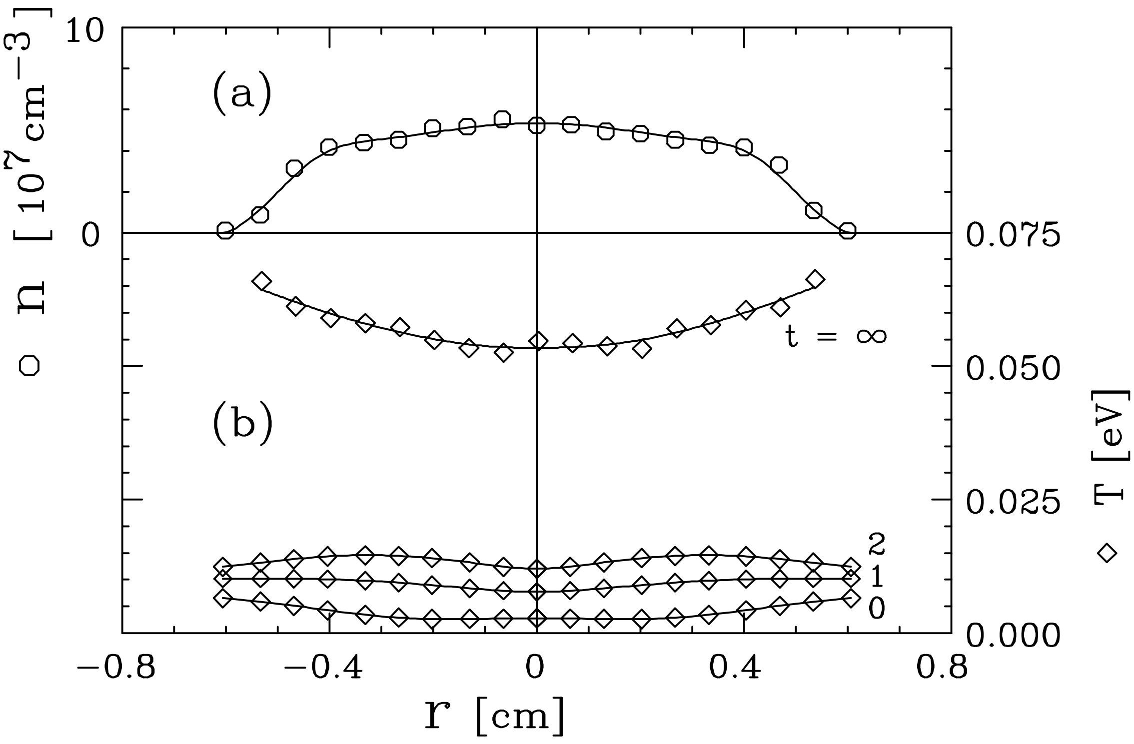

Figure 4.11: Measured plasma heating starting from uniformly cooled initial condition. Data points at $t = 0$, 1, and 2 are smoothed radially; data at $t = \infty$ is unsmoothed and shows the characteristic level of scatter in the data.

ure 4.12(b). The measured heating is slightly larger at the edges of the plasma than on center. The dashed curve of Figure 4.12 is the external heating expected from the model $\dot{q}_{ext} = \dot{q}_J + \dot{q}_N$, giving $\dot{q}_{ext} \simeq (10^5\,\mathrm{eVcm^{-3}s})\left[5.4\,(r/1\,\mathrm{cm})^2 + 0.1\right]$ $(n/10^7\,\mathrm{cm^{-3}})$. It can be seen that the model is smaller than the data; typically, we find rough qualitative agreement (i.e. within about a factor of two) between this model and measurements.

It is interesting to note that the uniformly-cooled data of Figure 4.11 corresponds to the same central ($r = 0$) initial condition ($n \simeq 5 \times 10^7\,\mathrm{cm^{-3}}$, $T \simeq 3 \times 10^{-3}$ eV) as the strong-gradient data of Figure 4.5. However, the measured initial ($t = 0.1$ sec) heating of Figure 4.11 ($\dot{q} \simeq 4 \times 10^5\,\mathrm{eVcm^{-3}s^{-1}}$) is about 10 times smaller that the measured initial ($t = 0.1$ sec) heating of Figure 4.5 ($\dot{q} \simeq 5 \times 10^6\,\mathrm{eVcm^{-3}s^{-1}}$).

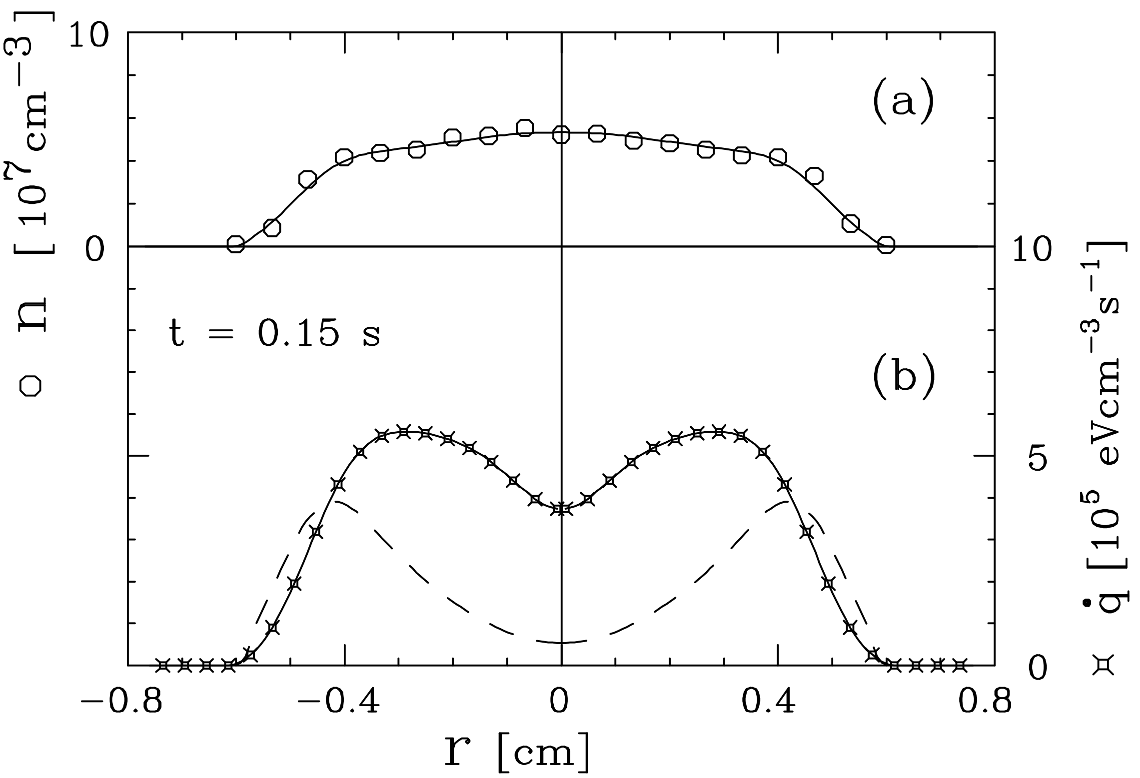

Figure 4.12: Measured heating rate $\dot{q}$ for uniformly-cooled initial condition.

Thus, the we have a clear signature of radial heat flow in the data of Figure 4.5.

Experiments similar to the one described above were performed on plasmas at neutral pressures $P_N \simeq 3 \times 10^{-10}$ and 4×10^{-9} Torr, densities $10^7 < n < 10^8$ cm^{-3}, and temperatures $10^{-3} < T < 2$ eV. Typically, we find that the heating/cooling as a function of radius is relatively flat, as in Figure 4.12. Typically, we find that the magnitude of the predicted heating $\dot{Q}_J + \dot{Q}_N$ is within a factor of 2 of the measured total heating $\dot{Q} \equiv 2\pi L_p \int \dot{q} r dr$. On average, we obtain $\left|(\dot{Q}_J + \dot{Q}_N)/\dot{Q}\right| \simeq 1.3$, so the model predicts an average total heating magnitude which is about 30% larger than the data.

Chapter 5

Measurement of Cross-Field Test Particle Transport

5.1 Overview

Cross-field test particle transport refers to the internal transport of particles across the magnetic field. Even in an ideal trap with no bulk plasma expansion, collisions between the charges will cause a continuous cross-field diffusion of individual charges. That is, the local density of test particles $n_t(r)$ can change as a function of time even though the total density $n(r)$ remains constant. In Chapter 4, it was demonstrated that long-range collisions with impact parameter $\rho \lesssim \lambda_D$ dominate the internal transport of heat across the magnetic field. We find here that these long-range collisions also give enhanced test particle transport. The measured test particle diffusion obeys the same density, temperature, and magnetic field scaling as predicted by the classical theory; but is larger by about an order of magnitude, consistent with the theory prediction for long-range plus short-range collisions.

The classical theory of test particle transport was derived for neutral plasmas with $r_c > \lambda_D$. It was presumed that the transport results from steps of the particle guiding-centers by a distance of order r_c as a result of short-range velocity-scattering collisions with impact parameter $\rho \leq r_c$. Thus, we expect a classical diffusion coefficient $D_c \sim (n\bar{v}b^2)r_c^2$. A more rigorous analysis gives a classical diffusion coefficient of [39, 58]:

$$\begin{aligned} D_c &= \frac{5}{4}\nu_{ii} r_c^2 \\ &\approx \left(3.1\times10^{-3}\,\mathrm{cm^2s^{-1}}\right)\left(\frac{T}{1\,\mathrm{eV}}\right)^{-1/2}\left(\frac{B}{1\,\mathrm{T}}\right)^{-2}\left(\frac{n}{10^7\,\mathrm{cm^{-3}}}\right) \\ &\times \left\{1+0.08\ln\left[\left(\frac{T}{1\,\mathrm{eV}}\right)^{3/2}\left(\frac{B}{1\,\mathrm{T}}\right)^{-1}\right]\right\}, \end{aligned} \tag{5.1}$$

where ν_{ii} is the "momentum transfer" rate resulting from ion-ion collisions (Equation 4.1).

If the Debye shielding length is sufficiently large, i.e. $\lambda_D > r_c$, then the particles can also interact via long-range collisions with impact parameter $r_c < \rho \leq \lambda_D$. The cross-field particle diffusion resulting from these collisions can be estimated as follows: two guiding centers separated by a distance of order λ_D will $\mathbf{E}\times\mathbf{B}$ drift in each others' electric fields, resulting in a cross-field step $\Delta r \sim cE\Delta t/B$, where Δt is the interaction time. The collision frequency of these collisions is expected to be of order $nv\lambda_D^2$. Using the estimates $E \sim e/\lambda_D^2$ and $\Delta t \sim \lambda_D/v$, one then obtains $\Delta r \sim b(r_c/\lambda_D)$, and an estimated diffusion coefficient due to long-range collisions $D_L \sim nv\lambda_D^2\Delta r^2 \sim nvb^2r_c^2$. Thus, the diffusion coefficient due to long-range collisions is expected to have the same scaling as the classical coefficient D_c [38]. A more detailed calculation of the long-range diffusion coefficient gives [19]:

$$\begin{aligned} D_L &= 6\sqrt{\pi}\left(nvb^2\right) r_c^2 \ln(\lambda_D/r_c)\ln\left[v/\left(\nu_{ii}v^2\sqrt{\lambda_D r_c}\right)^{1/3}\right] \\ &\approx \left(8.6\times10^{-3}\,\mathrm{cm^2s^{-1}}\right)\left(\frac{T}{1\,\mathrm{eV}}\right)^{-1/2}\left(\frac{B}{1\,\mathrm{T}}\right)^{-2}\left(\frac{n}{10^7\,\mathrm{cm^{-3}}}\right) \\ &\times \left\{1+0.6\ln\left[\left(\frac{n}{10^7\,\mathrm{cm^{-3}}}\right)^{-1/2}\left(\frac{B}{1\,\mathrm{T}}\right)\right]\right\}. \end{aligned} \tag{5.2}$$

It is interesting to note that the diffusion coefficient D_L in Equation 5.2 contains a factor three enhancement because of the effectively one-dimensional nature of the collisional dynamics: velocity diffusion caused by collisions with surrounding particles can reverse a particle's axial velocity and lead to multiple collisions between the same pair of particles. This "velocity caging" is a novel effect in kinetic theory: it is present even in the limit of weak one-dimensional collisions, yet it cannot be obtained using the traditional approach of integration along unperturbed orbits.

Test particle transport measurements require that a group of particles be made distinguishable from the other particles in the plasma. We accomplish this "tagging" of the test particles by uniformly spin-polarizing a Mg^+ ion plasma relative to the magnetic field $\mathbf{B}$ and then reverse spin-polarizing a small sample of ions. The LIF diagnostic allows the selective measurement of the tagged ions, so that their diffusion into the bulk of the plasma can be observed. The results of these measurements are presented in Section 5.2.

As in the heat transport measurements, small source terms can affect these experiments. Here, test particle "sources" result from collisions, which can cause spin depolarization. The corrections used to account for this effect are discussed in Section 5.3.

5.2 Test Particle Transport Results

To measure test particle transport in Mg^+ plasmas, optical pumping transitions are used to spin-state "tag" a cylindrical shell at some radius r_t; the radial diffusion of this cylindrical shell is then monitored at each radius r using a cyclic transition, as described in Section 2.5.2 (see Figure 2.8).

A typical test particle transport experiment [3, 2] is shown in Figure 5.1. Here, test particle diffusion is measured for a plasma with density $n \simeq 7 \times 10^6$ cm^{-3}, temperature $T \simeq 0.2$ eV, and magnetic field strength $B = 4$ T. Initially, the entire plasma is spin-polarized into the -1/2 ground state. Then, more than 80% of the ions are locally pumped into the +1/2 state at radius $r_t = 0.5$ cm; the rest of the plasma remains in the -1/2 state. The time-evolution of the test particles is

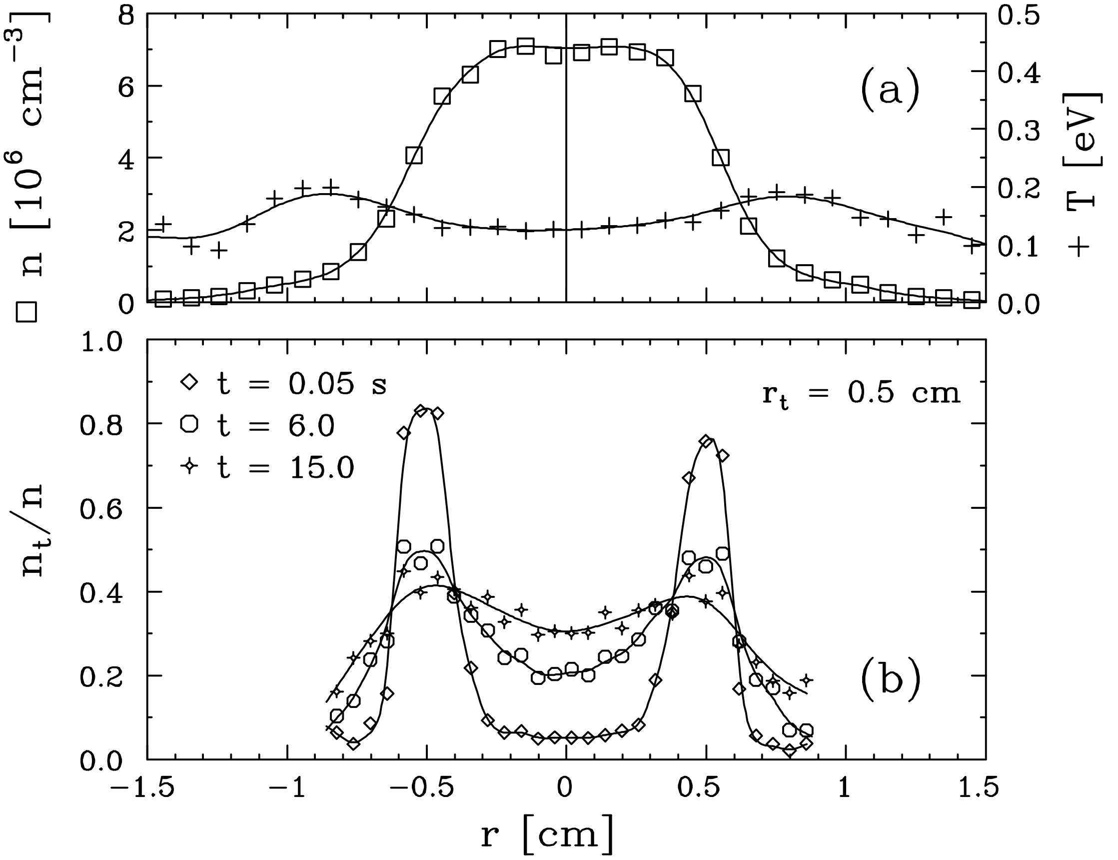

Figure 5.1: Measured radial diffusion of test particle density n_t toward $n_t/n = const.$

measured at 29 radial positions from $r = -0.85$ to $r = 0.85$ cm and at 15 time steps from $t = 0.05$ to $t \simeq 15$ sec; in Figure 5.1(b), $n_t(r,t)$ is shown only at time steps $t = 0.05$, 6, and 15 seconds. Also shown in Figure 5.1(a) are the total ion density $n(r)$ and temperature $T(r)$; these quantities are constant since the plasma is generally kept in a steady-state equilibrium by applying a rotating wall field, as described in Chapter 3.

The evolution of test particles $n_t(r,t)$ of Figure 5.1 results from radial diffusion of test particles as well as from local sources (or sinks) of test particles. In these experiments, spontaneous spin flip is the dominant source of test particles. As will be shown in Section 5.3, sideband optical pumping from the probe beam can be neglected for these experiments, and the local spontaneous spin flip rate $\nu_{sf}(r)$ can be obtained from independent measurements. The measured flux of test particles Γ_t is then:

$$\Gamma_t(r,t) = -\frac{1}{r}\int_0^r dr'r'\left\{\frac{\partial n_t(r',t)}{\partial t} - \nu_{sf}(r')\left[\frac{n(r')}{2} - n_t(r',t))\right]\right\} . \tag{5.3}$$

Here, $\partial n_t(r,t)/\partial t$ is the time derivative of the measured test particle evolution $n_t(r,t)$ and $\nu_{sf}(r)[n(r)/2 - n_t(r,t)]$ is the expected contribution to $\partial n_t(r,t)/\partial t$ from spontaneous spin depolarization, described in Section 5.3.

The test particle flux Γ_t is expected to have a form:

$$\Gamma_t(r,t) = -D(r)n(r)\nabla\left(\frac{n_t(r,t)}{n(r)}\right) + V_r(r)n_t(r,t) , \tag{5.4}$$

where $D(r)$ is the measured test particle diffusion coefficient, V_r represents a possible radial convective velocity, and $\nabla \equiv \partial/\partial r$. The test particle diffusion of Equation 5.4 is driven by gradients in the relative concentration of test particles n_t/n. The test particle flux will thus drive the test particle radial distribution toward an equilibrium where the concentration of test particles relative to total particles is a constant, that is, $n_t(r)/n(r) = const.$ This form of the diffusion term can be obtained from a two-species particle diffusion calculation [39]. It is important to note that Equation 5.4 describes diffusion in which the test particles diffuse radially as a result of collisions with either test particles or normal particles; tagged particles and untagged particles are indistinguishable as far as the diffusion process is concerned. The analysis is therefore valid for arbitrary relative concentrations n_t/n; a small relative concentration $n_t/n \ll 1$ is not required for these measurements.

We find that the test particle flux is diffusive in nature. This can be seen qualitatively in Figure 5.2, where the measured test particle flux Γ_t is plotted as a function of radius at $t = 3$ sec for the experiment shown in Figure 5.1. Also plotted is the expected driving term for test particle diffusion, $-n(r)\nabla\left[n_t(r)/n(r)\right]$. It can be seen that $\Gamma_t \propto -n(r)\nabla\left[n_t(r)/n(r)\right]$, consistent with Equation 5.4 with $D(r) \simeq const.$ and $V(r) \simeq 0$.

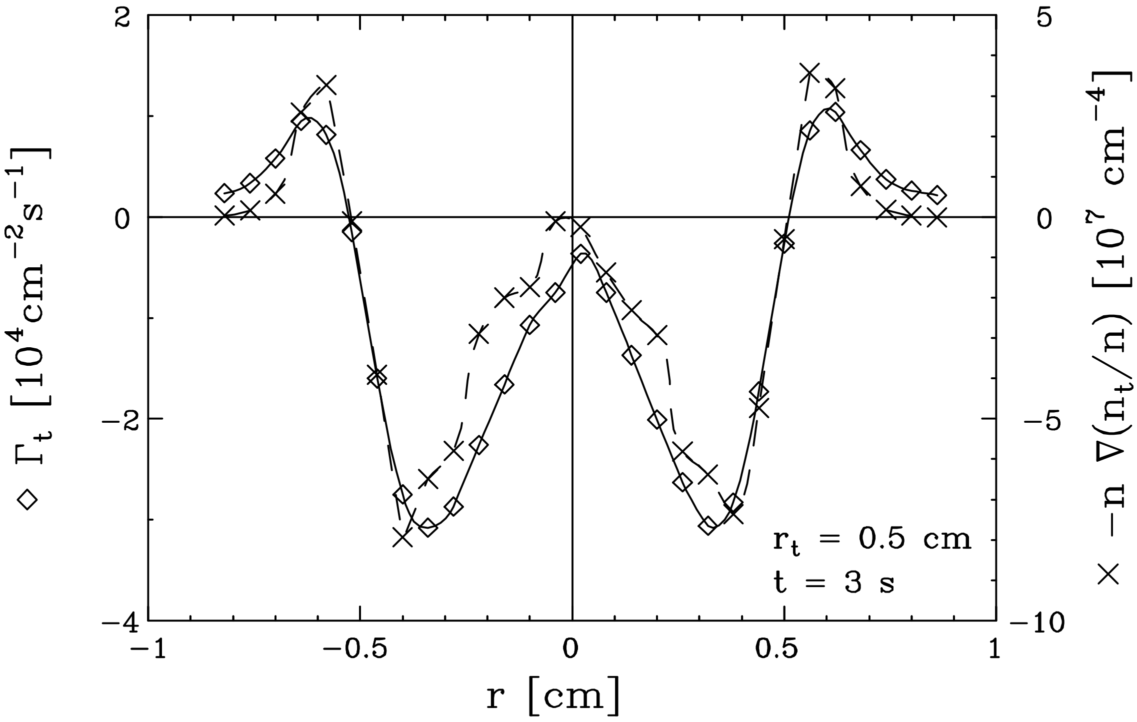

Figure 5.2: Radial test particle flux Γ_t and test particle concentration gradient $\nabla(n_t/n)$ as a function of radius, showing flux proportional to gradient.

This "Fick's Law" proportionality between flux and gradient is also found to apply as a function of time. This is shown in Figure 5.3, where the test particle flux Γ_t is plotted as a function of the gradient $n(r)\nabla\left[n_t(r)/n(r)\right]$ at radius $r = 0.32$ cm; here, the different points represent different time steps in the evolution. The solid line is a fit to the data; it can be seen that the expected proportionality $\Gamma_t \propto -n(r)\nabla\left[n_t(r)/n(r)\right]$ is well-satisfied. The slope of the line gives a measured diffusion coefficient $D(r) = 3.3 \times 10^{-3}\,\mathrm{cm}^2/\mathrm{sec}$.

A nonzero radial convective velocity $V_r(r)$ would be expected to manifest itself as a vertical offset in the fit through the data in Figure 5.3. Here, we obtain a negligible y-axis intercept $V_r(r) = -1.4 \times 10^{-4}$ cm/s. In general, we find $V_r(r) \simeq 0$ within experimental accuracy. One might expect a nonzero V_r as a result of slow azimuthally-asymmetric convection cells or from incorrect removal of source terms.

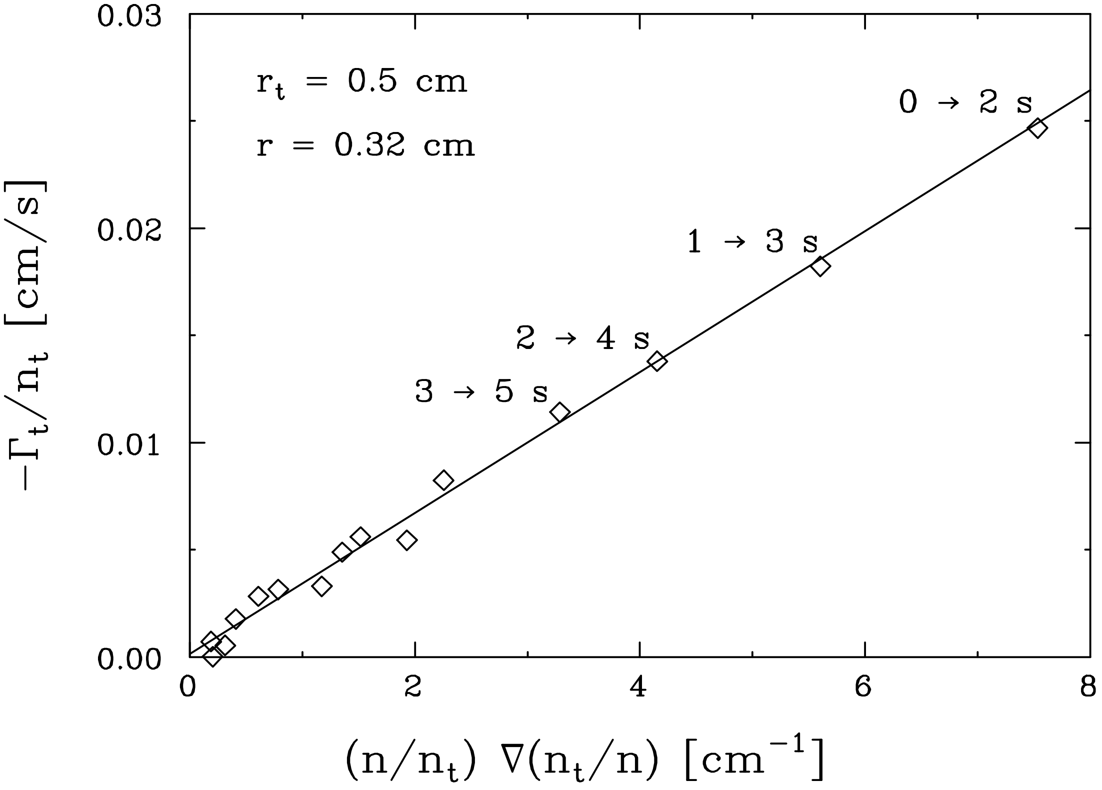

Figure 5.3: Test particle flux Γ_t as a function of test particle concentration gradient $\nabla(n_t/n)$, demonstrating flux proportional to gradient.

These results indicate that plasma convection is not a significant source of cross-field particle transport in these plasmas.

Test particle transport measurements were performed on plasmas with densities $10^6 < n < 4 \times 10^7\,\mathrm{cm}^{-3}$, temperatures $0.05 < T < 3$ eV, and magnetic fields $0.8 < B < 4$ T. The background neutral pressure was $P_N \simeq 4 \times 10^{-9}$ Torr. Temperatures higher than 0.05 eV were obtained by using either an $m_\theta = 1$ drive to launch cyclotron modes (ion cyclotron resonance heating) or by using an $m_\theta = 0$ drive to launch plasma modes in the system; both heating methods were used in the data presented here with no noticeable difference in the results.

The measured test particle diffusion coefficient D is displayed in Figure 5.4 as a function of temperature T. The measured D is divided by $n_7 B^{-2} \ln(\lambda_D/r_c)$

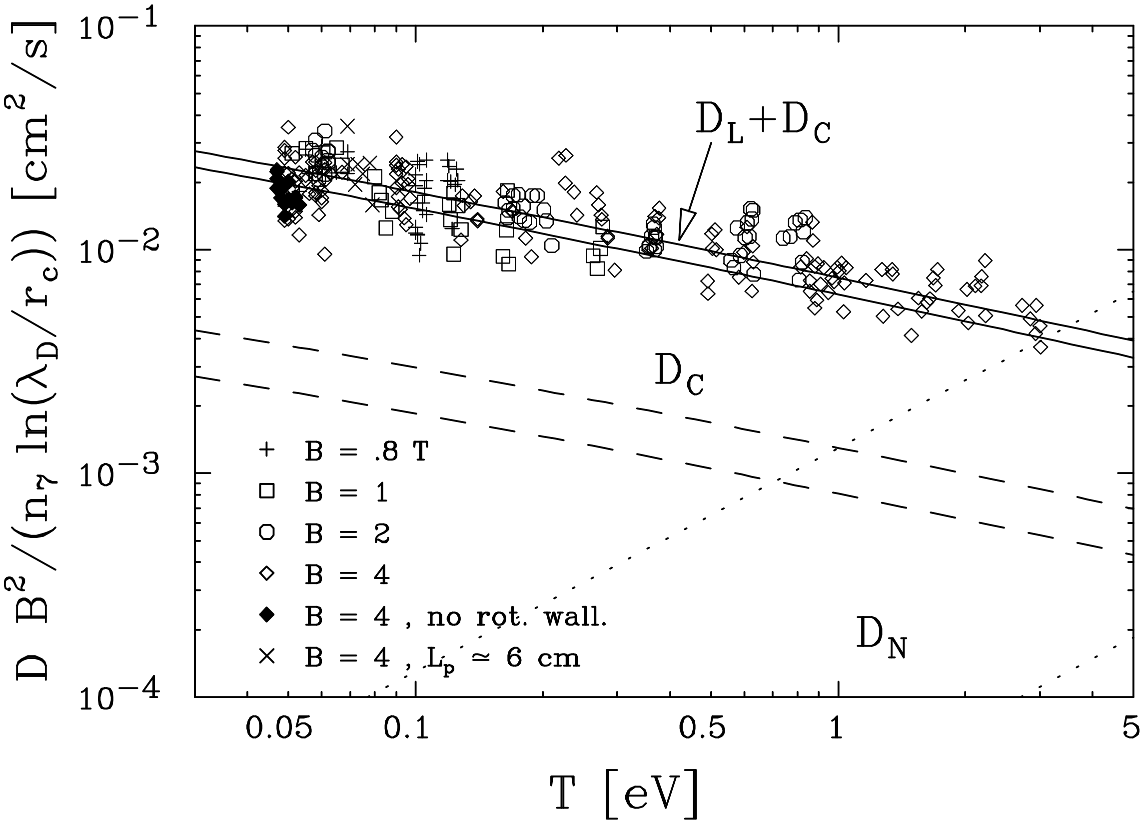

Figure 5.4: Measured test particle diffusion coefficient D as a function of temperature T.

(with B in Tesla), since this is the expected dominant density and magnetic field dependence of the long-range theory (Equation 5.2). This enables the entire range of B and n covered in the experiments to be displayed. In Figure 5.4, each point corresponds to a diffusion coefficient obtained at a single radius using a linear fit as a function of time as described above; several values of D are therefore obtained for each transport experiment.

It can be seen that the data is about ten times larger than expected for classical test particle diffusion D_c alone (dashed curves), but is in excellent agreement with the predictions of classical diffusion plus diffusion due to long-range collisions, $D_c + D_L$ (solid curves). The range of the curves is due to the $\ln(\lambda_D/r_c)$ normalization, which is not contained in the classical diffusion coefficient D_c of Equation 5.1.

It is expected that collisions with the background neutral gas will also cause radial diffusion of the ions; however, this is negligible for the data presented here. We can approximate the diffusion coefficient resulting from ion-neutral collisions as $D_N \simeq \nu_{iN} r_c^2$. Here, we use Equation C.3 of Appendix C to estimate ν_{iN}. The resulting ion-neutral collisional diffusion D_N is:

$$\begin{aligned} D_N &\simeq \nu_{iN} r_c^2 \simeq 2\pi n_N e\sqrt{\alpha/\mu} \\ &\approx (8.3 \times 10^{-5}\,\mathrm{cm^2 s^{-1}}) \left(\frac{B}{1\,\mathrm{T}}\right)^{-2} \left(\frac{P_N}{10^{-9}\,\mathrm{Torr}}\right) \left(\frac{T}{1\,\mathrm{eV}}\right) . \end{aligned} \tag{5.5}$$

This estimate for D_N is plotted in Figure 5.4 as the pair of dotted curves. It can be seen that the expected contribution from ion-neutral collisions is much too small to describe the observed diffusion. Also, D_N has a different temperature scaling than the observed diffusion and does not depend on ion density.

Similarly, the effect of the rotating wall drive used to hold the plasma in steady-state during these experiments is not responsible for the observed enhanced transport. The rotating wall drive counteracts the slow bulk plasma expansion which occurs on a time scale of $\tau_m \sim 1000$ sec. This is much slower than 10 sec, the time scale on which the test particles are typically observed to diffuse across the plasma. To verify this, the solid symbols of Figure 5.4 were measured at $T \simeq 0.05\,\mathrm{eV}$ with the rotating wall turned off during the test particle diffusion measurement; it can be seen that the absence of the rotating wall field does not affect the diffusion rate.

The 2-D bounce-averaged contribution to the test particle diffusion (from the last row of Table 4.1) is believed to be negligible here. This is verified experimentally by measuring the test particle diffusion for short ($L_p \simeq 6\,\mathrm{cm}$) ion plasmas. As seen in Figure 5.4, the observed diffusion in these short plasmas did not differ noticeably from that of the longer ($L_p \simeq 12\,\mathrm{cm}$) plasmas.

In conclusion, measurements of test particle transport in magnesium plasmas have been performed over a range of 50 in temperature, 40 in density, and 5 in magnetic field. The measured diffusion coefficients are about ten times greater than predicted by classical theory alone, but agree closely with the prediction for both long-range collisions and classical, short-range collisions. These results, together with the heat transport measurements of the previous chapter, provide an incisive demonstration of long-range collisional transport in these plasmas. Also, the test particle transport measurements provide support for a novel effect in kinetic theory, "velocity caging", which provides a factor of three enhancement in the particle diffusion rate for one-dimensional $\mathbf{E} \times \mathbf{B}$ collisions [19].

5.3 Background Corrections

The two background terms which can affect the test particle transport measurements are sideband optical pumping from the diagnostic beam and collisional depolarization of the spin-tagged ions, or "spontaneous spin-flip". We will show in this section that the sideband pumping can be made negligibly small by operating the diagnostic beam at low power and low duty cycle. The spontaneous spin flip is shown to be a small correction which can be measured and subtracted off from the test particle transport measurements.

A typical measurement of these background corrections is shown in Figure 5.5 for an ion plasma with central density $n_0 = 6.5 \times 10^7\,\mathrm{cm}^{-3}$ and temperature $T = 0.25$ eV. Here, the entire ion cloud is spin-polarized into the $m_j = -1/2$ state by 10 seconds of illumination with a perpendicular beam passing through $r = 0$. This polarizing beam is tuned to the peak of an optical pumping transition. The population of the $m_j = +1/2$ state is then probed by using a diagnostic beam passing through $r = 0$ parallel to $\mathbf{B}$ and tuned to the peak of a cyclic transition. This diagnostic beam is blocked most of the time with a shutter. Every 2 seconds, the shutter is opened for 40 ms and the resulting photon count rate is measured. This count

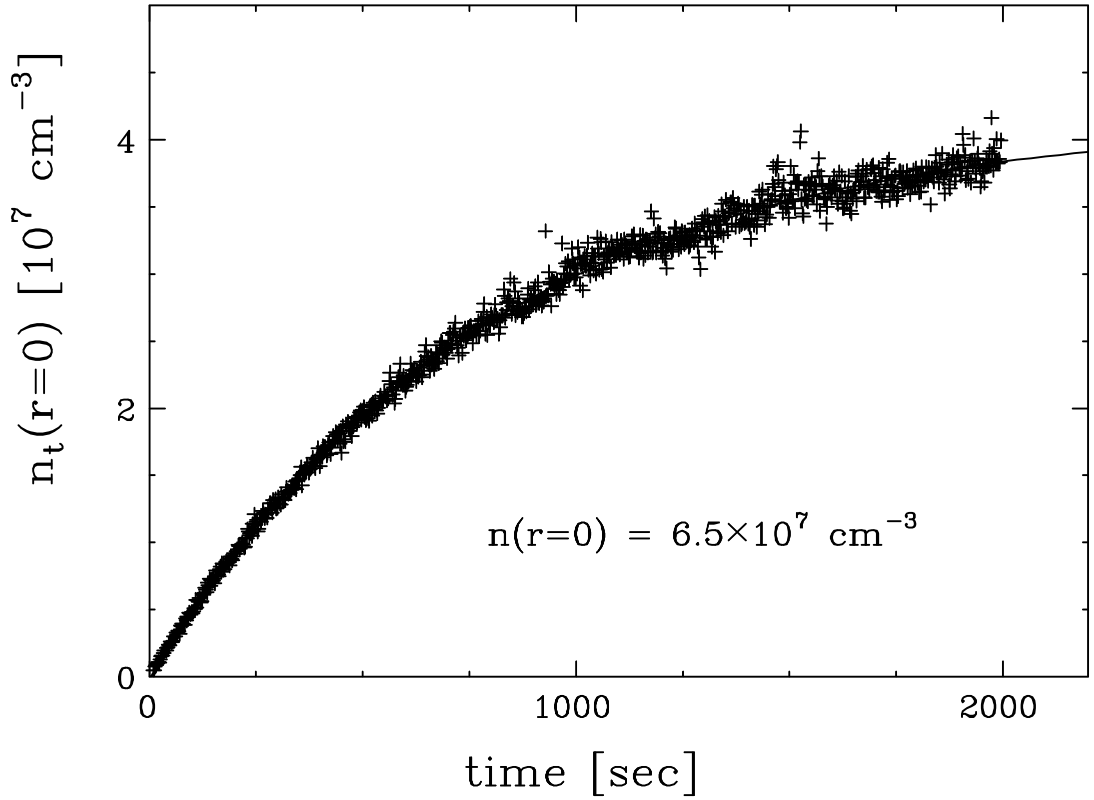

Figure 5.5: Measurement of the central density of ions in the $m_j = +1/2$ state, $n_t(r = 0, t)$, starting with a plasma completely spin polarized into the $m_j = -1/2$ state.

rate gives $n_t(0, t)$, the density of magnesium ions in the $+1/2$ state at $r = 0$. The plasma temperature is known and is constant during this measurement. The diagnostic beam power for this experiment was $I_0 \simeq 0.29$ mW, so the average diagnostic beam power was only $\langle I_0 \rangle = I_0\,(.04/2) = 5.8 \times 10^{-3}$ mW.

The time evolution $n_t(0, t)$ measured in Figure 5.5 can be used to obtain the sideband optical pumping rate ν_{op} and the spontaneous spin-flip rate ν_{sf}. Both rates can be obtained from a single measurement, since the optical pumping will tend to drive the all the ions into the $+1/2$ state, while the spontaneous spin-flip would asymptote to a final equilibrium with only half the ions in the $+1/2$ state. The time evolution of $n_t(r,t)$ can thus be written as:

$$\frac{\partial}{\partial t} n_t(r,t) = \nu_{op}\left[n(r) - n_t(r,t)\right] + \nu_{sf}\left[\frac{n(r)}{2} - n_t(r,t)\right] . \tag{5.6}$$

Note that the total particle density $n(r)$ is not a function of time. We expect the rates in Equation 5.6 to be slow compared with the rate at which ions diffuse across the field lines, so the fractional polarization will be uniform across the plasma, i.e. $n_t(r,t)/n(r) \simeq const.$ Also, it is reasonable to expect that the spin-flip rate will be proportional to the ion density, $\nu_{sf}(r) \propto n(r)$. Averaging Equation 5.6 over the entire plasma and using the initial condition $n_t(r, t=0) = 0$ then gives:

$$n_t(r=0,t) = n_{final}\left(1 - e^{-t/\tau_t}\right) + n_{back} , \tag{5.7}$$

where $\tau_t \equiv 1/(\nu_{op}+\nu_{sf})$, $n_{final} \equiv n_0(\nu_{op}+\nu_{sf}/2)/(\nu_{op}+\nu_{sf})$, $\nu_{sf} \equiv \nu_{sf}(r)n/n(r)$, and $n \equiv \int n^2\, rdr/\int n\, rdr$. n_{back} allows for an offset in the measured signal; this can occur as a result of background scattering of photons or from amplifier offsets. The solid line in Figure 5.5 is a fit to the data of the form of Equation 5.7 with the adjustable parameters $n_{final} = 4.18 \times 10^7\,\mathrm{cm}^{-3}$, $\tau_t = 786$ sec, and $n_{back} = -1.6 \times 10^5\,\mathrm{cm}^{-3}$. It can be seen that this functional form provides an excellent fit to the measured signal. The optical pumping rate ν_{op} and average spin flip rate ν_{sf} are then obtained from the fit parameters: $\nu_{op} = (2\,n_{final}/n_0 - 1)/\tau_t \simeq 3.7 \times 10^{-4}\,\mathrm{s}^{-1}$ and $\nu_{sf} = 2\,(1 - n_{final}/n_0)/\tau_t \simeq 9.0 \times 10^{-4}\,\mathrm{s}^{-1}$.

The measurement method demonstrated by Figure 5.5 was used to measure the sideband pumping rate and spontaneous spin-flip rate as a function of average diagnostic beam power $\langle I_0\rangle$, plasma temperature T, and plasma density n. These results are described in Subsections 5.3.1 and 5.3.2. It is found that sideband optical pumping is negligible and that spontaneous spin flip is a small correction for the test particle transport data presented in Section 5.1

5.3.1 Sideband Optical Pumping

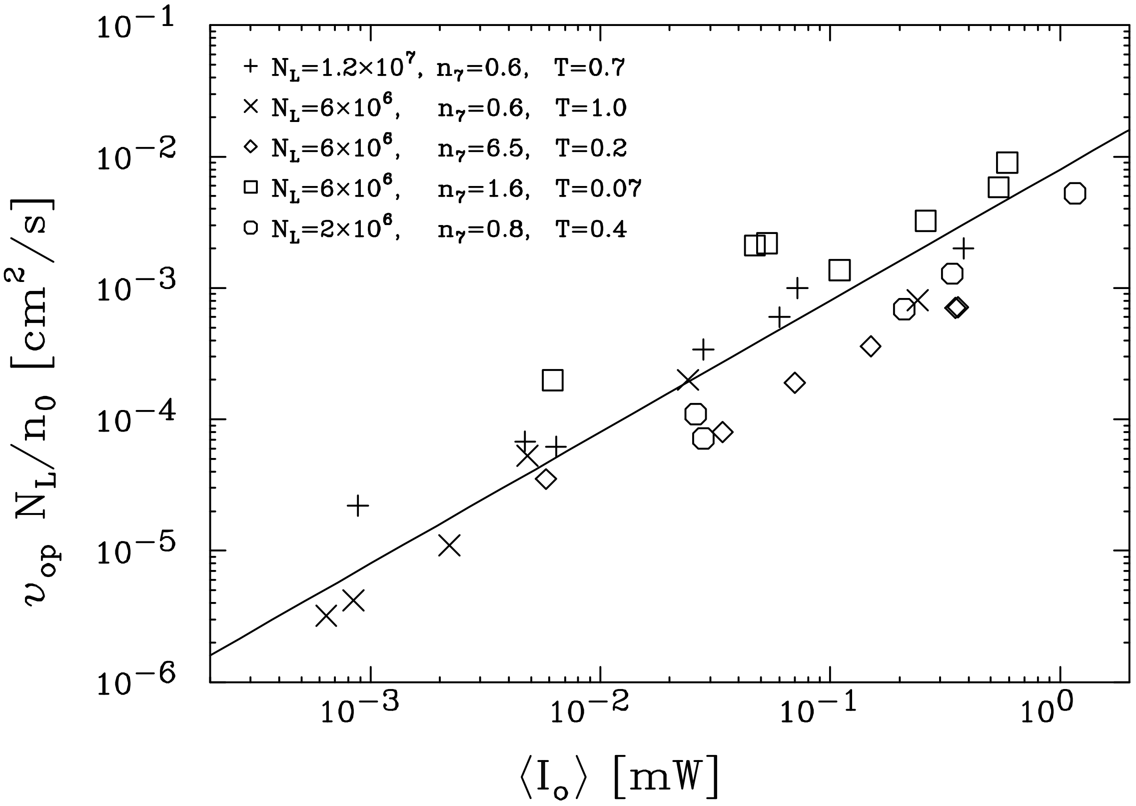

Figure 5.6: Measured sideband optical pumping rate ν_{op} as a function of average UV power $\langle I_0 \rangle$.

For the range of UV power I_0 used here, we expect the sideband pumping rate to be linear in UV power. Additionally, the sideband pumping rate should be proportional to the number of ions illuminated by the beam divided by the total number of ions in the cloud (assuming fast radial mixing). For a parallel diagnostic beam at $r = 0$, the number of ions illuminated goes like the central density n_0 times the plasma length L_p, so we expect $\nu_{op} \propto \langle I_0 \rangle n_0 L_p / N_{tot} = \langle I_0 \rangle n_0 / N_L$, where N_L is the mean line charge density. We do not expect a strong temperature dependence for typical operating conditions, since the frequency shift between the cyclic and optical pumping transitions is large compared to the average Doppler shift in the transitions: $\Delta\nu \equiv \sqrt{2}\,\nu_0(v/c) \simeq (10.1\text{ GHz})\,(T/1\,\text{eV})^{1/2} < \delta\nu_{op} \simeq 37.4\text{ GHz}\,(B/4\,\text{T})$.

Figure 5.6 shows the measured sideband optical pumping rate ν_{op} as a function of averaged diagnostic beam power $\langle I_0 \rangle$. The sideband pumping rate is displayed multiplied by N_L/n_0 for each data set to remove this anticipated dependence from the data. The data was taken at magnetic field strength $B = 4$ T and covers a central density range $6 \times 10^6 \le n \le 6.5 \times 10^7\,\mathrm{cm}^{-3}$, a line density range $0.2 \times 10^7 \le N_L \le 1.2 \times 10^7\,\mathrm{cm}^{-1}$, and a temperature range $0.07 \le T \le 1.0$ eV. The data can be reasonably well-fit by a straight line, corresponding to:

$$\nu_{op} = (8 \times 10^{-3}\mathrm{s}^{-1}) \left(\frac{n}{10^7\,\mathrm{cm}^{-3}}\right) \left(\frac{N_L}{10^7\,\mathrm{cm}^{-1}}\right)^{-1} \left(\frac{\langle I_0 \rangle}{1\,\mathrm{mW}}\right) . \tag{5.8}$$

Our test particle transport experiments are performed with a low average search beam power $\langle I_0 \rangle$, so sideband pumping can in general be neglected. For the experiment shown in Figure 5.1, for example, the probe beam was used at power $I_0 \simeq 0.5$ mW and at a duty cycle $(0.04\,\mathrm{sec}/0.5\,\mathrm{sec}) \simeq 8 \times 10^{-2}$, corresponding to an average power $\langle I_0 \rangle \simeq 4 \times 10^{-2}$ mW. Using the line-charge density $N_L \simeq 2 \times 10^7\ \mathrm{cm}^{-1}$ and density $n_0 \simeq 6 \times 10^6\,\mathrm{cm}^{-3}$, the sideband optical pumping rate estimated from Equation 5.8 is $\nu_{op} \simeq 10^{-4}\,\mathrm{sec}^{-1}$. The sideband pumping thus causes n_t to evolve on a time scale of about 10^4 seconds, which is clearly negligible compared to the 1 to 30 second time scale for particle diffusion.

5.3.2 Spontaneous Spin Flip

The plasma-averaged spontaneous spin-flip rate ν_{sf} was measured at magnetic field strength $B = 4$ T, neutral pressures $P_N = 7 \times 10^{-11}$ and 4×10^{-9} Torr, temperatures $T = .06$ to 4.4 eV, and average ion densities $n = 10^6$ to $10^8\,\mathrm{cm}^{-3}$. In Figure 5.7, the measured spin-flip rate is plotted as a function of the plasma temperature at neutral pressures $P_N = 7 \times 10^{-11}$ and 4×10^{-9} Torr and at an average ion density ranging from $n = 3 \times 10^6$ to $11 \times 10^6\,\mathrm{cm}^{-3}$. It can be seen that the spin-flip rate rises strongly with increasing temperature for the low neutral pressure data. For the high neutral pressure data, the temperature dependence is not as pronounced;

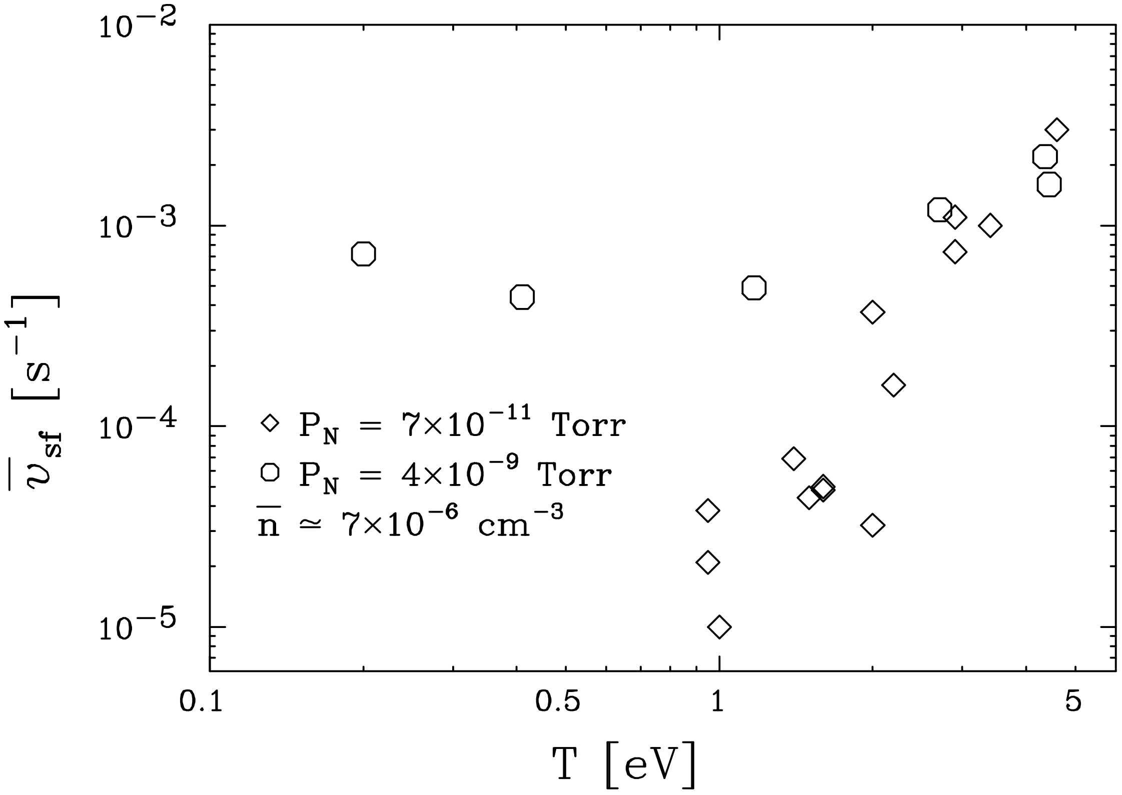

Figure 5.7: Spontaneous spin-flip rate measured as a function of temperature, showing strong temperature dependence at low neutral pressure and weak temperature dependence at high neutral pressure.

the spin-flip rate appears to be almost independent of temperature.

In Figure 5.8, the measured spin-flip rate ν_{sf} is plotted as a function of average density n for plasmas at temperatures $T \simeq 1.8$ to 2 eV at a neutral pressure of $P_N = 7 \times 10^{-11}$ Torr. Here, the spin-flip rate appears to be essentially linear in the average plasma density n. Also, ν_{sf} vs. n is plotted at $T \simeq 0.1$ to 0.2 eV and $P_N = 4 \times 10^{-9}$ Torr. For these parameters, the spin-flip rate is independent of average density.

Based on the data of Figures 5.7 and 5.8, it appears likely that ion spin depolarization occurs as a result of both ion-ion collisions, which depend strongly on ion temperature, and ion-neutral collisions, which have a weaker temperature dependence. At low neutral pressures, the ion-ion collisions dominate, and the spin-

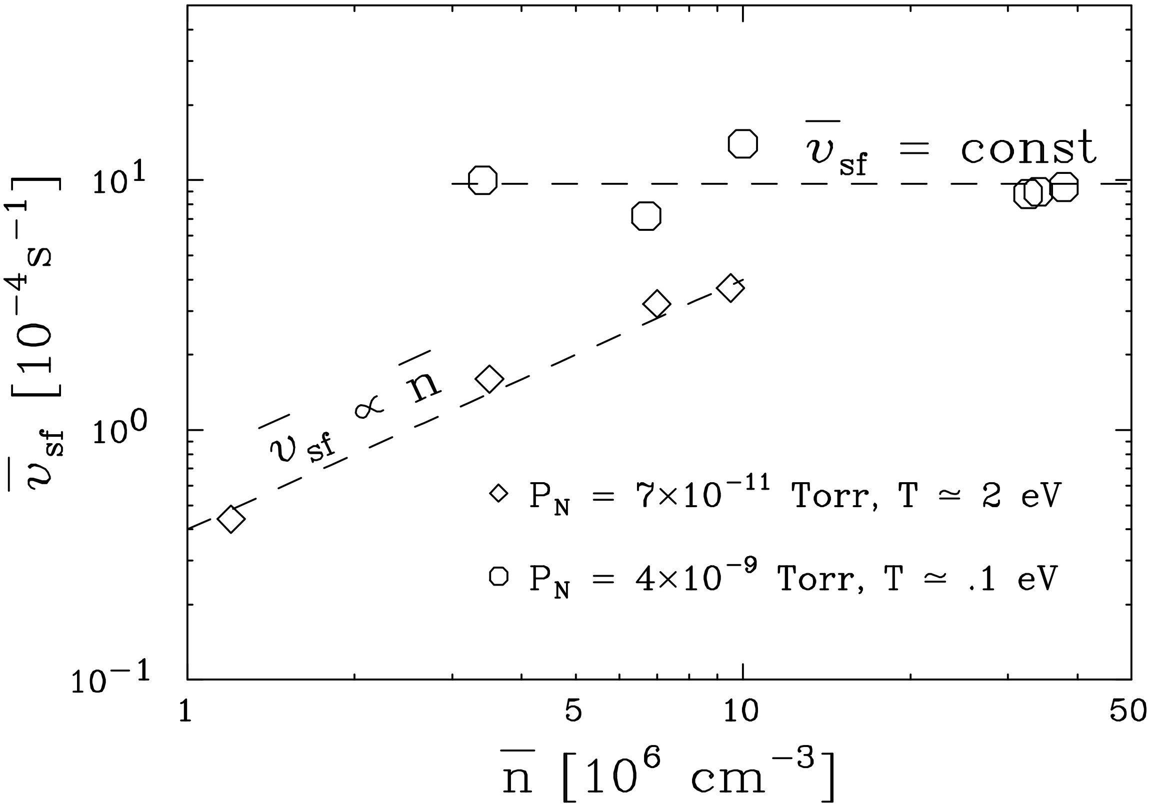

Figure 5.8: Spontaneous spin-flip rate measured as a function of density showing linear dependence at low neutral pressure and no clear dependence at high neutral pressure.

flip rate is linear in ion density; whereas at higher neutral pressures, the ion-neutral collisions dominate and the spin-flip rate does not depend on the plasma density. In either parameter regime, the maximum spontaneous spin flip rate observed is approximately $\nu_{sf} \simeq 10^{-2}\ \mathrm{s}^{-1}$, corresponding to a time scale of about 100 seconds for the depolarization of the spin-polarized plasma.

The spontaneous spin-flip is incorporated as a small correction to the test particle transport measurements. Prior to every test particle transport experiment, the average spontaneous spin-flip rate ν_{sf} is measured. The local spontaneous spin-flip rate $\nu_{sf}(r)$ used in Equation 5.3 is then estimated using $\nu_{sf}(r) \simeq n(r)\nu_{sf}/n$. This is not always a valid approximation, i.e. at high neutral pressures, we do not expect

$\nu_{sf} \propto n$. However, the test particle transport data used here is typically taken from the bulk of the plasma, where $n(r) \simeq n$ within a factor of 2, so this approximation is not expected to introduce errors greater than a factor of 2 into the estimated value of the local spin-flip rate $\nu_{sf}(r)$. With the inclusion of the spin-flip term in Equation 5.3, the total number of tagged particles is typically conserved within 10% in the test particle transport measurements. In any case, the spontaneous spin flip term constitutes a small correction to the measured $n_t(r, t)$. For the plasma shown in Figure 5.1, for example, the average spontaneous spin-flip rate was measured to be $\nu_{sf} = 5 \times 10^{-3}\mathrm{s}^{-1}$, which is clearly a small correction to the observed time evolution, which occurs on a time scale of about 10 seconds.

Appendix A

Corrections to LIF Diagnostic for Very Cold Plasmas

For most of the experiments described here, the three-Maxwellian fit given by Equation 2.2 is sufficiently accurate for the purposes of determining the plasma magnesium density n_{Mg}, temperature T, and rotation velocity v_{tot} from the scattered photon count rate as a function of laser detuning $\nu_{photon}(\delta\nu)$. For very cold plasmas ($T \lesssim 10^{-3}$ eV), we find that corrections due to the finite linewidth of the transition begin to become important, so the measured ν_{photon} needs to be fit to a Voigt, rather than Maxwellian, function. Also, centrifugal separation of the plasma species can become significant, so the assumption of Equation 2.2 that the magnesium isotopes are distributed according to their natural abundances is not always valid. Additionally, if the perpendicular LIF diagnostic is used, the plasma rotation can cause an apparent broadening of the observed transition due to the finite probe beam diameter. Here, a more detailed form of Equation 2.2 is derived which accounts for these corrections.

Figure A.1 provides a schematic of the basic detection scheme viewed axially along the $-\hat{z}$-direction. A perpendicular probe beam at position x is shown. The diagnosed volume has a height $H \simeq 4$ mm determined by the detection optics geometry. The plasma is rotating at an angular frequency $\omega_{tot} = 2\pi f_{tot}$.

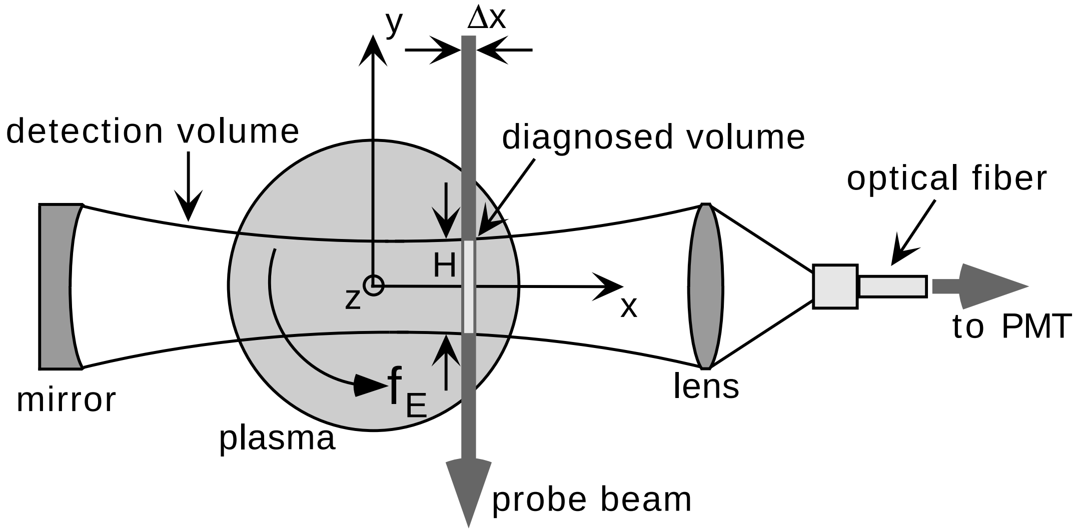

Figure A.1: Geometry of LIF diagnostic showing perpendicular probe beam. Components are not shown to scale; for example, the lens and mirror are much larger and farther from the plasma than indicated in the figure.

We assume the detection efficiency of photons scattered in the detection volume to be independent of position. At the powers used here, saturation of the transition and the resulting "power broadening" of the transition can be ignored. The measured photon count rate is then:

$$\nu_{photon}(\delta\nu) = \frac{\epsilon H}{h\nu_0} \int dx' d^3\mathbf{v}\, I(x') \sigma(\mathbf{v}, \delta\nu) f(\mathbf{v}) \ , \tag{A.1}$$

where ϵ is the collection efficiency of UV photons scattered in the diagnosed volume, σ is the scattering cross-section, $h\nu_0$ is the photon energy, and $f(\mathbf{v})$ is the lab-frame distribution function of ion velocities $\mathbf{v}$:

$$f(\mathbf{v}) = \frac{n}{(2\pi)^{3/2} v^3} \exp\left\{ -\frac{1}{2v^2} \left[(v_x + y\omega_{tot})^2 + (v_y - x\omega_{tot})^2 + v_z^2 \right] \right\} \ . \tag{A.2}$$

Neglecting ion recoil and relativistic corrections, the scattering cross-section is [64]:

$$\sigma(\mathbf{v}, \delta\nu) = \frac{\sigma_0 \left(\Delta\nu_0/2\right)^2}{(\delta\nu - \mathbf{k}\cdot\mathbf{v})^2 + (\Delta\nu_0/2)^2} \ , \tag{A.3}$$

where σ_0 is the total scattering cross-section, $\Delta\nu_0 \simeq 43$ MHz is the linewidth of the transition, $\delta\nu \equiv \nu - \nu_0$ is the laser detuning off-resonance, and $\mathbf{k}\cdot\mathbf{v} = \nu(v_y/c)$ is Doppler shift of the ion in the laser ($\hat{y}$) direction. In the work discussed here, where the laser light is polarized perpendicular to the magnetic field, we expect $\sigma_0 = 3\lambda_0^2/2\pi \simeq 1.8 \times 10^6 \text{Å}^2$ [34].

Direct measurements have found the probe beam intensity distribution to be well-described by a Gaussian about the beam position x:

$$I(x') = \frac{I_0}{\sqrt{\pi}\Delta x} e^{-[(x-x')/\Delta x]^2} , \tag{A.4}$$

with $\Delta x \simeq 0.5$ mm.

Equation A.1 then becomes:

$$\nu_{photon} = \frac{\sqrt{\pi}}{2} \frac{\epsilon H}{h\nu_0} n\, I_0\, \sigma_0 \frac{\Delta\nu_0}{\Delta\nu'}\, \mathrm{K}\left(\frac{\delta\nu - \nu_{rot}}{\Delta\nu'}, \frac{\Delta\nu_0}{2\Delta\nu'}\right) , \tag{A.5}$$

where $\nu_{rot} \equiv \nu_0\,(x\omega_{tot}/c)$ and $\Delta\nu' \equiv \sqrt{2}\nu_0(v'/c)$ with $v'^2 \equiv v_{24}^2 + \frac{1}{2}\omega_{tot}^2\Delta x^2$ and $v_{24} = \sqrt{T/m_{24}}$. K is the Voigt function, which is the convolution of a Gaussian and a Lorentzian: $\mathrm{K}(x,y) \equiv \frac{y}{\pi}\int_{-\infty}^{+\infty} \frac{e^{-t^2}}{y^2+(x-t)^2} dt$. Since the convolution of a Voigt function of linewidth y with a Lorentzian of linewidth y' is a Voigt function of linewidth $y + y'$, we can include the effect of the laser linewidth (about 1 MHz) by using $\Delta\nu_0 \rightarrow 43\,\text{MHz} + 1\,\text{MHz} = 44\,\text{MHz}$.

Equation A.5 can be modified to include all three magnesium isotopes:

$$\nu_{photon} = A \sum_s \frac{n_s}{\Delta\nu'_s} \mathrm{K}\left(\frac{\delta\nu - \nu_{rot} - \delta\nu_s}{\Delta\nu'_s}, \frac{\Delta\nu_0}{2\Delta\nu'_s}\right) , \tag{A.6}$$

where $\Delta\nu'_s$ is the same as $\Delta\nu'$ but using the mass m_s with s = 24, 25, or 26. n_s is the density of species s and $A \equiv \frac{\sqrt{\pi}}{2}\frac{\epsilon H}{h\nu_0} I_0\, \sigma_0\, \Delta\nu_0$. Our best theoretical estimate for ϵ, based on the light collection geometry and the efficiencies of the optical components, is $\epsilon \simeq 3 \times 10^{-5}$. In practice, we use the calibrated value $\epsilon = 6 \times 10^{-5}$, which is obtained by comparing LIF measurements with charge collection measurements and

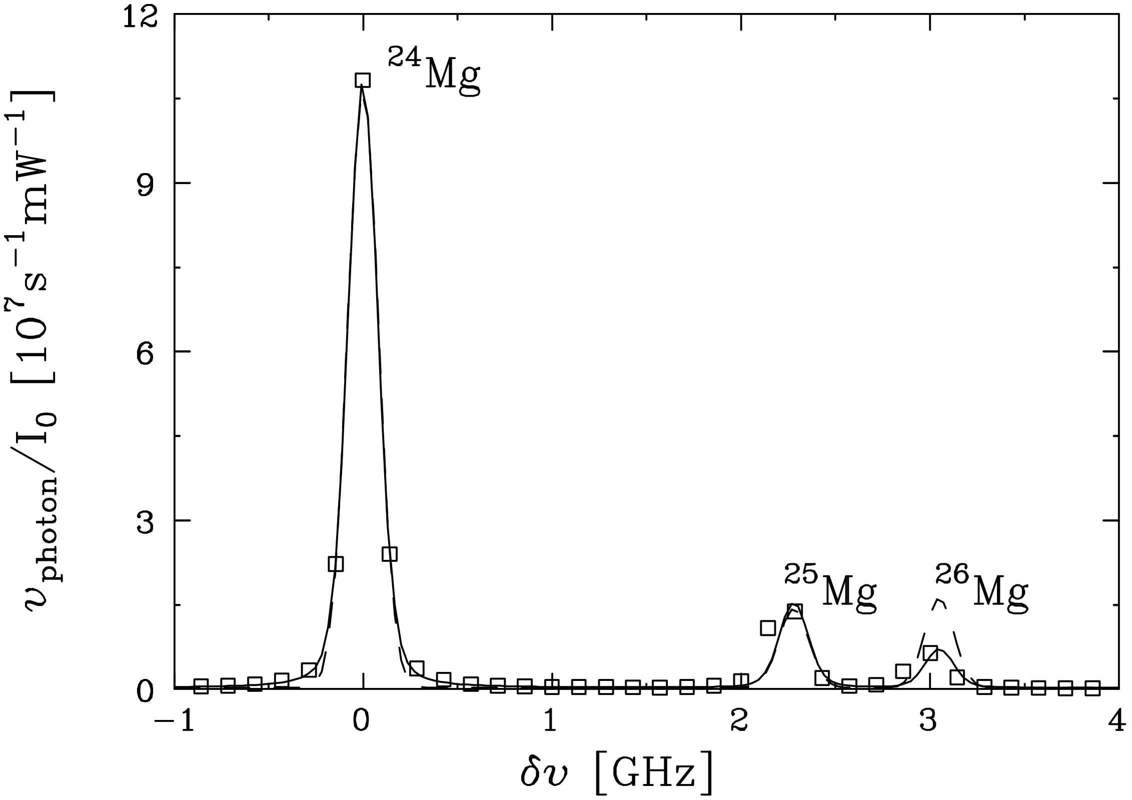

Figure A.2: Measured scattered photons for a laser-cooled plasma, showing three-Voigt fit with variable isotope abundances (solid line) and three-Maxwellian fit with natural isotope abundances (dashed line).

image charge measurements; this value of ϵ gives a peak LIF signal from Equation A.6 of $An/\Delta\nu \simeq (2.1 \times 10^5\,\text{photons/s})\,(n/10^7\,\text{cm}^{-3})(I_0/1\,\text{mW})(T/1\,\text{eV})^{-1/2}$.

Figure A.2 shows a LIF frequency scan for a laser-cooled plasma taken at radial position $r \simeq 0.2$ cm. Here, a weak ($I_0 \simeq 60\,\mu$W) probe beam is scanned through a cyclic transition of the three ^{24}Mg^{+} isotoptes; the scan goes from frequency detuning $\delta\nu = -10$ GHz to $\delta\nu = +10$ GHz in a time of about 6 seconds. We plot the measured scattered photon count rate ν_{photon} as a function of laser detuning $\delta\nu$. The photon count rate is normalized by the measured laser power I_0 during the frequency scan to account for small fluctuations in the probe beam power. The dashed line is a fit to the data of the form given by Equation 2.2; i.e. a three-Maxwellian fit assuming natural abundances of the magnesium isotopes. This fit gives a total magnesium density $n_{Mg} = 7.35 \times 10^7\,\mathrm{cm}^{-3}$ and temperature $T = 1.29 \times 10^{-4}$ eV. The solid line is a fit to the data of the form given by Equation A.6; i.e. a three-Voigt fit with variable abundances of the magnesium isotopes. This fit gives a total magnesium density $n_{Mg} = 7.52 \times 10^7\,\mathrm{cm}^{-3}$ and temperature $T = 0.93 \times 10^{-4}$ eV. It can be seen that the three-Voigt fit better describes the data; the height of the ^{26}Mg peak and the shape of the base of the ^{24}Mg peak, for example, are better fit by the three-Voigt fit. Here, the three-Maxwellian fit overestimates the temperature by about 40% and underestimates the density by about 3%. In general, we find that the three-Maxwellian fit slightly overestimates the temperature (up to a factor of 2) in very cold ($T \simeq 10^{-4}$ eV) magnesium plasmas. Unless the plasma is strongly centrifugally separated (very cold, high density plasmas), reasonable agreement is found between the densities obtained from the two fits.

Appendix B

Plasma Modes in a Long Cylindrical Plasma

The electrostatic modes in cylindrical nonneutral plasmas can be obtained from the collisionless drift-kinetic equation. This derivation assumes a guiding-center $\mathbf{E} \times \mathbf{B}$ drift motion in the azimuthal ($\hat{\theta}$) direction, but keeps the normal kinematics in the axial ($\hat{z}$) direction. The ion distribution function $f(\mathbf{r}, z, v_\perp, v_z, t)$ evolves as

$$\frac{\partial f}{\partial t} + \mathbf{v}_\perp \cdot \nabla_\perp f + v_z \frac{\partial f}{\partial z} - \frac{e}{m} \frac{\partial \Phi}{\partial z} \frac{\partial f}{\partial v_z} = 0 \tag{B.1}$$

where $\mathbf{v}_\perp = -\frac{c \nabla \Phi \times \hat{z}}{B}$ and $\mathbf{B} = +B\hat{z}$ for electrons and $\mathbf{B} = -B\hat{z}$ for ions. Equation B.1 can be linearized around the unperturbed distribution function f_u, assuming that $f = f_u + \delta f$ and $\Phi = \Phi_u + \delta\Phi$, where δf and $\delta\Phi$ are small perturbations oscillating like $e^{i(k_z z + m_\theta \theta - \omega t)}$. This gives:

$$\left(k_z v_z + m_\theta \omega_E - \omega\right) \delta f = \left(\frac{m_\theta c}{rB} \frac{\partial f_u}{\partial r} + \frac{k_z e}{m} \frac{\partial f_u}{\partial v_z}\right) \delta\Phi \tag{B.2}$$

where $\omega_E(r) = \frac{c}{rB} \frac{\partial \Phi_u}{\partial r}$ is the local unperturbed $\mathbf{E} \times \mathbf{B}$ rotation frequency. Using $\delta n = \int \delta f dv_z$, Poisson's Equation $\left(\frac{1}{r} \frac{\partial}{\partial r} r \frac{\partial}{\partial r} - \frac{m_\theta^2}{r^2} - k_z^2\right) \delta\Phi = -4\pi e \delta n$, and assuming that f_u is Maxwellian with no radial dependence in T gives:

$$\left\{ \frac{1}{r} \frac{\partial}{\partial r} r \frac{\partial}{\partial r} - \frac{m_\theta^2}{r^2} + \frac{4\pi m_\theta e c}{rB} \frac{\partial n_u}{\partial r} \frac{\left[W\left(\frac{\omega - m_\theta \omega_E}{k_z \bar{v}}\right) - 1\right]}{\omega - m_\theta \omega_E} \right.$$

$$\left. - \frac{\omega_p^2}{v^2} W\left(\frac{\omega - m_\theta \omega_E}{k_z v}\right) \right\} \delta\Phi = 0 \tag{B.3}$$

where $W(z) \equiv \frac{1}{\sqrt{2\pi}} \int_{-\infty}^{\infty} \frac{x e^{-x^2/2}}{x-z} dx$ is the Ichimaru W-function. This differential equation in $\delta\Phi$ can be solved numerically given an unperturbed density profile $n(r)$, a wave number k_z, and an azimuthal mode number m_θ [57]. Smooth, physical solutions only exist for discrete values of ω, corresponding to the mode frequencies for different radial mode numbers m_r. We use $k_z = m_z \pi / L_p$ for the wave number, where L_p is the length of the plasma. This is believed to be a reasonable estimate since, for the plasmas used here, $R_w / L_p < 1$ and numerical simulations of these modes in finite-length geometries find $k_z \simeq (m_z \pi / L) \left[1 - \mathcal{O}(R_w / L_p)\right]$ [35].

In Chapter 3, the numerical solution of Equation B.3 was used to estimate the mode frequencies. Often, however, it is also useful to have a simple analytical approximation for the mode frequencies. If we assume a top-hat density profile:

$$n(r) = \begin{cases} const. & , \; r \leq R_p \\ 0 & , \; r > R_p \end{cases} , \tag{B.4}$$

take the limits $T \rightarrow 0$ and $R_p k_z \rightarrow 0$, and assume that $\omega - m_\theta \omega_E \rightarrow 0$ in this limit, then Equation B.3 gives the dispersion relation:

$$\omega - m_\theta \omega_E \simeq C \omega_p R_p k_z \left[1 + \frac{3}{2} (v / v_\phi)^2\right] \tag{B.5}$$

$$\text{where } \; C \equiv \begin{cases} \sqrt{\frac{1}{2} \ln\left(R_w / R_p\right)} & , \; m_\theta = 0 \\ \pm 1 / j_{m_\theta m_r} & , \; m_\theta > 0 \end{cases}$$

with damping

$$\gamma \simeq -\sqrt{\pi / 8} \left(\omega - m_\theta \omega_E\right) \left(v_\phi / v\right)^3 e^{-\frac{1}{2}\left(v_\phi / \bar{v}\right)^2} , \tag{B.6}$$

where γ is the small imaginary component of ω. Here, $j_{m_\theta m_r}$ is the m_rth zero of the m_θth Bessel function and $v_\phi = \left(\omega - m_\theta \omega_E\right) / k_z$ is the axial mode phase velocity in the rotating frame. In these equations, m_θ is assumed to be positive; however, the short-hand notation $-m_\theta$ is used to denote the backwards rotating branch of the m_θ mode, which corresponds to the $-$ sign on the coefficient C.

It is of interest to note in Equation B.5 that $\omega - m_\theta \omega_E \propto \omega_p R_p k_z \propto N_L^{1/2} L_p^{-1}$, where N_L is the line-charge density. Thus, the mode frequencies in this limit are independent of plasma radius R_p (aside from the logarithmic correction in the $m_\theta=0$ case). More detailed analytical calculations of these modes have been made for finite-length geometries [51].

Appendix C

Cooling of an Ion Plasma due to Collisions with Neutrals

The potential describing the interaction between a charged particle and a neutral atom can be approximated:

$$V(\mathbf{r}) = V_{HS}(\mathbf{r}) - \frac{(1/2)\alpha e^2}{r^4} \, , \tag{C.1}$$

where V_{HS} is the short-range, repulsive "hard-sphere" potential, and $-\frac{1}{2}\alpha e^2/r^4$ is the long-range attractive potential resulting from the induced dipole moment of the neutral atom, where $\alpha \simeq 0.7\,\text{Å}^3$ is the mean polarizability of H_2 [13].

We expect V_{HS} to have a range corresponding to the molecular dimensions. The radius of an H_2 molecule is approximately 1.4 Å [7], while the radius of a Mg^+ molecule is about 1.0 Å [48], so the range of V_{HS} is expected to be approximately $r_{HS} \simeq 2.4\,\text{Å}$.

The range of the dipole interaction is approximately $r_\alpha \equiv (\alpha e^2/\mu w^2)^{1/4}$, where $\mu \equiv m m_N/(m + m_N)$ is the reduced mass and $w = |\mathbf{w}|$ is the magnitude of the relative velocity of the particles. For thermal particles with $m = 24$, $m_N = 2$, and $T_N = .026$ eV, we find $r_\alpha \simeq 2.6\,\text{Å}\,[(T/1\,\text{eV}) + .29]^{-1/4}$, so $r_\alpha > r_{HS}$ if $T < 1.1$ eV. That is, for higher temperatures ($T \gtrsim 1$ eV), we expect the hard-sphere potential to dominate, giving a constant scattering cross-section $\sigma_{HS} = \pi r_{HS}^2 \simeq 18\,\text{Å}^2$; while for lower temperatures ($T \lesssim 1$ eV), we expect the dipole potential to dominate.

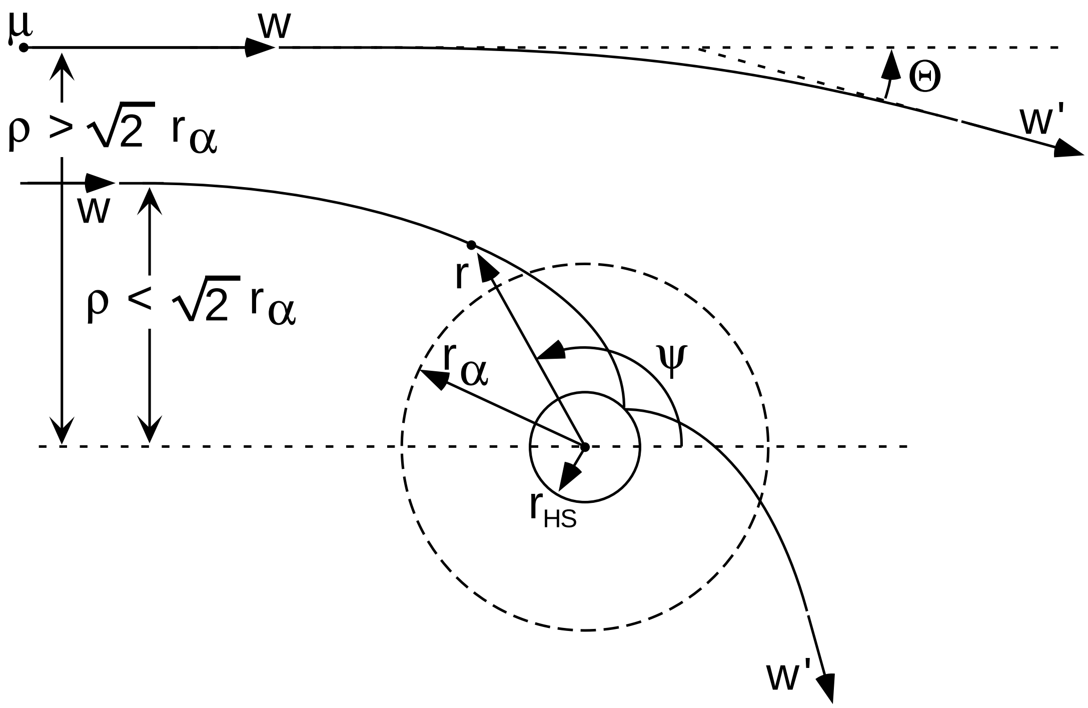

Figure C.1: Qualitative illustration of scattering off attractive dipole potential.

The ion data presented in this thesis covers a temperature range $5 \times 10^{-4} < T < 5$ eV, so the dipole interaction is expected to be dominant.

A qualitative picture of the scattering as seen in the center-of-mass frame is shown in Figure C.1. For $r > r_{HS}$, the potential is dominated by the dipole interaction, so the equation of motion of the particles is approximately:

$$d\psi = \frac{\rho}{r^2} \frac{dr}{\sqrt{1 - (\rho/r)^2 + (r_\alpha/r)^4}} , \tag{C.2}$$

where **r** is the relative position vector and ρ is the impact parameter.

For impact parameters $\rho < \sqrt{2}\, r_\alpha$, the relative radius r passes within the angular momentum barrier $r = r_\alpha$ and spirals into the force center, where the particle is eventually scattered by the hard-sphere potential. The resulting scattering angle Θ depends on the precise form of the close-range interaction between the H_2 molecule and the Mg^+ ion. Presumably, however, these collisions result in strong scattering, so a simple estimate for the total collision cross-section is given by the Langevin cross-section, $\sigma_{Lang} = \pi(\sqrt{2}\, r_\alpha)^2 = 2\pi(e/w)\sqrt{\alpha/\mu}$ [37], which gives an estimated ion-neutral collision frequency

$$\begin{aligned} \nu_{\rm iN} &\simeq 2\pi n_N e\sqrt{\alpha/\mu} \\ &\approx (2.5 \times 10^{-2}{\rm s}^{-1})\left(\frac{P_N}{10^{-9}{\rm Torr}}\right) , \end{aligned} \tag{C.3}$$

with a corresponding estimated heating rate

$$\frac{\partial T}{\partial t} \simeq -\nu_{\rm iN}\,(T - T_N) = -2\pi n_N e\sqrt{\alpha/\mu}\,(T - T_N)\ . \tag{C.4}$$

For impact parameters $\rho > \sqrt{2}\, r_\alpha$, r never reaches $r = r_\alpha$. The Langevin cross-section ignores these collisions, so the actual cross-section should be somewhat larger, i.e. $\sigma \simeq \pi\rho_{eff}^2$, with $\rho_{eff} > \sqrt{2}\, r_\alpha$. The energy transfered in a collision with scattering angle Θ goes like $1 - \cos\Theta$, so ρ_{eff} can be approximated as:

$$\rho_{eff}^2 \simeq 2\int_0^\infty (1 - \cos\Theta)\,\rho d\rho\ . \tag{C.5}$$

To evaluate Equation C.5, we assume that collisions with $\rho < \sqrt{2}\, r_\alpha$ are strongly scattered, so $\Theta(\rho < \sqrt{2}\, r_\alpha) \simeq \pi/2$. For $\rho > \sqrt{2}\, r_\alpha$, the final scattering angle is given by:

$$\Theta(\rho > \sqrt{2}\, r_\alpha) = 2\int_{r_{min}}^\infty \frac{\rho dr}{r^2\sqrt{1 - (\rho/r)^2 + (r_\alpha/r)^4}} - \pi\ , \tag{C.6}$$

where $r_{min}^2 \equiv \rho^2\left(1 + \sqrt{1 - (\sqrt{2}\, r_\alpha/\rho)^4}\right)/2$. Equation C.5 can then be evaluated numerically, giving $\rho_{eff}^2 \simeq 1.2\,(\sqrt{2}\, r_\alpha)^2$ with a corresponding approximate differential scattering cross-section $\sigma(\Theta) \simeq \rho_{eff}^2/4$.

Given a differential scattering cross-section $\sigma(\Theta)$ for ion-neutral collisions, the evolution of ions at temperature T in a bath of neutrals at fixed temperature T_N can be estimated with the Boltzman collision integral:

$$\frac{\partial T}{\partial t} = -\frac{m}{3n}\int d^3\mathbf{u}\, d^3\mathbf{v}\, |\mathbf{u} - \mathbf{v}|\, v^2 \int d\Omega\, \sigma(\Theta)\, [f(\mathbf{v})g(\mathbf{u}) - f(\mathbf{v}')g(\mathbf{u}')]\ , \tag{C.7}$$

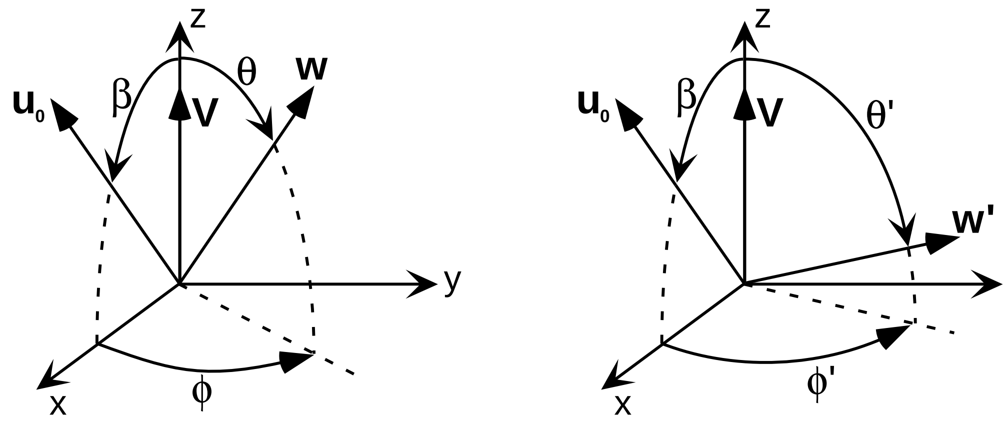

before collision

after collision

Figure C.2: Geometry of scattering in center-of-mass frame.

where $\mathbf{u}$ and $\mathbf{v}$ are the neutral and ion velocities prior to a collision, $\mathbf{u}'$ and $\mathbf{v}'$ are the corresponding velocities after the collision, and $\int d\Omega$ is the integral over scattering angles. The ions and neutrals are presumed to remain close to thermal equilibrium during the heating process, so the neutral and ion distribution functions in the rotating frame are: $g(\mathbf{u}) = \frac{n_N}{(2\pi)^{3/2}\bar{u}^3} e^{-\frac{1}{2}[(\mathbf{u}-\mathbf{u}_0)/\bar{u}]^2}$ and $f(\mathbf{v}) = \frac{n}{(2\pi)^{3/2}\bar{v}^3} e^{-\frac{1}{2}(\mathbf{v}/\bar{v})^2}$. Here, $\mathbf{u}_0$ is the average velocity of the neutral molecules in the rotating frame of the plasma, and the thermal velocities are $u = \sqrt{T_N/m_N}$ and $v = \sqrt{T/m}$.

Plugging $g(\mathbf{u})$, $f(\mathbf{v})$, and $\sigma(\Theta)$ into Equation C.7 and going to the center-of-mass coordinate system $\mathbf{w} \equiv \mathbf{u} - \mathbf{v}$ and $\mathbf{V} \equiv m_N \mathbf{u} + m\mathbf{v}$, where $m_N \equiv \frac{m_N}{m+m_N}$ and $m \equiv \frac{m}{m+m_N}$ gives:

$$
\begin{aligned}
\frac{\partial T}{\partial t} &= -\frac{1}{5}\frac{m}{(2\pi)^3}\frac{n_N}{u^3 v^3} e\sqrt{\alpha/\mu} \qquad \text{(C.8)} \\
&\times \int d^3\mathbf{w}\, d^3\mathbf{V}\, v^2 \int d\Omega \, \left\{ e^{-\frac{1}{2}(v/\bar{v})^2} e^{-\frac{1}{2}[(\mathbf{u}-\mathbf{u}_0)/\bar{u}]^2} - e^{-\frac{1}{2}(v'/\bar{v})^2} e^{-\frac{1}{2}[(\mathbf{u}'-\mathbf{u}_0)/\bar{u}]^2} \right\} .
\end{aligned}
$$

The integrals in Equation C.8 can be evaluated using the coordinate system shown in Figure C.2. After the collision, the relative velocity vector $\mathbf{w}$ changes orientation, but not magnitude, so $w' = w$, but $\mathbf{w}' \neq \mathbf{w}$. The center-of-mass vector

$\mathbf{V}$ is unchanged, so $\mathbf{V}' = \mathbf{V}$. The scattering angle Θ of Figure C.1 is related to these quantities through $\mathbf{w} \cdot \mathbf{w}' = ww' \cos\Theta$. From Figure C.2, one finds the relations

$$u^2 = V^2 + 2mwV\cos\theta + m^2w^2 \ , \tag{C.9}$$

$$v^2 = V^2 - 2m_N wV\cos\theta + m_N^2 w^2 \ , \tag{C.10}$$

and

$$\begin{aligned} (\mathbf{u} - \mathbf{u}_0)^2 &= V^2 + m^2w^2 + u_0^2 + 2mwV\cos\theta \\ &- 2mwu_0(\sin\beta\cos\phi\sin\theta + \cos\beta\cos\theta) - 2u_0V\cos\beta \end{aligned} \tag{C.11}$$

with $d\Omega = \sin\theta' d\theta' d\phi'$. Equation C.8 can then be evaluated to give:

$$\frac{\partial T}{\partial t} \simeq -5\pi n_N e\sqrt{\alpha/\mu}\frac{mm_N}{(m+m_N)^2}(T - T_{N,eff}) \ , \tag{C.12}$$

where

$$\begin{aligned} T_{N,eff} &\equiv T_N + \frac{1}{3}m_N u_0^2 = T_N + \frac{1}{3}m_N r^2 \omega_{tot}^2 \\ &\approx 0.026\,\mathrm{eV}\left[1 + 1.1\times10^{-3}\left(\frac{r}{1\ \mathrm{cm}}\right)^2\left(\frac{f_{tot}}{1\ \mathrm{kHz}}\right)^2\right] \ . \end{aligned} \tag{C.13}$$

This is the same result as was obtained from the Langevin cross section (Equation C.4) with the addition of a mass-ratio factor $\frac{2mm_N}{(m+m_N)^2}$, a factor 1.2 from the estimated contribution of the $\rho > \sqrt{2}\,r_\alpha$ collisions, and using the effective neutral temperature in the rotating frame, $T_{N,eff}$, instead of T_N.

Appendix D

Estimating the Radial-Expansion Flux of Ion Plasmas

In order to estimate the Joule heating resulting from ion plasma expansion (for Section 4.3.3), it is necessary to have a model for the radial particle flux of ion plasmas. In a radial-expansion experiment, the radial particle flux Γ_m is obtained from the measured density $n(r,t)$ by conservation of particles:

$$\Gamma_m = -\frac{1}{r}\int_0^r \frac{\partial n(r')}{\partial t} r' dr' \; . \tag{D.1}$$

The expansion rate of the plasma can be obtained by integrating over the radial flux:

$$\tau_{\langle r^2 \rangle}^{-1} \equiv \frac{\partial}{\partial t}\langle r^2 \rangle / \langle r^2 \rangle = 2 \int \Gamma_m r^2 dr \Big/ \int n r^3 dr \; . \tag{D.2}$$

In Figure D.1, we plot the measured radial particle flux Γ_m for the experiment shown in Figure 3.14. In general, we observe a radial flux of the approximate shape $\Gamma_m \propto nr$; in Figure D.1, the dashed line corresponds to $\Gamma_m = 1.3 \times 10^4 \text{ cm}^{-2}\text{s}^{-1} \, (n/10^7 \text{ cm}^{-3})(r/1 \text{ cm})$, demonstrating that this functional form describes the radial shape of the data reasonably well.

As discussed in Section 3.4, we do not observe a clear density or temperature dependence in the measured free expansion rate $\tau_{\langle r^2 \rangle}^{-1}$ of ion plasmas. These measurements were taken at magnetic field $B = 4$ T and length $L_p \simeq 12$ cm and find an average expansion rate of $\tau_{\langle r^2 \rangle}^{-1} \simeq (1.7 \pm 1.3) \times 10^{-3} \text{ s}^{-1}$. For the same data,

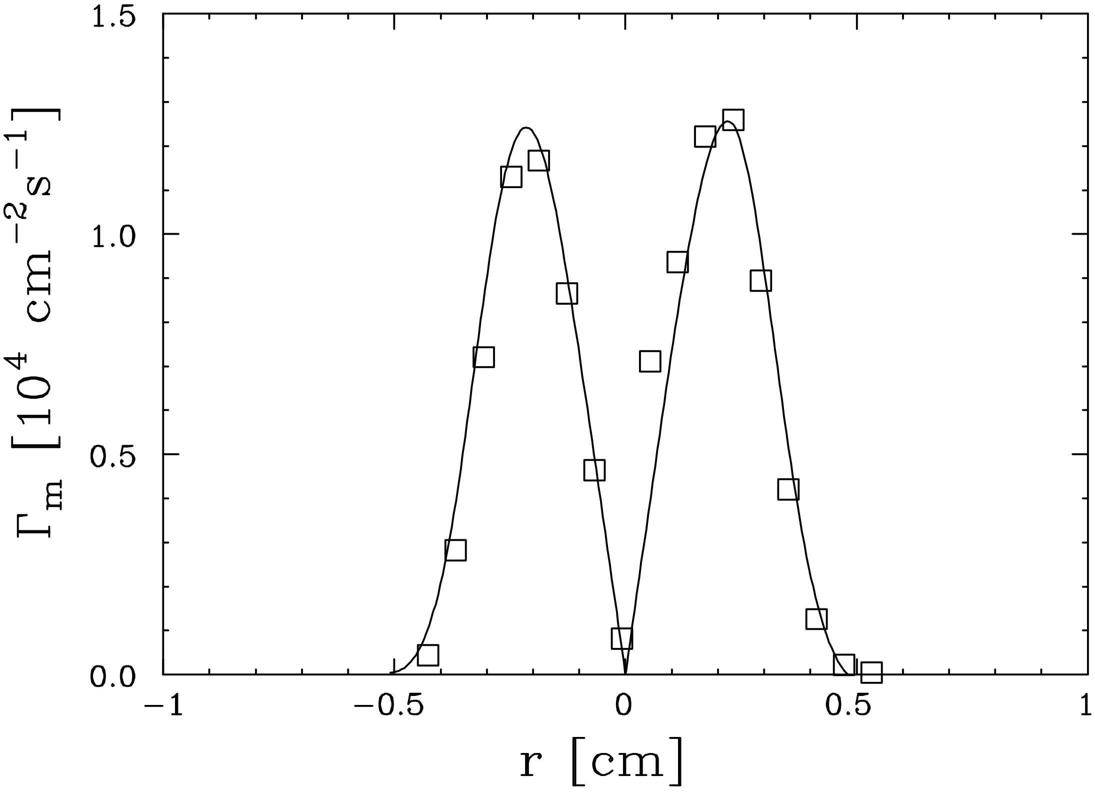

Figure D.1: Radial flux obtained from free-expansion experiment of Figure 3.14.

we find the relative scatter in the unnormalized expansion rate to be smaller, i.e. $\langle \dot{r^2} \rangle = (2.4 \pm 1.3) \times 10^{-4}\,\mathrm{cm}^2\mathrm{s}^{-1}$.

In the absense of a clear density or temperature scaling, we will assume $\langle \dot{r^2} \rangle \propto n^0 T^0$. However, we will assume the standard inherent asymmetry transport scaling with magnetic field and plasma length, $\langle \dot{r^2} \rangle \propto L_p^2 B^{-2}$. Although a rigorous study of the magnetic field and length dependence of expansion rate in ion plasmas has not been performed, this scaling appears to apply to our ion plasmas on a qualitative level, i.e. shorter ion plasmas in stronger magnetic fields are observed to expand radially much more slowly than longer ion plasmas in weaker magnetic fields.

Our estimate for the radial expansion rate of IV ion plasmas is then: $\langle \dot{r^2} \rangle \simeq (2.7 \times 10^{-3}\,\mathrm{s}^{-1})\,(B/1\,\mathrm{T})^{-2}(L_p/10\,\mathrm{cm})^2$. Assuming $\Gamma_m \propto nr$, Equation D.2 can be used to estimate an empirical form for the radial flux of radially-expanding ion plasmas in the IV apparatus:

$$\Gamma_m \approx \left(24\,\mathrm{cm}^{-2}\mathrm{s}^{-1}\right)\left(\frac{B}{1\,\mathrm{T}}\right)^{-2}\left(\frac{L_p}{10\,\mathrm{cm}}\right)^{2}\left(\frac{n}{10^7\,\mathrm{cm}^{-3}}\right)\left(\frac{r}{1\,\mathrm{cm}}\right)\left(\frac{R_p}{1\,\mathrm{cm}}\right)^{-2} . \qquad \text{(D.3)}$$

The B and L_p scalings of this model agree with those observed in other experiments, but the n and T scalings differ. That is, experiments in electron plasmas (Figure 3.18) generally find a free expansion rate $\tau_m^{-1} \propto R^{-2} \propto B^{-2}L_p^2n^2T^{-1}$, which gives a radial flux scaling $\Gamma_m \propto B^{-2}L_p^2n^3T^{-1}$, in contrast to the scaling of Equation D.3, $\Gamma_m \propto B^{-2}L_p^2nT^0$.

Appendix E

Symbols and Notations

This appendix compiles the symbols and notations commonly used in this work. Whenever necessary, a definition of a symbol or the equation number where it is first introduced is given. All equations are in the cgs convention. In general, a subscript "e" refers to a quantity applied to electrons; a subscript "24" applies to a quantities applied to $^{24}\mathrm{Mg}^{+}$; e.g. "m_e" is the electron mass, while "m_{24}" is the $^{24}\mathrm{Mg}^{+}$ mass. The subscript "N" refers to neutral gas, e.g. T_N is the neutral temperature, while the subscript "t" refers to spin-tagged test particles, e.g. n_t is the density of test particles.

********** Fundamental Quantities **********

e		Particle charge ($e < 0$ for electrons)
m		Particle mass
t		Time
(x, y, z)		Cartesian coordinates centered on the trap axis
(r, θ, z)		Cylindrical coordinates centered on the trap axis
$\mathbf{B}$	$B\hat{z}$	Magnetic field
Φ		Electrostatic potential
$\mathbf{E}$	$-\nabla\Phi$	Electric field
n		Density
c		Speed of light in vacuum
$\hbar$	$h/2\pi$	Planck's constant

********** Energies and Velocities **********

$T_\perp$		Temperature perpendicular to **B**
$T_\parallel$		Temperature parallel to **B**
T	$\frac{1}{3}T_\parallel + \frac{2}{3}T_\perp$	Average temperature
ΔT	$T_\parallel - T_\perp$	Temperature anisotropy
T_∞	$T(t \to \infty)$	Equilibrium temperature
δT	$T - T_\infty$	Perturbation about equilibrium temperature
v	$\sqrt{T/m}$	Thermal velocity
P	nT	Pressure
q	$\frac{3}{2}nT$	Energy density
$\dot{q}$	$\partial q/\partial t$	Rate of change of plasma energy density
$\dot{q}_{ext}$		Component of $\dot{q}$ from external perturbations
$\dot{q}_J$	Eqn. (5.9)	Component of $\dot{q}_{ext}$ resulting from plasma expansion (Joule heating)
$\dot{q}_N$	Eqn. (5.9)	Component of $\dot{q}_{ext}$ resulting from ion-neutral collisions
v_{dia}	Eqn. (2.3)	Diamagnetic rotation velocity of plasma
v_E	Eqn. (2.4)	**E** × **B** rotation velocity of plasma
v_{tot}	$v_{dia} + v_E$	Total rotation velocity
v_ϕ	$(\omega - m_\theta \omega_E)/k_z$	Azimuthal phase velocity of mode

********** Lengths **********

L_p	5 cm→50 cm	Length of Plasma
R_p	0.2 cm→1 cm	Radius of Plasma
R_w	2.86 cm	Radius of trap wall
L_r	5.84 cm	Length of trap rings
d_c	1 mm	Diameter of collimator plate hole
H	$\simeq$ 4 mm	Height of LIF-diagnosed volume
λ_D	$\sqrt{T/4\pi n e^2}$	Debye length
r_c	v/Ω_c	Cyclotron radius
λ_0	c/ν_0	Wavelength of atomic resonance
L_T	$\sim R_p$	Length of thermal gradient
b	e^2/T	Distance of closest approach
ρ		Impact parameter of a collision

********** Times and Frequencies **********

ω_p	$\sqrt{4\pi n e^2/m}$	Plasma frequency
Ω_c	eB/mc	Cyclotron frequency
f_E	$v_E/2\pi r$	$\mathbf{E} \times \mathbf{B}$ rotation frequency of plasma
f_b	$v/2L_p$	Thermal bounce frequency
ν_{ii}	Eqn. (4.5)	Ion-ion collision rate
ν_{ee}	Eqn. (4.5)	Electron-electron collision rate
ν_{iN}	Eqn. (C.3)	Ion-neutral collision rate
$\nu_{\perp 0}$	$\frac{3}{2}\nu_{ii}$, $3\nu_{\perp\parallel}$	Anisotropic temperature relaxation rate resulting from ion-ion collisions
ν_{eq}	$\nu_{\perp 0} + \nu_{iN}$	Total anisotropic temperature relaxation rate
f		Electrostatic mode frequency
f_s		Frequency of a signal applied to a ring or sector
f_w	f_s/m_θ	Rotation frequency of an applied signal with azimuthal dependence
f_1	$\simeq N_L ec/\pi B R_w^2$	$m_\theta = 1$ diocotron mode frequency
γ		Mode damping rate
ν		Frequency of laser light
ν_0		Resonance frequency of Mg^+ atomic transition
$\delta\nu$		Laser detuning off-resonance
ν_{photon}		Count rate of scattered photons
$\Delta\nu$	$\sqrt{2}\nu_0(v/c)$	Doppler broadening of atomic transition
$\Delta\nu_0$	$\simeq 43$ MHz	Linewidth of atomic transition
ν_{rot}	$\nu_0(v_{tot}/c)$	Doppler shift of atomic transition due to plasma rotation
τ_m		Time for radially-expanding plasma to decrease its central density by a factor of 2
τ_{bck}^{-1}	$-\dot{n}_0/n_0$	Central density expansion rate of radially-expanding plasma n_0
$\tau_{\langle r^2\rangle}^{-1}$	$\dot{\langle r^2\rangle}/\langle r^2\rangle$	mean-square radius expansion rate of plasma
ν_{sf}		Spontaneous spin-flip rate
ν_{sf}	$\nu_{sf}(n/n)$	Spontaneous spin-flip rate averaged over plasma
ν_{op}		Optical pumping rate from laser sidebands
τ_t^{-1}	$\nu_{op} + \nu_{sf}$	total rate of test-particle spin-flip
ν_{dump}	$\dot{V}_c/T$	Rate at which confinement potential is dropped
ν_{wig}		Plasma heating rate from applied "wiggle" perturbation

Note that $\omega = 2\pi f$ for all frequencies.

********** Integrals **********

P_θ	Eqn. (2.1)	Plasma angular momentum
N_L	$2\pi \int nrdr$	Line charge density of plasma
N_{tot}	$L_p N_L$	Total number of particles in plasma
$\dot{Q}$	$2\pi L_p \int \dot{q} rdr$	Total plasma heating rate
$\dot{Q}_J$	$2\pi L_p \int \dot{q}_J rdr$	Component of $\dot{Q}$ resulting from plasma expansion
$\dot{Q}_N$	$2\pi L_p \int \dot{q}_N rdr$	Component of $\dot{Q}$ resulting from ion-neutral collisions
n	$\int n^2 rdr / \int nrdr$	Average plasma density

********** Fluxes and Transport Coefficients **********

Γ_q	Eqn. (5.5)	Radial heat flux
χ	Eqn. (5.6)	Measured thermal diffusivity
χ_c	Eqn. (5.1)	Classical thermal diffusivity
χ_L	Eqn. (5.2)	Long-range thermal diffusivity
Γ_t	Eqn. (6.3)	Flux of test particles
D	Eqn. (6.4)	Measured test-particle diffusion coefficient
D_c	Eqn. (6.1)	Classical test-particle diffusion coefficient
D_L	Eqn. (6.2)	Long-range test-particle diffusion coefficient
D_N	Eqn. (6.5)	Test-particle diffusion coefficient for ion-neutral collisions
Γ_m	Eqn. (D.1)	Radial particle flux of radially-expanding plasma

********** Miscellaneous **********

n_0	$n(r=0)$	Central plasma density
n_7	$n/10^7\mathrm{cm}^{-3}$	Normalized plasma density
n_B	$B^2/8\pi mc^2$	Brillouin density
I_0		Intensity of laser beam
$\langle I_0\rangle$		Time-averaged intensity of laser beam
α	0.7 Å^3	Average polarizability of H_2 molecule
μ	$mm_N/(m+m_N)$	Reduced mass for ion-neutral collisions
β	$\frac{\partial}{\partial T}\dot{q}_{ext}(T_\infty)$	Temperature derivative of external heating term
m_j		Spin state of Mg^+ valence electron relative to **B**
$T_{N,eff}$	Eqn. (C.10)	Effective temperature of neutrals in rotating frame of plasma
n_{final}	$n_t(t\rightarrow\infty)$	Measured final test particle density
n_{back}		Background (noise) density measured by LIF diagnostic
k	$2\pi/\lambda$	Photon wavenumber
$\mathbf{p}$	$\hbar\mathbf{k}$	Photon momentum vector
σ		Scattering cross-section
(m_θ, m_r, m_z)		Azimuthal, radial, and axial mode numbers for plasma modes
R	f_b/f_E	Plasma rigidity
k_z	$\simeq m_z\pi/L_p$	Axial wave number of a plasma mode
A_s		Amplitude of a signal applied to a ring or sector
V_c	$\simeq \pm 200$ V	End-confinement potential
Q	$\omega/2\gamma$	Mode quality
Q_c		Charge collected on collimator plate
Q_F		Charge collected on Faraday cup
ϵ	$\sim 10^{-5}$	efficiency of LIF detection optics

References

[1] F. Anderegg, E. M. Hollmann, and C. F. Driscoll. Rotating field confinement of pure electron plasmas using Trivelpiece-Gould modes. *Phys. Rev. Lett.*, 81:4875, 1998.

[2] F. Anderegg, X. P. Huang, C. F. Driscoll, E. M. Hollmann, T. M. O'Neil, and D. H. E. Dubin. Test particle transport due to long range interactions. *Phys. Rev. Lett.*, 78:2128, 1997.

[3] F. Anderegg, X. P. Huang, E. M. Hollmann, C. F. Driscoll, T. M. O'Neil, and D. H. E. Dubin. Test particle transport from long range collisions. *Phys. Plasmas*, 4:1552, 1997.

[4] F. Anderegg, X. P. Huang, E. Sarid, and C. F. Driscoll. A new pure ion plasma device with laser induced fluorescence diagnostic. *Rev. Sci. Instrum.*, 68:2367, 1997.

[5] B. R. Beck. *Measurement of the Magnetic and Temperature Dependence of the Electron-Electron Anisotropic Temperature Relaxation Rate.* PhD thesis, University of California at San Diego, 1990.

[6] B. R. Beck, J. Fajans, and J. H. Malmberg. Measurement of collisional anisotropic temperature relaxation in a strongly magnetized pure electron plasma. *Phys. Rev. Lett.*, 68:317, 1992.

[7] P. K. Biswas. Excitation and ionization of the positronium atom in positronium-hydrogen molecule scattering. *Phys. Lett. A*, 223:173, 1996.

[8] L. Brillouin. A theorem of Larmor and its importance for electrons in magnetic fields. *Phys. Rev.*, 67:260, 1945.

[9] F. F. Chen. *Introduction to Plasma Physics and Controlled Fusion*, volume 1. Plenum Press, second edition, 1984.

[10] B. P. Cluggish, J. R. Danielson, and C. F. Driscoll. Resonant particle heating of an electron plasma by oscillating sheaths. *Phys. Rev. Lett.*, 81:353, 1998.

[11] B. P. Cluggish and C. F. Driscoll. Transport and damping from rotational pumping in magnetized electron plasmas. *Phys. Rev. Lett.*, 74:4213, 1995.

[12] S. M. Crooks. *Rotational Pumping Transport in Magnetized Non-Neutral Plasmas.* PhD thesis, University of California at San Diego, 1995.

[13] A. Dalgarno, M. R. C. McDowell, and A. Williams. The mobilities of ions in unlike gases. *Phil. Trans. Roy. Soc. A*, 250:411, 1958.

[14] R. C. Davidson. *Physics of Nonneutral Plasmas.* Addison-Wesley, 1990.

[15] C. F. Driscoll. Containment of single-species plasmas at low energies. In D. Kline, editor, *Low Energy Antimatter*, page 184. Singapore:World Scientific, 1986.

[16] C. F. Driscoll, K. S. Fine, and J. H. Malmberg. Reduction of radial losses in a pure electron plasma. *Phys. Fluids*, 29:2015, 1986.

[17] R. E. Drullinger, D. J. Wineland, and J. C. Bergquist. High-resolution optical spectra of laser cooled ions. *Appl. Phys.*, 22:365, 1980.

[18] D. H. E. Dubin. Private Communication.

[19] D. H. E. Dubin. Test particle diffusion and the failure of integration along unperturbed orbits. *Phys. Rev. Lett.*, 79:2678, 1997.

[20] D. H. E. Dubin and T. M. O'Neil. Cross-magnetic-field heat conduction in non-neutral plasmas. *Phys. Rev. Lett.*, 78:3868, 1997.

[21] D. H. E. Dubin and T. M. O'Neil. Two-dimensional bounce-averaged collisional particle transport in a single species non-neutral plasma. *Phys. Plasmas*, 5:1305, 1998.

[22] D. L. Eggelston, C. F. Driscoll, B. R. Beck, A. W. Hyatt, and J. H. Malmberg. Parallel energy analyzer for pure electron plasma devices. *Phys. Fluids B*, 4:3432, 1992.

[23] D. L. Eggelston, T. M. O'Neil, and J. H. Malmberg. Collective enhancement of radial transport. *Phys. Rev. Lett.*, 53:982, 1984.

[24] K. S. Fine. *Experiments with the l=1 Diocotron Mode.* PhD thesis, University of California at San Diego, 1988.

[25] M. E. Glinsky, T. M. O'Neil, M. N. Rosenbluth, K. Tsuruta, and S. Ichimaru. Collisional equipartition rate for a magnetized pure electron plasma. *Phys. Fluids B*, 4:1156, 1992.

[26] T. W. Haensch and A. L. Schawlow. Cooling of gases by laser radiation. *Opt. Commun.*, 13:68, 1975.

[27] D. J. Heinzen, J. J. Bollinger, F. L Moore, W. M Itano, and D. J. Wineland. Rotational equilibria and low-order modes of a non-neutral ion plasma. *Phys. Rev. Lett.*, 66:2080, 1991.

[28] X. P. Huang, F. Anderegg, E. M. Hollmann, C. F. Driscoll, and T. M. O'Neil. Steady-state confinement of nonneutral plasmas by rotating electric fields. *Phys. Rev. Lett.*, 78:875, 1997.

[29] X. P. Huang, J. J. Bollinger, T. B. Mitchell, and W. M. Itano. Phase-locked rotation of crystallized non-neutral plasmas by rotating electric fields. *Phys. Rev. Lett.*, 80:73, 1998.

[30] A. W. Hyatt. *Measurement of the Anisotropic Temperature Relaxation Rate in a Magnetized Pure Electron Plasma.* PhD thesis, University of California at San Diego, 1988.

[31] A. W. Hyatt, C. F. Driscoll, and J. H. Malmberg. Measurement of the anisotropic temperature relaxation rate in a pure electron plasma. *Phys. Rev. Lett.*, 59:2975, 1987.

[32] S. M. Ichimaru, H. Iyetomi, and S. Tanaka. Statistical physics of dense plasmas: Thermodynamics, transport coefficients, and dynamic correlations. *Phys. Rep.*, 149:93, 1987.

[33] S. M. Ichimaru and M. N. Rosenbluth. Relaxation processes in plasmas with magnetic field. Temperature relaxations. *Phys. Fluids*, 13:2778, 1970.

[34] W. M. Itano and D. J. Wineland. Laser cooling of ions stored in harmonic and Penning traps. *Phys. Rev. A*, 25:35, 1982.

[35] J. K. Jennings, R. L. Spencer, and K. C. Hansen. Numerical calculation of axisymmetric electrostatic modes for cold finite-length non-neutral plasmas. *Phys. Plasmas*, 2:2630, 1995.

[36] J. M. Kriesel. *Experiments on Viscosity and Asymmetry-Induced Transport in Magnetized, Pure Electron Plasmas.* PhD thesis, University of California at San Diego, 1999.

[37] P. Langevin. A fundamental formula of kinetic theory. *Ann. Chim. Phys.*, 8:245, 1905.

[38] E. M. Lifshitz and L. P. Pitaevskii. *Physical Kinetics.* Pergamon, 1981.

[39] C. L. Longmire and M. N. Rosenbluth. Diffusion of charged particles across a magnetic field. *Phys. Rev.*, 103:507, 1956.

[40] J. H. Malmberg and J. S. deGrassie. Properties of a nonneutral plasma. *Phys. Rev. Lett.*, 35:577, 1975.

[41] T. B. Mitchell. Private Communication.

[42] T. B. Mitchell. *Experiments on Electron Vortices in a Malmberg-Penning Trap.* PhD thesis, University of California at San Diego, 1993.

[43] T. B. Mitchell, J. J. Bollinger, X. P. Huang, and W. M. Itano. Doppler imaging of plasma modes in a Penning trap. *Optics Express*, 2:8, 1998.

[44] D. Montgomery, G. Joyce, and L. Turner. Magnetic field dependence of plasma relaxation times. *Phys. Fluids*, 17:2201, 1974.

[45] T. M. O'Neil. Centrifugal separation of a multispecies pure ion plasma. *Phys. Fluids*, 24:1447, 1981.

[46] T. M. O'Neil. A new theory of transport due to like particle collisions. *Phys. Rev. Lett.*, 55:943, 1985.

[47] T. M. O'Neil and C. F. Driscoll. Transport to thermal equilibrium of a pure electron plasma. *Phys. Fluids*, 22:266, 1979.

[48] W. B. Pearson. *Handbook of Lattice Spacings and Structures of Metals and Alloys*. Pergamon, 1958.

[49] F. M. Penning. Low-pressure glow discharge between coaxial cylinders in an axial magnetic field. *Physica*, 3:873, 1936.

[50] S. Pistinner, A. Levinson, and E. Eichler. Can electromagnetic instabilities driven by temperature gradients inhibit thermal conduction in cluster cooling flows? *Astrophys. J.*, 467:162, 1996.

[51] S. A. Prasad and T. M. O'Neil. Waves in a cold pure electron plasma of finite length. *Phys. Plasmas*, 26:665, 1983.

[52] M. N. Rosenbluth and A. N. Kaufmann. Plasma diffusion in a magnetic field. *Phys. Rev.*, 109:1, 1958.

[53] M. N. Rosenbluth and C. S. Liu. Cross-field energy transport by plasma waves. *Phys. Fluids*, 19:815, 1976.

[54] E. Sarid, F. Anderegg, and C. F. Driscoll. Cyclotron resonance phenomena in a non-neutral multispecies ion plasma. *Phys. Plasmas*, 2:2895, 1995.

[55] A. Simon. Diffusion of like particles across a magnetic field. *Phys. Rev.*, 100:1557, 1955.

[56] F. Skiff, T. N. Good, F. Anderegg, and P. J. Paris. Plasma diagnostics with spin-polarized ions. *Phys. Lett. A*, 137:57, 1989.

[57] R. L. Spencer. Private Communication.

[58] L. Spitzer. *Physics of Fully Ionized Gas*. Interscience, 1955.

[59] A. W. Trivelpiece and R. W. Gould. Space charge waves in cylindrical plasma columns. *J. Appl. Phys.*, 30:1784, 1959.

[60] M. Tuszewski. Particle and heat transport in a low-frequency inductively coupled plasma. *Phys. Plasmas*, 5:1198, 1998.

[61] F. Wagner and U. Stroth. Transport in toroidal devices - the experimentalist's view. *Plasma Phys. and Contr. Fusion*, 35:1321, 1993.

[62] C. S. Weimer, J. J. Bollinger, F. L. Moore, and D. J. Wineland. Electrostatic modes as a diagnostic in Penning-trap experiments. *Phys. Rev. A*, 49:3842, 1994.

[63] D. J. Wineland and H. Dehmelt. Proposed 10^{14} $\delta\nu < \nu$ laser fluorescence spectroscopy on Tl^+ mono-ion oscillator III. *Bull. Am. Phys. Soc.*, 20:637, 1975.

[64] D. J. Wineland and W. M. Itano. Laser cooling of atoms. *Phys. Rev. A*, 20:1521, 1979.

[65] D. J. Wineland and W. M. Itano. Laser cooling. *Phys. Today*, page 2, June, 1987.